

Luminescent, porous, metal-organic crystals: Design, synthesis, and applications

Présentée le 17 décembre 2020

à la Faculté des sciences de base
Laboratoire de simulation moléculaire
Programme doctoral en chimie et génie chimique

pour l'obtention du grade de Docteur ès Sciences

par

Fatmah EBRAHIM

Acceptée sur proposition du jury

Prof. A. Züttel, président du jury
Prof. B. Smit, C. P. Ireland, directeurs de thèse
Prof. R. H. Friend, rapporteur
Prof. G. Grancini, rapporteuse
Prof. P. J. Dyson, rapporteur

To my quirky, loving, wonderful family...



Acknowledgements

The three years that I have spent towards this PhD felt as fleeting as they have been enriching. For the many experiences that I have had, and things that I have learned, I have many people to thank.

First, I am extremely grateful to my advisor, Prof. Berend Smit, for giving me the opportunity to work in his lab and for introducing me to the fascinating world of MOFs. It is not so common to find an advisor who is always willing to take out time to share their wisdoms and teach their students how to focus on the big picture, think strategically, and uncover hidden possibilities in their work. For this I consider myself very fortunate indeed. A very special thanks goes to Prof. Kyriakos Stylianou, for without his advice and endless support during the first two years of my doctorate, I could not have acquired the scientific maturity needed to progress in experimental chemistry. I would like to thank Dr. Christopher Ireland for agreeing to sign on as my co-advisor, and for always being willing to share great advice and insightful discussions.

I am very grateful to all the collaborators with whom I have worked on my projects, for their invaluable contributions and helping me to enrich my work. In particular, I would like to thank Prof. Paul Dyson, Prof. Grigoris Itsikos, Dr. Pascal Schouwink, Dr. Natalia Gasilova, Dr. Mounir Mensi, Dr. Emaad Oveisi, and Seriy Saris. I would like to express my gratitude to the members of my thesis committee, Prof. Richard Friend, Prof. Paul Dyson, Prof. Giulia Grancini, and Prof. Andreas Züttel, for taking the time to evaluate my thesis and provide feedback on my work. I would also like to thank Prof. Giovanni de Micheli (Nanni) for taking the time to give me supportive advice when I needed it.

The group of people that I have worked alongside at LSMO is really more a group of friends than colleagues, and it has been an immense pleasure for me to learn and

share so much with each one of them. I would like to thank Alina for her generous friendship (from my very first days in Sion when she hosted me in her apartment), and for always finding ways to bring liveliness (and entertainment!) into the lab; Pelin for all the nice times spent together outside and lab, and for being the truly wonderful human being that she is; Bardiya for his cheerful good humour and positive attitude (especially during the memorable bead-making days!); Arun for all the chai-less chai sessions and sharing of amazing food; Sam for her inspiring creativity and go-getter attitude; Chris for his kind helpfulness, great advice, and all the delightful teacakes(!); and Serhii for his collaborations and mastery of ligand synthesis.

Many of our computational colleagues on the fourth floor do the amazing job of shedding light on processes and phenomena that experimentalists like myself can simply not measure. I have had the pleasure of working closely with many of them during the last year of my doctorate, and I would very much like to thank Maria, Ozge (my hiking, biking buddy), Kevin, Daniele, and Amber, for their valuable collaborations, from which I have learnt a great deal. Much of this thesis was written during the Covid-19 pandemic, which would have been a very different experience were it not for all rest of the fourth-floor residents, who came up with stimulating collaborative projects and learning tools to help us experimentalists keep doing science in lockdown. A very special thanks also goes to our dear Evelyn, who skilfully kept us engaged in fun conversations every day of the lockdown, and who is always available to listen, help, and cheer us up.

I would like to thank the many former members of LSMO with whom I have had the pleasure of working. Tu for the nice introduction to MOF characterisation and for many discussions; Andrzej (LSMO's 'high priest' of MOF crystals) for all his meticulous work and enjoyable collaborations, Sylvain, the best desk buddy that a person could ask for; and Aylin and Nancy for their bubbly personalities and enthusiasm in the lab.

I feel so lucky to have had the love and friendship of some very special people throughout all the ups and downs of my PhD. A very special thank you to Hina, Hoda, Rebecca, and Anita. I am very grateful to have you in my life and no amount of distance can really separate us!

While the journey that brought me to LSMO has been an unconventional one, it has always been rich and colourful, and there isn't a thing that I would change about it. For this, I am grateful to my family. My parents, brother, and sister, have been the

best support system that anybody could ask for, always encouraging me to challenge myself, cushioning my stumbles, and inspiring me to never stop exploring. Thanks dad, for teaching me to be tough, to believe in myself, and find ways to see the humour in everything. Mum, for being the ultimate comfort, for your gentle soul, and for being the model of human kindness that all of us should aspire to. Hassan, for always having my back, giving me endless confidence boosts, and having good advice at hand every time I need it. My amazing sister Seham, my real-life superhero, and my biggest source of inspiration. You have inspired me throughout my life to be a better person in every single way, and I wouldn't be who I am without you. I cannot forget to acknowledge Mika, (who just might read this thesis one day!) for bringing our family endless amounts of joy every day. And Shamim, for her knowledge, wisdom, and love. To my partner Gio, I am grateful every day; for sharing my love for science, nature, and so much more; for always making me laugh; and for letting no task or challenge seem too big for me to take on. Last but not least, I am grateful for Peanut, who hopped into my life on her three little legs two years ago, and has brought us so much happiness every day since.

Sion, 25 June 2020

Mish

Abstract

The work presented in this thesis is focused on the design and discovery of new luminescent, porous, crystalline materials for targeted applications. In particular, we focus on luminescent *Metal-Organic Frameworks* (MOFs) and *Organic Molecules of Intrinsic Microporosity* (OMIMs), both belonging to emerging classes of synthetic materials that are particularly promising due to their porosity, modularity, and the many dynamic photophysical processes that can be exploited within them. While there is great potential for these types of materials, their relatively recent discovery, less than two decades prior to the writing of this thesis, means that they are still in early stages of development and so very few examples exist that demonstrate the potential for real-world applicability. Challenges persist in achieving targeted design, high stability, or processing for integration into devices. The aim of this thesis is consider new ways of strategically designing MOFs and OMIMs that may be carried a step closer to real-world application. With problems like excess energy consumption and the depletion of clean air and water supplies on the rise in today's world, applications that can have a positive impact on the environment are of particular interest. We present a luminescent MOF that is capable of detecting trace amounts of fluoride contaminations in drinking water down to the *parts per billion* (ppb) range. The interactions of this MOF with fluoride in aqueous solutions are simultaneously electrostatic and specific in nature because of the carefully designed structure of its active site. This allows the material to be easily regenerated and used over 10 cycles, setting it apart from most existing molecular and polymeric fluoride sensors. We combined our MOF with a portable prototype sampling device that was designed and built in-house to measure fluoride concentrations in natural groundwater samples taken from three different countries, with the results showing excellent agreement with ion chromatography analysis. The strategy that we use to obtain this selective yet reversible interaction can be applied to the design of new MOFs that work on a similar principle. In addition, we present a new OMIM that exhibits broad spectrum, tuneable white light emission. The structural components and pore environment of the OMIM contribute

to it having a high quantum yield in addition to tuneability that can be controlled by guest molecules. Using this material, we obtain the highest thus-far reported value of photoluminescence quantum yield for a single-species white-light emitter, with a nearly pure-white emission colour. This has promising implications for the fabrication of new, energy-efficient *Organic Light-Emitting Diode* (OLED) devices. In addition, introducing structural changes to the base ligand of this OMIM allows us to obtain an even greater range of colour tuneability as well as new features of guest-host chemistry.

Keywords: Metal-Organic Frameworks, Porous Organic Molecules, Luminescence, Sensing, White-Light Emission



Sommario

Il lavoro presentato in questa tesi si incentra sulla scoperta e la progettazione di nuovi materiali porosi e luminescenti per specifiche applicazioni. In dettaglio, ci interessiamo di reticoli metallorganici (MOFs) e molecole organiche porose (OMIMs) luminescenti. Entrambi appartengono a una classe di nuovi materiali sintetici che, grazie alla loro porosità e modularità, sono particolarmente promettenti per le possibilità che offrono nell' utilizzo in vari processi fotofisici. Sebbene questi materiali abbiano un enorme potenziale, il fatto che siano stati scoperti solo circa 20 anni prima della stesura di questa tesi, comporta che siano ancora in una fase iniziale del loro sviluppo, con pochi esempi che ne dimostrino l'applicabilità in situazioni reali. Le più grandi difficoltà che persistono per questi materiali sono il controllo della loro struttura, la loro stabilità e lo sviluppo di processi per l'integrazione in dispositivi. Questa tesi si incentra sullo studio di nuovi metodi per la progettazione mirata di MOFs e OMIMs, per renderne possibile l'applicazione nella quotidianità. Tra le applicazioni che suscitano il maggior interesse spiccano quelle che possono avere un impatto positivo sull'ambiente, mirate per esempio alla riduzione del consumo di energia o alla salvaguardia delle risorse idriche. Il primo materiale che presentiamo è un MOF luminescente per la rivelazione di tracce di fluoro che possono contaminare acqua potabile. Questo MOF si basa sull' interazione debole e reversibile, ma tuttavia altamente selettiva, con gli ioni di fluoro. Questa interazione genera una risposta ottica che quantifica la concentrazione di ioni di fluoro in un campione fino a valori di parti per miliardo. La strategia usata per ottenere questa interazione reversibile e altamente selettiva può essere applicata alla progettazione di nuovi MOF sfruttando principi simili. Presentiamo inoltre un nuovo OMIM che esibisce un' emissione cromaticamente regolabile di luce bianca ad ampio spettro. I componenti della struttura dell' OMIM e l'ambiente all'interno dei suoi pori contribuiscono a conferirgli un'alta resa quantica e la peculiare caratteristica di poter regolare l' emissione controllando le molecole presenti all'interno dei pori. La possibilità di introdurre diversi ligandi in questo OMIM può permettere di ottenere un' ancora maggiore regolazione cromatica, nonché

la possibilità di esplorare nuove caratteristiche dell'interazione chimica tra l'OMIM e le molecole nei pori.

Parole Chiave: Reticoli Metallorganici, Molecole Organiche Porose, Luminescenza, Sensori, Emissione di Luce Bianca



Contents

Acknowledgements	i
Abstract / Sommario	v
List of figures	xi
List of tables	xiii
List of Acronyms	xv
1 Introduction	1
1.1 Aim and Scope of the Thesis	4
1.2 Metal-Organic Frameworks	6
1.3 Organic Molecular of Intrinsic Microporosity	9
1.4 Thesis Overview and Key Accomplishments	13
1.5 Thesis organization	15
2 Mechanisms of Photoluminescence	17
2.1 Photophysics of luminescent materials	18
2.1.1 Spectroscopic selection rules	20
2.1.2 Exceptions to the selection rules	21
2.1.3 Absorption processes	21
2.1.4 Dark excited-state processes	24
2.1.5 Emission processes	25
2.1.6 Luminescence in MOFs and OMIMs	28
2.2 Characterisation of light emission	30
2.2.1 Steady-state absorption spectra	30
2.2.2 Photoluminescence quantum yield	31
2.2.3 Steady-state emission spectra	31
2.2.4 Transient photoluminescence	32

2.3	Conclusions	32
3	A Luminescent MOF for Sampling Water Quality	33
3.1	A Brief Overview of Chemical Sensors	34
3.2	Integrating MOFs into sensor devices	37
3.2.1	Design of Luminescent MOF sensors	39
3.3	A Luminescent Ln-MOF for sensing trace contaminants in drinking water	42
3.3.1	Design and synthesis of Sion-105	44
3.3.2	Calibration of Sion-105 for fluoride	47
3.3.3	Structural Advantages of Sion-105	52
3.3.4	Integration of Sion-105 into a portable device	58
3.4	Conclusions	59
4	A Luminescent OMIM for White Light Emission	61
4.1	White Light Emission	62
4.2	Characterising white light emitters	64
4.3	A Bio-inspired, Single-species, White-light Emitter	66
4.3.1	Luminescence of D-Luciferin	66
4.3.2	Synthesis and Structure of Cu ₂ L ₃	68
4.3.3	Optical Properties of Cu ₂ L ₃	71
4.3.4	Cu ₂ L ₃ as a Molecular Model for luciferin@luciferase Complexes . .	76
4.4	Conclusions	79
5	Conclusions and Future Perspectives	81
5.1	Future Perspectives	82
	Bibliography	99
	Curriculum Vitae	101

List of Figures

1.1	MOFs and OMIMs	1
1.2	Applications of luminescent materials	3
1.3	Shape-directing components of MOFs	7
1.4	How MOF building units determine overall topology	8
1.5	The presence of open-metal sites in MOF structures	10
1.6	The way that OMIMs pack	11
1.7	Examples of molecular crystals that were found to be OMIMs	12
2.1	Jablonski diagram	19
2.2	Mechanisms of photon absorption in MOFs	23
2.3	Energy transfer processes	26
2.4	Stokes shift	27
2.5	Photophysical mechanisms in MOFs	29
3.1	Overview of chemical sensors	35
3.2	Incorporating MOFs into micromechanical sensors	36
3.3	The process of developing a MOF sensor	38
3.4	Structure and proposed luminescence mechanism of Sion-105	45
3.5	Crystal structure of Sion-105	46
3.6	Stability and porosity of Sion-105	47
3.7	Luminescence properties of Sion-105	49
3.8	Response time of Sion-105	51
3.9	Phosphorescence spectra of Gd-Sion-105	52
3.10	Sion-105- F^- interactions	54
3.11	Stability of Sion-105 in aqueous salt solutions	55
3.12	Binding site of Sion-105	56
3.13	Selectivity of Sion-105 to fluoride	57
3.14	Sion-105-based portable sensor	59

4.1	Structure of a stacked WOLED device	63
4.2	Characterising the colour of white light	65
4.3	Bioluminescence in beetles	67
4.4	The Cu_2L_3 complex	70
4.5	Crystal structure of Cu_2L_3	71
4.6	Optical properties of Cu_2L_3	73
4.7	Structure and emission of predicted Cu_2L_3 -like complexes	74
4.8	Tuneable luminescence spectrum of Cu_2L_3	75
4.9	Solvent adsorption sites and probability density plots of Cu_2L_3	76
4.10	Comparison of Cu_2L_3 to crystallised oxyluciferin	79
4.11	Comparison of water adsorption in Cu_2L_3 and luciferase pocket	80

List of Tables

3.1	Results of Eu-ICP-OES analysis of Sion-105 after introducing F^-	53
3.2	Contents of bottled mineral water tested using Sion-105.	57
3.3	ppm Concentrations of F measured in three groundwater samples taken from wells in Vietnam (GW1), the U.A.E. (GW2), and Saudi Arabia (GW3). Results of measurements via ion chromatography and Sion-105 show strong agreement.	60
3.4	Comparison of Sion-105 with existing MOF-based F^- - anion sensors for drinking water sampling	60

List of Acronyms

Alq3	<i>tris (8-hydroxyquinoline) aluminium</i>
BET	<i>Brunauer–Emmett–Teller</i>
CIE	<i>International Commission on Illumination</i>
CT	<i>Charge-Transfer</i>
D-A	<i>Donor-Acceptor</i>
DEE	<i>Dexter Electron Exchange</i>
DFT	<i>Density Functional Theory</i>
EDX	<i>Energy-Dispersive X-ray Spectroscopy</i>
EL	<i>Electroluminescence</i>
EQE	<i>External Quantum Efficiency</i>
ESIPT	<i>Excited-State Intramolecular Proton Transfer</i>
ESPT	<i>Excited-State Proton Transfer</i>
ET	<i>Energy Transfer</i>
ETM	<i>Electron Transport Material</i>
FRET	<i>Förster Resonance Energy Transfer</i>
FWHM	<i>Full Width at Half Maximum</i>
HOMO	<i>Highest Occupied Molecular Orbital</i>
HTM	<i>Hole Transport Material</i>

IC	<i>Internal Conversion</i>
ICP-OES	<i>Inductively-Coupled Plasma Optical Emission Spectroscopy</i>
IQE	<i>Internal Quantum Efficiency</i>
ISC	<i>Inter-System Crossing</i>
ITO	<i>Indium Tin Oxide</i>
LED	<i>Light-Emitting Diode</i>
LLCT	<i>Ligand-to-Ligand Charge Transfer</i>
LMCT	<i>Ligand-to-Metal Charge Transfer</i>
LOD	<i>Limit Of Detection</i>
LUMO	<i>Lowest Unoccupied Molecular Orbital</i>
MLCT	<i>Metal-to-Ligand Charge Transfer</i>
MMCT	<i>Metal-to-Metal Charge Transfer</i>
MOF	<i>Metal-Organic Framework</i>
NaF	<i>Sodium Fluoride</i>
NIR	<i>Near-Infrared</i>
OLED	<i>Organic Light-Emitting Diode</i>
OMIM	<i>Organic Molecule of Intrinsic Microporosity</i>
OPO	<i>Optical Parametric Oscillator</i>
PLQY	<i>Photoluminescence Quantum Yield</i>
ppb	<i>parts per billion</i>
ppm	<i>parts per million</i>
PPV	<i>poly(p-phenylene vinylene)</i>

PSM	<i>Post-Synthetic Modification</i>
PXRD	<i>Powder X-Ray Diffraction</i>
QCMs	<i>Quartz-Crystal Microbalances</i>
QD	<i>Quantum Dots</i>
SBU	<i>Secondary Building Unit</i>
SEM	<i>Scanning Electron Microscopy</i>
SV	<i>Stern-Volmer</i>
TGA	<i>Thermo-Gravimetric Analysis</i>
THF	<i>Tetrahydrofuran</i>
UV	<i>Ultra-Violet</i>
UV-vis	<i>UV and visible</i>
WOLED	<i>White Organic Light-Emitting Diode</i>
XPS	<i>X-ray Photoelectron Spectroscopy</i>

1

Introduction

The urgent environmental crises of the 21st century include increasing energy consumption, depletion of clean air and water supplies, and leaching of chemical toxins into environmental resources. With many of these problems on the rise, significant research efforts must be directed towards new solutions to both clean up and mitigate further environmental damage. Important applications include the detection and capture of air- and water-borne chemical toxins, and the development of new alternatives to widely-used, energy-intensive electronic devices, to reduce global energy consumption. A significant portion of such efforts may progress with the help of porous, functional materials that are carefully designed to perform targeted functions.

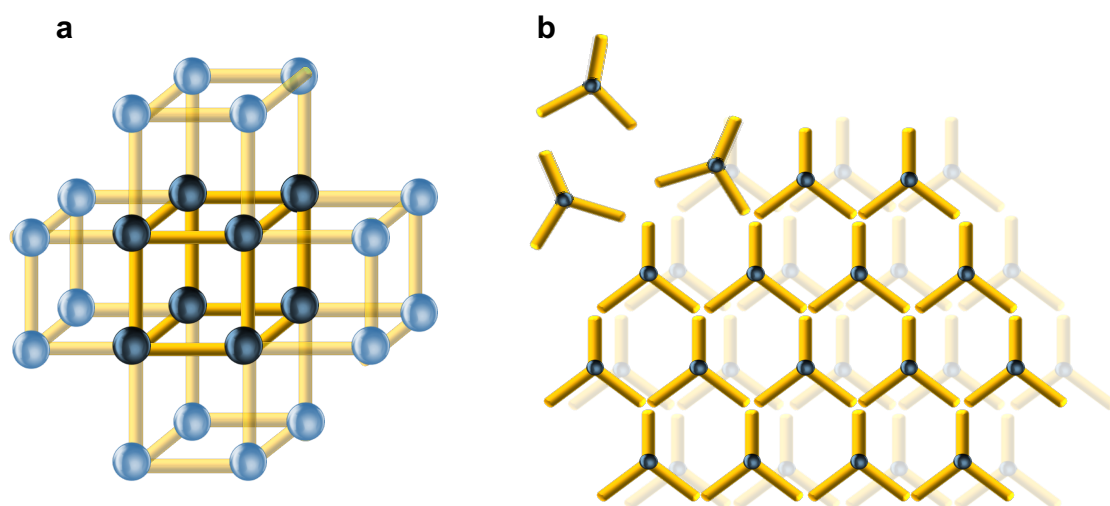


Figure 1.1 – MOFs and OMIMs. **a.** MOFs are porous, crystalline coordination networks formed from organic ligands linked together by metallic ions or clusters. **b.** OMIMs are porous molecular crystals whose porosity arises due to the formation of intermolecular voids when the molecular substituents pack.

In particular, *Metal-Organic Frameworks* (MOFs) and *Organic Molecules of Intrinsic Microporosity* (OMIMs), depicted in Figure 1.1, have been gaining popularity for a range of applications, from gas capture, separation, and storage, to chemical sensing, catalysis, and white light emission [1, 2]. MOFs are porous, crystalline coordination networks consisting of organic linkers held together in a periodic pattern by metallic vertices. OMIMs on the other hand, are molecules, typically with bent, angular, or otherwise ‘awkward’ shapes, that pack together leaving intermolecular void spaces when they crystallise [3]. Their porosity is therefore extrinsic in nature. While the regular crystalline porosity of these types of materials gives them an advantage in many applications that rely on host-guest chemistry, their most valuable features are their chemical and structural versatility. The range of organic and inorganic substituents that can be combined in the synthesis of MOFs and OMIMs is virtually infinite. This provides material scientists with a bottomless toolkit from which to construct new materials with precise desirable properties.

The selection of light-emitting, or luminescent, components to construct these materials is of particular interest because of the ease with which we can interact with light. Incorporating luminescent materials into devices for sensing, for example, makes it possible to detect a microscopic trigger event simply by eye. More importantly, luminescent materials, whether incorporated into mobile phone and computer displays, or used in artificial lighting, facilitate our interaction with the world around us.

One of the most striking demonstrations of the impact of luminescent materials discovery is seen in the evolution of lighting systems. Incandescent light bulbs and fluorescent lamps were the peak of artificial lighting technology for decades. Incandescent bulbs generate light by heating resistive tungsten filaments, while fluorescent lamps rely on the excitation of a light-emitting phosphor material by mercury vapour inside the bulbs. The standard efficiencies of these devices are around 2% to 10% [6, 7]. In 1993, the combined efforts of Shuji Nakamura, Isamu Akasaki, and Hiroshi Amano resulted in the first bright blue *Light-Emitting Diodes* (LEDs), based on gallium nitride (GaN) [8–10]. Combining these blue LEDs with existing red and green LEDs resulted in the very first white LEDs. These devices were quickly commercialised to make solid state lighting solutions that consume 75% less energy than traditional lights while lasting around 25 times longer [11]. Within a decade of the discovery, governments across the globe would ban the manufacture and sale of incandescent light bulbs [12], as LEDs began to widely substitute traditional indoor and outdoor lights.

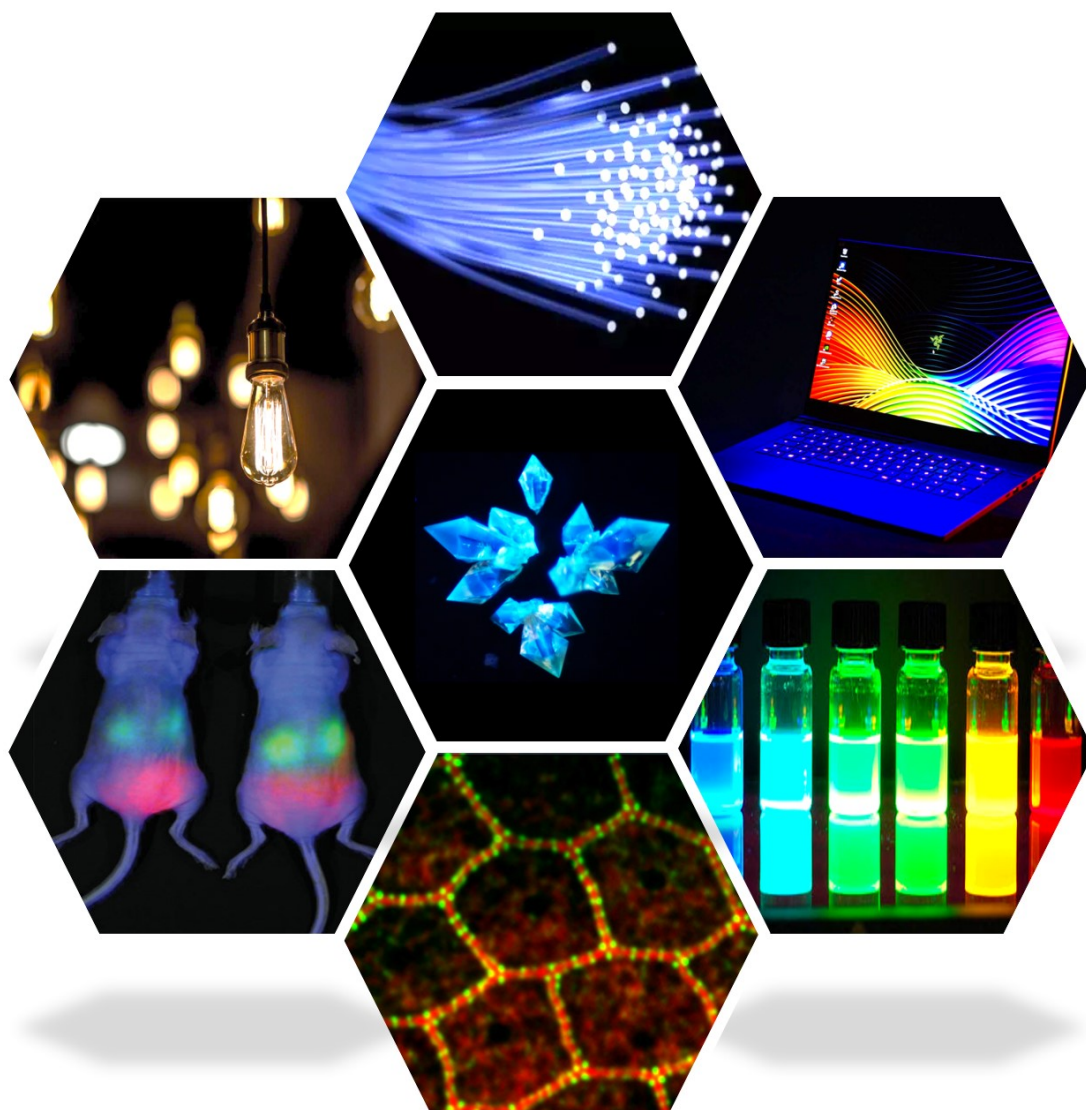


Figure 1.2 – Applications of luminescent materials. Luminescent materials have an extensive range of applications, including (clockwise from top) optical communication, display technology, sensing, in-vitro [4] and in-vivo [5] bio-imaging, and ambient lighting. Images reproduced with permission.

The discovery of novel, bright, efficient luminescent materials can equally impact a wide range of different applications. Some examples, highlighted in Figure 1.2, include communication, display lighting, biological imaging, and sensing. Organic and hybrid luminescent materials are particularly relevant to imaging and sensing applications. Bio-

logical imaging, both in-vitro and in-vivo, enables the visualisation of biological building blocks and processes. It is usually carried out by ‘tagging’ enzymes or proteins with fluorescent molecules (i.e. ‘probes’) that selectively bind to them, and then imaging them with high-resolution optical microscopy [13]. While the capabilities of fluorescence microscopy are extremely sophisticated, there is opportunity for developing new fluorescent probes that exhibit greater optical stability and brightness [14]. In-vivo imaging in particular can benefit from efficient probes with near-infrared emissions, to minimise the amount of fluorescence signal that is reabsorbed by surrounding tissue. For chemical sensing, organic and hybrid luminescent materials have a greater degree of chemical tuneability than inorganic compounds and can therefore be designed to selectively target desired analytes. Optical signals are among the simplest means of registering sensing events, as changes in luminescence can be quantified and converted into digital values with the help of commercially available optoelectronic components. Combining the applicability of luminescent compounds with the advantages of porous crystals results in a fascinating sub-class of materials with expansive potential, that hold relevance in multiple frames of reference. This sub-class of materials that are luminescent, porous, and crystalline, is explored in this thesis.

1.1 Aim and Scope of the Thesis

The primary applications of MOFs, OMIMs, and other porous crystalline materials have largely been gas capture and storage. However, most of the organic ligands that are used to construct these materials, with their aromatic nature, tend to be luminescent under *Ultra-Violet* (UV) excitation. Coordinating these ligands to metal centres, *e.g.* in the formation of MOF¹ structures, can result in interesting changes in their luminescence spectra, with different metal centres giving rise to different optical properties. In addition, the fixation of luminescent organic ligands into rigid structures with regularly repeating periodicity gives rise to interesting optical effects that may not be observed in their uncoordinated, molecular form. Such effects are demonstrated in the large, and rapidly increasing, number of publications that have focused on the synthesis and application of luminescent MOFs over the past decade [17, 18]. By thus paying attention to their luminescence properties, one can leverage what might be an otherwise untapped advantage that is inherent to the structure of these materials. This realisation has cultivated a

¹While OMIMs are still in relative infancy and fewer examples of luminescent OMIMs exist [15, 16], the same set of principles that concern luminescent MOFs may be applied to OMIMs as well.

wide range of creative synthetic strategies and applications for luminescent MOFs in recent years. For example, MOF-based optical sensors exploit their porosity and chemical tuneability along with their luminescence to provide simultaneous detection and signal transduction [19]. Luminescent MOFs have been designed for bioimaging applications, in which their pores provide the dual functionality of also hosting guests such as small-molecule drugs [20]. Light-emitting MOFs have been exploited to enhance the activity of photocatalytic systems [21,22], and have even been designed to demonstrate frequency upconversion, whereby low frequency incident light is converted into high-frequency emitted light [23]. One important aspect of investigating luminescent MOFs and OMIMs is that their inherent crystallinity makes it easier to shed light on photophysical processes taking place within them. In many cases, substituting the metal that forms the nodes of MOFs, for example, results in a topologically identical structure that exhibits entirely distinct optical properties. By judicious selection of the components, and careful analysis of the resulting optical behaviour, it becomes possible to infer what dynamical processes may be occurring in the material on a molecular level. A far-reaching consequence of access to such insights is the potential for targeted design of luminescent materials for desired applications. Both OMIMs and MOFs, being roughly one and two decades old respectively, are in the relatively early stages of their development. While they hold immense potential for use in a variety of applications, very few examples exist so far that demonstrate real-world pertinence. Being able to investigate and better understand the processes occurring in the material on a molecular level can help guide the targeted design of materials that come closer to real-world use.

This brings us to the aim of this thesis, which is to design new materials of the emerging MOFs and OMIMs class, and carry them a step closer to real-world application. We exploit the broad and exciting landscape encompassing porous, luminescent crystals, with a particular focus on applications that positively impact the environment. With the depletion of safe and clean drinking water sources in mind, we present a luminescent MOF capable of sampling trace amounts of targeted chemical contaminants from drinking water in the presence of a range of potential interferences. We describe a hand-held sensor that we designed and built for use with our MOF for sampling untreated ground water. With the consideration of the high cost and energy expense of lighting technologies, we report a novel strategy to synthesising stable, colour-tuneable, and high-efficiency white light emitters, inspired by bioluminescent organisms. In order to place considerations for the design and synthesis of such materials into context, we first provide a general introduction to MOFs and OMIMs in the following section.

1.2 Metal-Organic Frameworks

Metal-organic frameworks evolved from coordination compounds, which consist of metal ions, connected via coordination bonds (i.e. non-covalent interactions), to organic molecules or ligands. The first examples of crystalline coordination compounds with 2- and 3-dimensional periodicity appeared in the form of clathrates; cage-like crystals whose structures are maintained by the presence of small guest molecules trapped within the cavities of the host lattice [24]. Their discovery in the 1950s inspired the development of extended coordination networks that consisted of inorganic nodes linked together by organic ligands to form net-like structures [25]. The ease with which the length of ligands used in the synthesis of these coordination networks could be varied, resulted in the emergence of a variety of different coordination network architectures [26]. While many of these structures possessed cage-like voids, the size of the voids was limited by the tendency of long linkers to entangle during synthesis, resulting in interpenetrated nets [27]. Furthermore, since the voids would form by encasing guest molecules during synthesis, these materials suffered from inherent instability whereby activation (removal of the guest molecules, e.g. by applying heat and vacuum) resulted in the collapse of the crystalline structure. The first example of a crystalline coordination network that exhibited permanent porosity (i.e. that maintains its structure and porosity upon activation) was reported by Omar M. Yaghi and coworkers in 1995 in the form of MOF-2 [28]. With metal clusters in the form of dinuclear Cu^{2+} paddlewheels as the nodes and charged, chelating, 1,4-benzene dicarboxylate (BDC) ligands as linkers, MOF-2 was the first example of a definitive MOF structure. Permanent porosity could be achieved in part due to the chelation of Cu^{2+} ions to form the paddlewheel clusters. This afforded more rigidity to the overall structure than nodes composed of single metal ions would, while the use of charged linkers increased the coordination bond strength. The combination of factors paved the way for new strategies in MOF synthesis.

As illustrated in Figure 1.3, the two key components of MOFs - the metal nodes and the organic linkers - determine their overall shape and topology. In structures where the metal nodes consist of polynuclear clusters rather than single ions, the geometry of the cluster controls the directionality and the connectivity of the net. For this reason, polynuclear metal clusters are described as *Secondary Building Unit* (SBU) in MOF structures. One of the most well-studied MOFs for example, MOF-5 (depicted in Figure 1.4a), consists of octahedral Zn_4O SBUs that hold the connecting BDC linkers in a perpendicular fashion to form a cubic net with open, scaffold-like pores [30]. Remarkably,

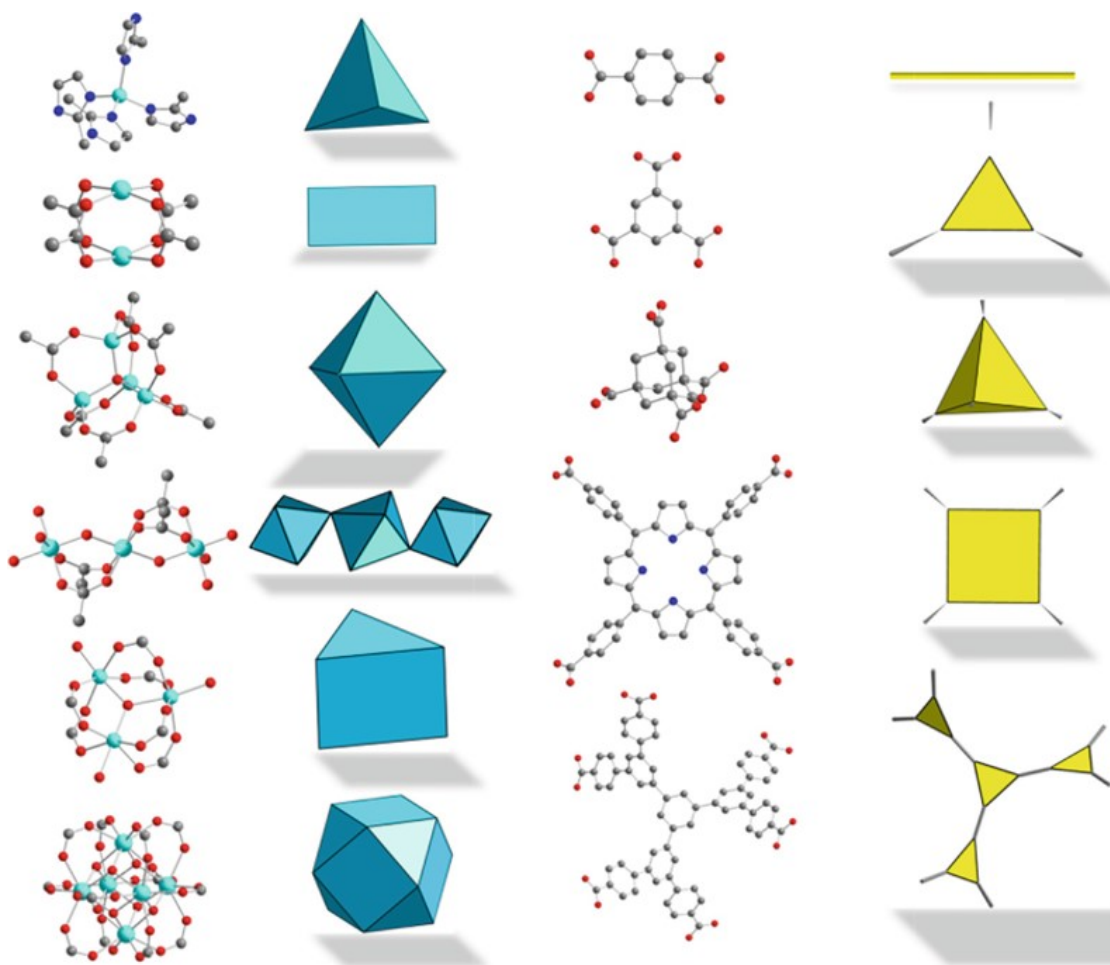


Figure 1.3 – Shape-directing components of MOFs. **a.** Some examples of inorganic SBU geometries, and **b.** Linker geometries and topocities that dictate the structure of the MOF coordination network. Reproduced with permission from [29]

it was found that increasing the length of the linear linker resulted in the formation of scaled nets with otherwise identical topologies to the original MOF-5. These scaled structures were described as ‘isorecticular’ structures, and formed the first isorecticular MOF (IR-MOF) series [31] shown in Figure 1.4a. The geometry of the organic linker used in MOF synthesis equally contributes to the resulting structure topology. For example, using the trigonal, tri-topic, benzene-1,3,5-tricarboxylate (BTC) as the linker resulted in the formation of spherical cages seen in the MIL-100 series of MOFs [32], where the name MIL represents the birthplace of the series, the Materials Institute Lavoisier. Coordination of BTC with trivalent metals tends to favour the formation of MO_6 octahedra (M = metal) depicted in Figure 1.4b, allowing the node metal used in MIL-100 synthesis to be easily substituted. Isostructural analogues of MIL-100 could

therefore easily be formed using Al, In, Cr, and Fe. The diverse SBU geometries, linker lengths, and linker topocities that can be combined in MOF synthesis have led to an exponential growth in reports of new, highly porous MOF structures over the past two decades.

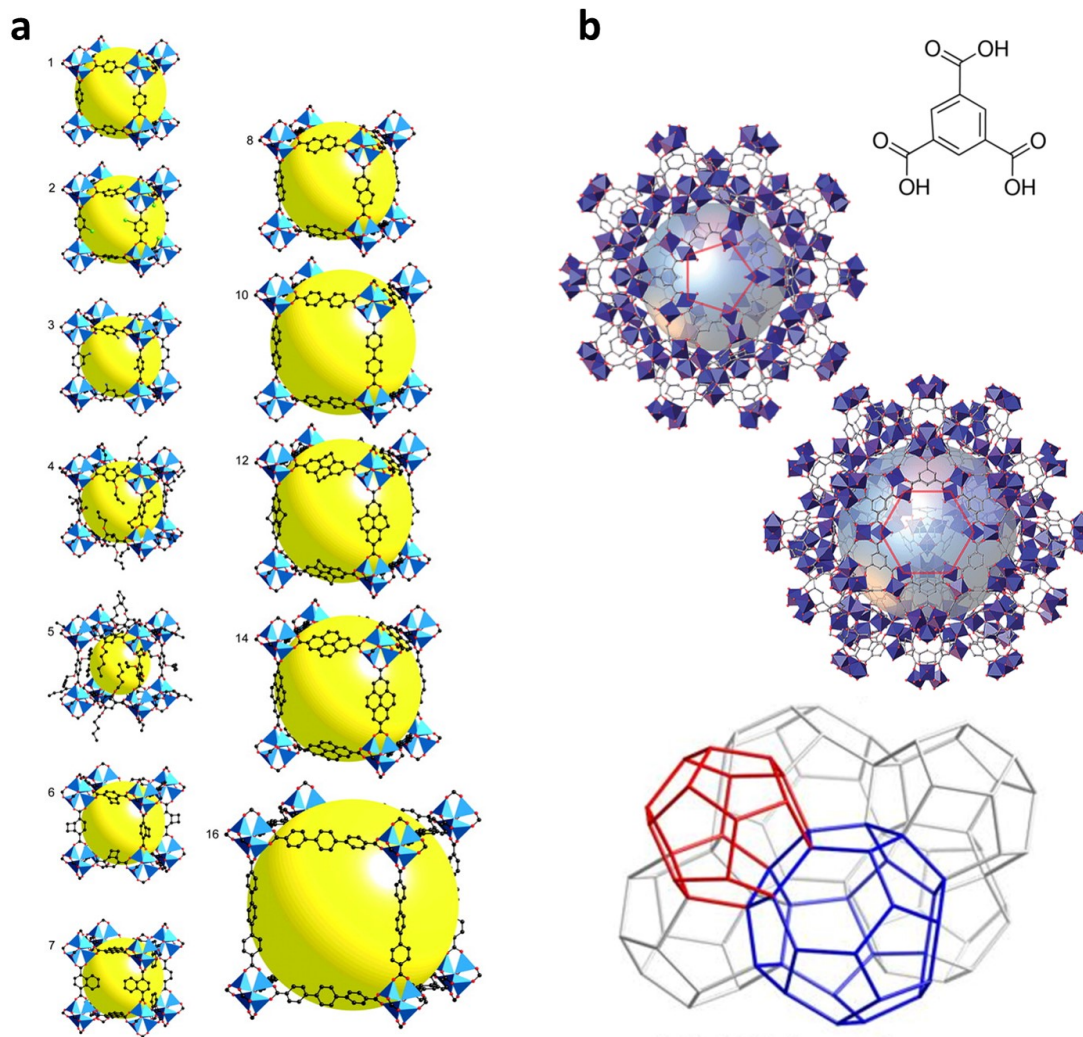


Figure 1.4 – The earliest exemplary MOF structures demonstrate how building units determine overall topology. a. MOF-5 maintains its cubic geometry resulting in an isorecticular series of MOFs (IR-MOFs) [31], and **b.** The use of tritopic BTC in the synthesis of MIL-100 results in the formation of two types of pores [33] with large spherical cavities [34]. Images reproduced with permission.

Owing to the exceptional porosity that could be achieved with linker elongation, the earliest applications of MOFs were largely focused on gas capture and storage. However, the ease with which chemical functionality could be introduced into either the MOF SBUs or linkers led to a rapid expansion in their applicability. MOFs in which the SBUs

consist of partially uncoordinated open metal sites, for instance, are widely used for catalytic reactions and selective separation of gases [35, 36]. There are two common ways of incorporating open metal sites into MOF structures, illustrated in Figure 1.5. The first arises when solvent molecules coordinate to the metal nodes during synthesis, but do not act as stabilising ligands and can therefore be removed from the structure upon activation. The exemplary HKUST-1 shown in Figure 1.5a (HKUST = Honk Kong University of Science and Technology) MOF consists of Cu^{2+} paddlewheels in which each Cu^{2+} ion is coordinated to two BTC linkers and one water molecule [37]. Removal of the water molecule under heat and vacuum results in a high density of open metal sites in the pores of HKUST-1, to which it owes its excellent performance in CO_2 capture [38], catalytic CO_2 reduction [39], and propane/propene separation [40]. The other common method of introducing open metal sites into a MOF, shown in 1.5b, is to engineer the formation of defects in the crystal during synthesis. Defect engineering involves the introduction of modulators to the synthetic reaction [41]. In the $\text{Zr}_6\text{O}_4(\text{OH})_4\text{-BDC}$ MOF, UiO-66 (UiO = Universitetet i Oslo), for example, known for its ability to maintain a high density of defects without losing crystallinity, modulators in the form of mono carboxylates like formic or acetic acid occupy metal coordination sites, resulting in ‘missing-linker’ defects [42]. Removal of these coordinated monocarboxylates creates open metal sites that can be exploited for selective gas adsorption and catalytic reactions.

Where the formation of open metal sites is not an option, the extensive opportunities offered by organic chemistry to design, synthesise, and functionalise the organic ligands of a MOF make it possible to precisely tune the chemical environment within its pores. This approach is particularly interesting for applications in the selective detection and capture of volatile organic compounds in air, or ionic or heavy metal pollutants in water.

Given these synthetic strategies, we can easily imagine the design of MOFs with desired chemical and structural properties for targeted applications. Combining the capabilities of organic chemistry with the structural diversity of SBUs in this way results in the formation of structures whose properties greatly exceed the sum of their individual components.

1.3 Organic Molecular of Intrinsic Microporosity

A class of porous crystalline materials that have emerged even more recently than MOFs are OMIMs. These are a type of porous molecular material, distinct from MOFs in

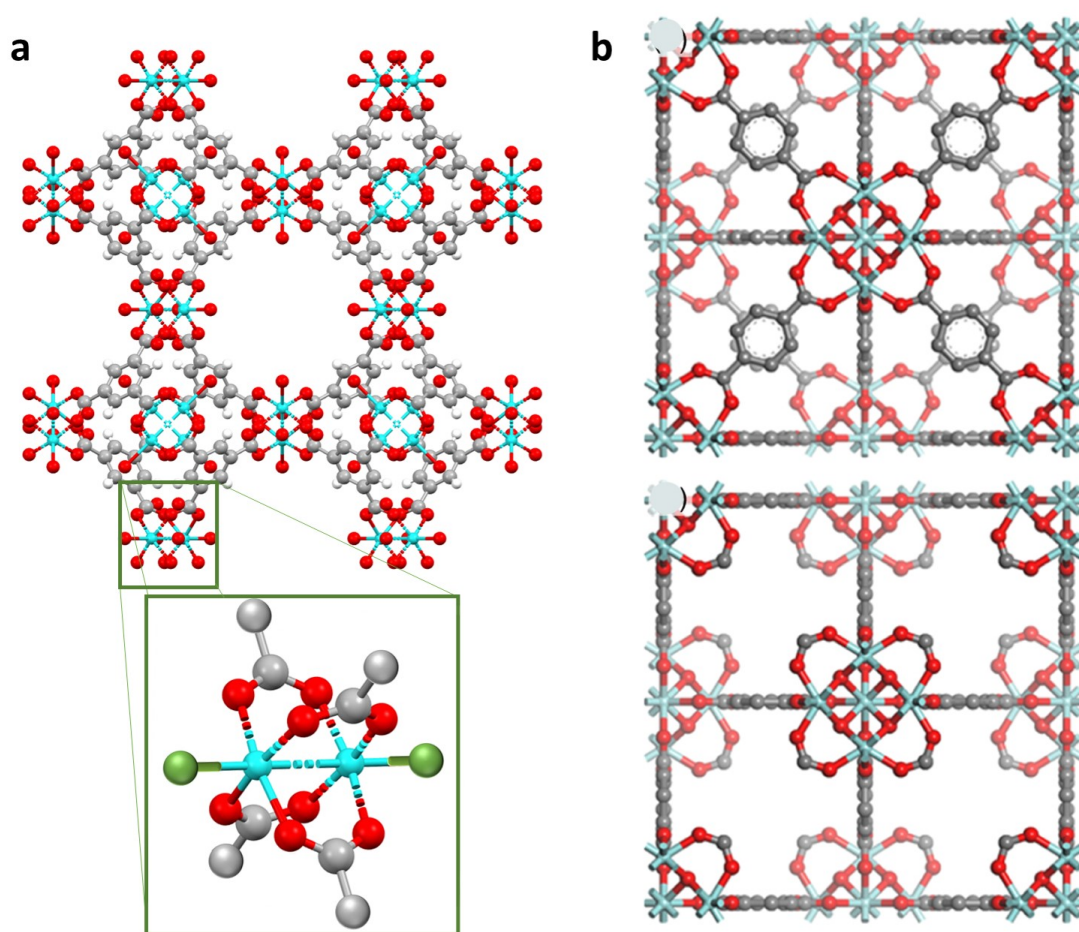


Figure 1.5 – The presence of open-metal sites in MOF structures. **a.** HKUST-1 consists of copper paddlewheels (inset) with two coordinated water molecules that can be removed upon activation, exposing open metal sites and **b.** "Missing linker" defects can be introduced to the structure of UiO-66 by including monocarboxylate modulators in the synthetic environment. Reproduced with permission from [43]

that they are discrete molecules rather than coordinated networks, and can therefore occur solvated as well as crystallised. The porosity of OMIMs arises because of their characteristic awkward shapes, which prevent close-packing of the molecules in the solid state and thus promote the formation of periodic intermolecular micropores. As with MOFs, the pore sizes in OMIMs are typically comparable to the size of small molecules, making them equally interesting candidates for capture, storage, separation, and sensing applications. Their solubility however, may offer advantages over MOFs in terms of processing. While MOFs predominantly occur as crystalline powders, solution-processability of OMIMs makes them promising for the formation of porous crystalline membranes, coatings, and films.

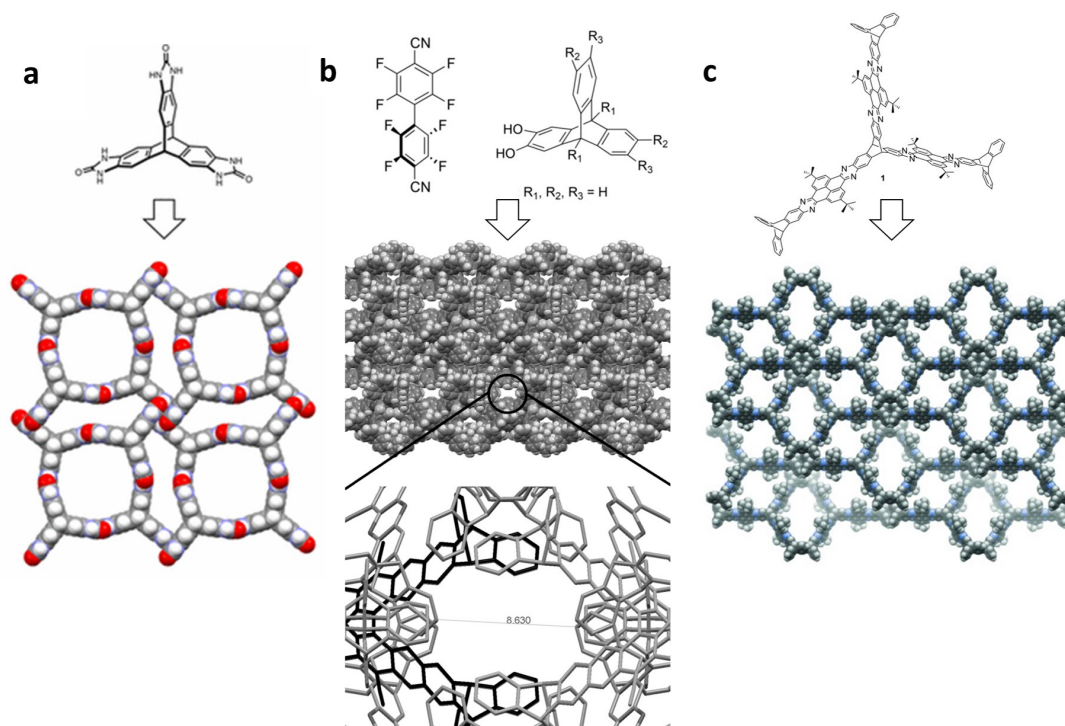


Figure 1.6 – The way that OMIMs pack. **a.** A rigid triptycene derivative self-assembles by hydrogen bonds to a porous crystal with large 1-D channels [44] **b.** Microporous OMIMs designed to frustrate packing [45] **c.** Microporous OMIM structure capable of gas sorption [46]. Images reproduced with permission.

Due to the extrinsic nature of their porosity, it is difficult to either predict which molecules might crystallise to form OMIMs, or to deduce the porous properties that a given OMIM may exhibit upon crystallisation by examination of its molecular structure alone. For this reason, the majority of porous molecular materials investigated in the last century have been in the form of molecular cages or organic polymers, with relatively few examples of crystalline OMIMs. One of the earliest examples of an OMIM is the so-called Dianin's compound, a bisphenol and acetone condensation isomer first prepared in 1891 by Russian chemist, Aleksandr Dianin [47]. The crystallisation of Dianin's compound into clathrates in the presence of guest molecules was first reported in the 1950s [48]. The molecules form six-membered rings, hydrogen-bonded via their hydroxyl groups, that stack upon each other like columns. Their bent structure was found to result in waisted, one-dimensional channels capable of reversibly adsorbing a range of guest molecules [49]. Similarly rigid, angled, aromatic molecules are more likely to form OMIMs that are stable upon activation and can be exploited for host-guest applications. Since the computational prediction of molecular crystal packing remains a challenge, OMIMs tend to be discovered rather than intentionally designed [2, 50], with the most common

identifier being a particularly low crystal density. One example, identified as an OMIM six years after it was first synthesised, is 3,3',4,4'-tetra(trimethylsilylethynyl)biphenyl [51]. Examination of the molecule's crystal structure revealed similarities to that of the microporous zeolite A, and upon successful evacuation of its pores, reversible adsorption of nitrogen and hydrogen were successfully demonstrated. While hinged or awkwardly-shaped molecules such as triptycenes [52] or propellanes have been used towards the synthesis of new OMIMs [45], the formation of multiple polymorphs during crystallisation limits the growth and characterisation of OMIM single crystals. Much of the solid-state characterisation of OMIM properties, including the adsorption and desorption of guest molecules, has therefore been carried out on amorphous samples.

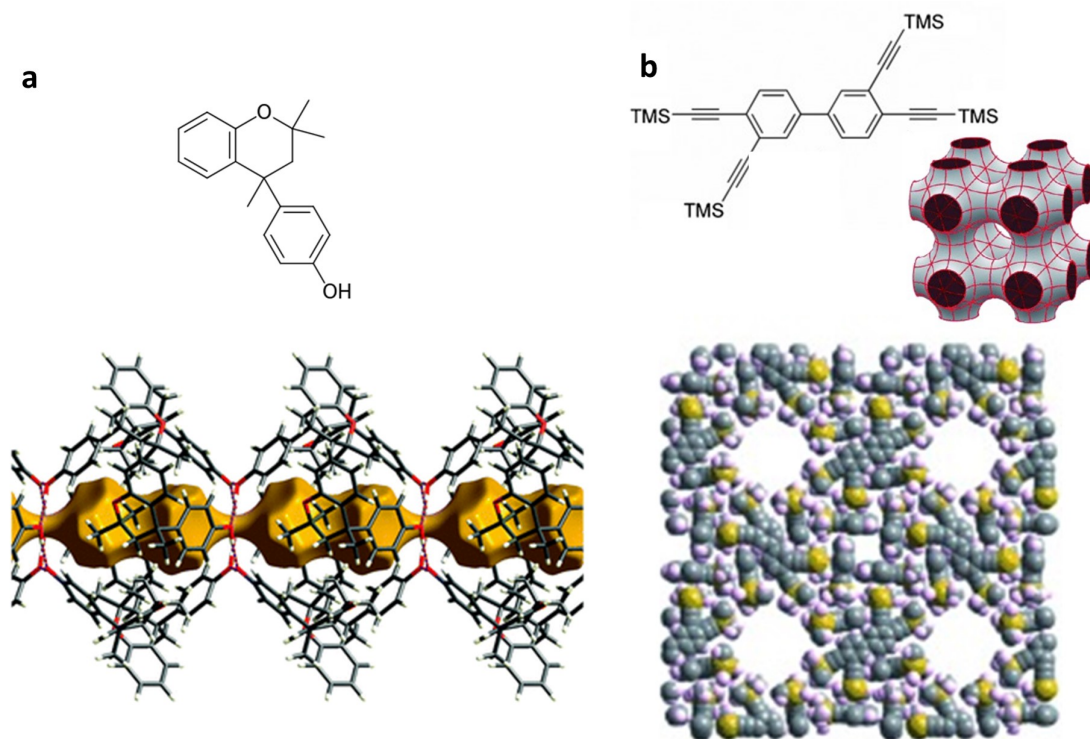


Figure 1.7 – Examples of molecular crystals that were found to be OMIMs. **a.** Dianin's compound forms a porous crystal that is capable of reversible gas capture and **b.** 3,3',4,4'-tetra(trimethylsilylethynyl)biphenyl has an open microporous structure similar to zeolite A. The inset illustrates the topological structures of the pores. TMS = trimethylsilyl. Images reproduced with permission from [53].

While OMIMs are still in relative infancy, there is plenty of opportunity for progress in the development of new structures, control of their crystallisation, and exploration of new applications.

1.4 Thesis Overview and Key Accomplishments

In this thesis, we focus on the applications-driven design of porous, crystalline materials that emit light. The advantage of these materials is threefold: porosity allows the exploitation of host-guest chemistry, e.g. for the detection and capture of pollutants in air and drinking water. Crystallinity offers a greater degree of control over material properties than can be achieved with amorphous materials. Luminescence allows us to exploit these materials as a means to interact with our environment.

With this in mind, we report the design, synthesis, and characterisation of two novel, luminescent, porous crystalline materials for applications in sensing and white light emission. We focus on hybrid organic-inorganic crystals, and demonstrate how both the inorganic and organic components can be carefully selected to contribute to the overall properties of the material in a desirable way. The sensing material presented in Chapter 3, for example, is a MOF named "Sion-105" that is designed to detect fluoride ions, a commonly occurring chemical contaminant in drinking water, particularly from wells. While non-toxic in very small amounts, fluoride ions can cause tissue damage and crippling bone deformities when consumed over long periods in concentrations as low as 2 mg/L. The organic component of Sion-105 is functionalised to target fluoride ions, while its metallic nodes, consisting of luminescent europium (Eu^{3+}) ions, serve two purposes: (i) to distort the organic ligand, resulting in the formation of micropores that selectively interact with fluoride ions to their small size, and (ii) to provide an optical signal when fluoride ions are present. The white light emitter on the other hand, presented in Chapter 4, is an OMIM named " Cu_2L_3 ", in which broad-spectrum light emission arises from the organic component, consisting of a bioluminescent molecule called luciferin. The metal nodes, composed of Cu^{1+} and Cu^{2+} ions, do not contribute to the emission colour of the complex, however by locking the luciferin molecules into a rigid structure, they enhance the intensity of light emitted. In addition, the copper nodes dictate the angular shape of the complex, which is directly responsible for its OMIM-like crystal packing.

With a particular emphasis on optical properties, we investigate how the pore shape, size, or chemical environment influence the characteristics of our materials in response to guest molecules. The small pore size of Sion-105, for example, allows for selective sensing of fluoride ions via a molecular sieving approach. Within the pore, the guest molecules are exposed to the functional group which is incorporated in the organic ligand. As explained in detail in Chapter 3, an interaction with this functional group gives rise to

changes in the MOF's Eu^{3+} -based luminescence intensity, allowing for contaminants to be quantified at trace levels. The pores of Cu_2L_3 also play a key role in its performance as a material. The optically emissive ligand contains a functional group that controls its emission colour. Guest molecules in the pores of Cu_2L_3 have access to this functional group, and tuning the concentration of guest molecules results in tuning the colour of light that is emitted. At an optimum concentration, the host-guest interactions give rise to broad-spectrum white light emission.

Finally, structure-guest molecule-material property relations are exploited to demonstrate real-world application of these materials. For Sion-105, we report a prototype of a portable, easy-to-use device for sampling the concentration of fluoride in drinking water sources. This prototype was designed and built in-house, with the support of an electronics workshop at EPFL, and was used to with a sampling protocol that requires no calibration, and gives reproducible, accurate results. The device was used to measure the concentration of fluoride ions in untreated water samples taken from wells in Vietnam, the United Arab Emirates, and Saudi Arabia, with the measurement results showing excellent agreement with results from ion chromatography. The efforts of designing, synthesising and characterising the material, investigating its optical properties, and designing, optimising, and testing the device, have culminated in an article titled "Selective, Fast-Response, and Regenerable Metal–Organic Framework for Sampling Excess Fluoride Levels in Drinking Water", published by Ebrahim et. al in the Journal of the American Chemical Society in February 2019. The tuneable, broad- spectrum light-emitting Cu_2L_3 on the other hand, is reported in the context of a new strategy for the design of materials to make *Organic Light-Emitting Diodes* (OLEDs). We demonstrate how we formed a stable crystalline structure in which simple guest molecules can be used to tune the emission, and thus obtain white light from a single emitter with amongst the highest quantum yield so far reported. We report how the range of colours that can be emitted by such materials can be tuned by introducing subtle changes into the structure of the organic component prior to synthesising the crystal. Interestingly, our investigation of the host-guest chemistry in the pores of our material provided insights into a possible mechanism by which different bioluminescent organisms are capable of emitting different colours of light; a natural phenomenon that thus far remains elusive. The design, synthesis, characterisation, and investigation of this Cu_2L_3 and its optical properties have culminated in a patent that is currently under consideration, as well as an article titled "Tuneable luminescence from a biomolecule-inspired single-species emitter of white light" by Ebrahim et. al, which is in submission.

1.5 Thesis organization

The structure of this thesis is as follows:

Chapter 2: In Chapter 2, we provide a brief, high-level summary of some of the relevant photophysical properties of molecular crystals like MOFs and OMIMs. Reviewing these concepts allows us to better understand the dynamic processes that arise in structures, including those reported in Chapters 3 and 4. It also allows us to better attempt the design of luminescent materials with desired properties, which is an interesting tool to enable continued development of the work presented here in the future.

Chapter 3: Chapter 3 introduces Sion-105. Since the aim of this project was to create a MOF-based luminescent sensor, we begin the chapter by reviewing some of the important aspects pertaining to luminescent sensor operation and design. We then explain how we used Sion-105 for our targeted application and created our hand-held prototype sensor device for water sampling.

Chapter 4: In Chapter 4, we diverge from MOFs and sensing, to OMIMs and white light. We describe our bioluminescence-inspired strategy to synthesise a tuneable, broad spectrum, single-species emitter of white light. We detail the structural and optical characteristics of this new material, and propose a mechanism for the tuneability of its emission.

Chapter 5: In Chapter 5 we summarise the key findings of the thesis, and propose future work which may be carried out to build upon each of the projects presented.

2

Mechanisms of Photoluminescence

Luminescence describes the spontaneous, non-thermal emission of light, resulting largely from chemical or biological reactions (chemiluminescence/bioluminescence) or from optical or electrical excitations (photoluminescence/electroluminescence). Luminescent materials are ubiquitous, and form integral parts of devices ranging from daily-use lighting, computer displays, and personal heart-rate monitors, to specialised industrial instruments. This expansive reliance on luminescence drives continued research into new luminescent materials that are more energy efficient, more environmentally and spectrally stable, and capable of offering better control over the colour of light that they emit. *Metal-Organic Frameworks* (MOFs) and *Organic Molecules of Intrinsic Microporosity* (OMIMs) in particular, with their modularity and structural diversity, offer many opportunities in this field. Given the range of potential of linkers, metal ions or clusters, and guest molecules that can be incorporated into such materials, a variety of photophysical phenomena can be exploited to enhance their luminescence properties. Developing such materials for targeted applications requires some consideration of the fundamental photophysical processes occurring therein.

Since the focus of this thesis is the design, synthesis, and characterisation of luminescent porous crystals for targeted applications, we begin in this Chapter with a summary of the key relevant photophysical principles. In particular, we make general distinctions between the transitions occurring in organic luminophores and luminescent lanthanide ions, and explain the mechanisms underlying the absorption and emission spectra of these different types of emitters in extended crystalline structures. We then briefly review some of the main experimental techniques used to characterise luminescent materials. These principles and characterisation techniques were used in the design and analysis of the materials presented in Chapter 3 and Chapter 4 of this thesis.

2.1 Photophysics of luminescent materials

Despite their extended crystallinities, the electronic structures of materials like MOFs and OMIMs are more similar to molecular systems rather than inorganic crystals, and therefore tend to consist of spatially localised molecular orbitals in which localised electronic transitions occur. These transitions, described briefly in the present section, can be neatly summarised in a Jablonski diagram. Named after the Polish physicist Aleksander Jablonski, this diagram serves as a visual tool to track the kinetic energy loss pathways of photoexcited molecules [54]. Transitions including absorption, fluorescence, phosphorescence, explained in this section, can be mapped onto a Jablonski diagram as shown in Figure 2.1. The horizontal black lines depict the energy levels of a molecule, with energy increasing vertically. Bold lines, labelled S_0 , S_1 , S_2 , represent the lowest vibrational level of each singlet electronic state, with S_0 referring to the ground state. Lines labelled T_1 , etc. correspond to the triplet energies of the molecule. Dotted lines represent the vibrational levels associated with the motion of atoms in the molecule. The vibrational levels of higher energy states tend to become energetically more and more closely spaced, eventually forming a continuum.

The absorption of photons by a molecule or metal complex can generate excitations that correspond in energy to the energy of the incident photon. The eventual decay from the photo-excited state back to ground state may occur radiatively, via the emission of a photon, or non-radiatively, due to thermal effects that create vibrational or rotational decay pathways. The different types of excitation and de-excitation transitions are labelled with arrows in the Jablonski diagram.

While photons in the infrared and microwave regions of the electromagnetic spectrum give rise to vibrational and rotational molecular excitations respectively, the energy needed to change the electron distribution in molecules (typically of the order of several electronvolts), corresponds to the *UV and visible* (UV-vis) region. The UV-vis absorption and emission spectra of materials therefore provide key information about the electronic transitions taking place therein. We refer to electronic transitions involving the absorption and emission of UV-vis photons as optical transitions.

Optical transitions result from the interaction of a molecule with the electric field of incident light. Therefore, a key factor in determining whether or not such transitions are allowed to occur is the molecule's transition electric dipole moment, given by Equation 2.1. When light is incident on a molecule, the action of its electric field component,

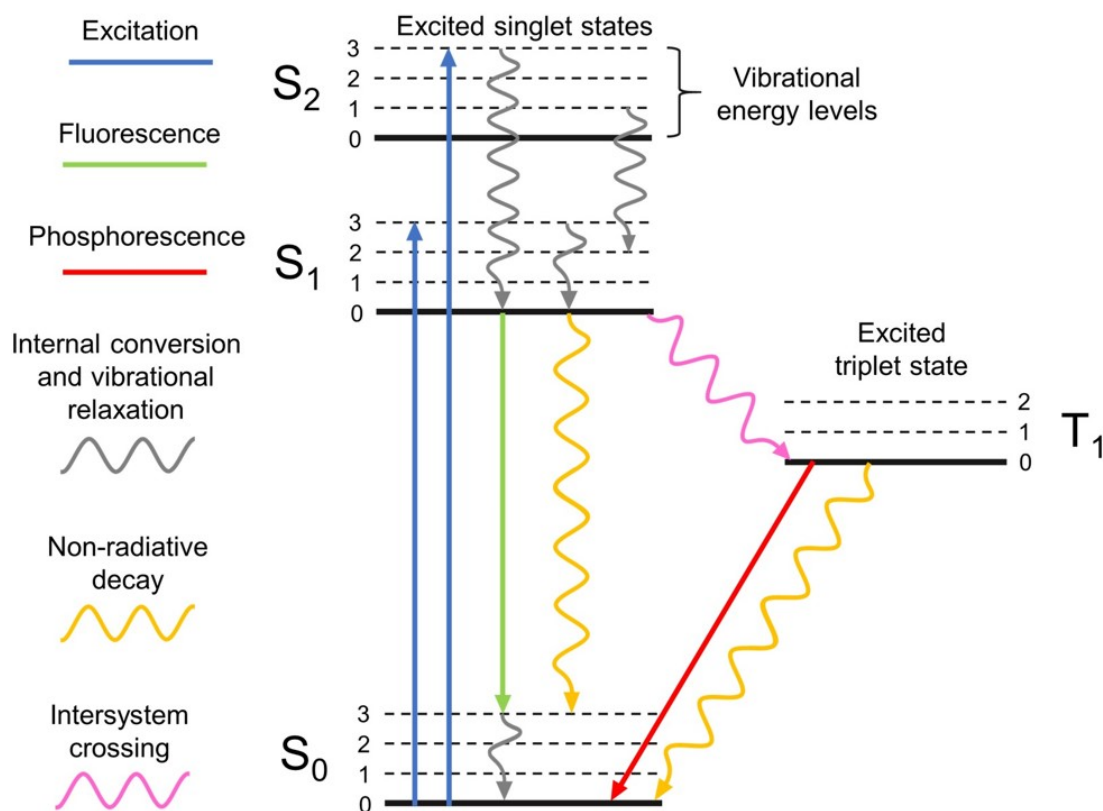


Figure 2.1 – Jablonski diagram illustrating the various transitions that may arise between the electronic states of a molecule. Electronic states, depicted by black lines, are arranged vertically by increasing energy, and grouped horizontally by spin multiplicity. States marked S refer to singlet states while states marked T refer to triplet states. Transitions involving the absorption and emission of photons are marked with straight arrows, while non-radiative processes are marked with wavy arrows.

described by the electric dipole operator $\hat{\mu}$, may cause an electron to transition from an initial state Ψ_i to a final state Ψ_f . The redistribution of charges resulting from such a transition may be dipolar in nature (i.e., the transition dipole moment, μ_{fi} , may be nonzero). An interaction with the incident light will be more likely if the molecule can host a transition whose resulting charge redistribution creates a dipole corresponding in frequency to that of the incident light. In this case, the associated transition will appear in the spectrum of the molecule. The larger the transition dipole moment, the greater

the intensity of the transition.

$$\mu_{fi} = \int \Psi_f^* \hat{\mu} \Psi_i \delta\tau \quad (2.1)$$

Not all optical transitions are allowed, and the probability of μ_{fi} being nonzero is contingent on the fulfilment of a set of selection rules, which emerge as a consequence of the conservation of angular momentum.

2.1.1 Spectroscopic selection rules

The spectroscopic selection rules state that in order for a transition to be allowed:

1. the change in spin (ΔS) during the transition must be equal to zero
2. the change in orbital angular momentum (ΔL) must be equal to 0 or ± 1 (this excludes $L = 0 \leftrightarrow L = 0$)
3. the change in total angular momentum (ΔJ) must be equal to 0 or ± 1 (this excludes $J = 0 \leftrightarrow J = 0$), and
4. only those transitions in which the wavefunction undergoes a change in parity are allowed

The first rule arises from the fact that photons, as spin-1 particles, will not affect the spin of an electron. Transitions between orbitals of the same spin state are therefore allowed, while transitions involving a change in spin multiplicity are forbidden. The second rule accounts for the need of a dipolar charge redistribution, with a unit change in orbital angular momentum, to accompany a transition. For this reason, intra-sublevel $s \leftrightarrow s$, transitions are forbidden, as are those between $s \leftrightarrow d$, $p \leftrightarrow f$, etc. The third rule accounts for the fact that even when there is a unit change in orbital angular momentum of the excited electron, the resultant total orbital angular momentum of the molecule depends on the coupling of spin and orbital angular momenta. The fourth rule applies specifically to centrosymmetric molecules, and implies that states with the same parity cannot be connected by electric dipole transitions.

2.1.2 Exceptions to the selection rules

The selection rules, which consider the angular momentum and symmetry of the molecular system, are derived under several hypotheses which are not always met in reality. They are, therefore, subject to exceptions. For example, the mixing of π -acceptor and π -donor ligand orbitals with metal d-orbitals in coordination compounds and metal complexes results in the formation of transitions that are no longer purely $d \leftrightarrow d$. This so-called ligand field splitting due to the mixing of orbitals accounts for the presence of d-d transitions in the spectra of transition metal complexes. Similarly, lanthanide ions under the influence of a ligand-field encounter non-centrosymmetric interactions that allow mixing of opposite-parity states into the 4f orbitals. As a result, $4f \leftrightarrow 4f$ transitions become weakly allowed. Exceptions arise in molecules and metal complexes containing heavy atoms, in which spin-orbit coupling is significant. This results in a partial lifting of the spin selection rule, so that spin-forbidden transitions become weakly allowed. Finally, parity-forbidden transitions in centrosymmetric complexes can become weakly allowed if the center of symmetry is disrupted, e.g. by Jahn-Teller distortion, or asymmetric vibronic transition. These exceptions typically result in a partial lifting of the selection rules, so that forbidden transitions tend to proceed at a slow rate compared to the allowed transitions, and the resulting spectral emission lines are relatively weak.

Assuming that the selection rules are either met or relaxed, the key light absorption processes occurring in MOFs and OMIMs can be considered.

2.1.3 Absorption processes

The absorption of a photon creates an excitation whereby an electron undergoes an optical transition to a higher energy state. In most crystalline semiconductors with delocalised band structures, the lowest-energy photons that can be absorbed to generate an optical transition determine the energy difference between the highest occupied and lowest unoccupied crystal bands (*i.e.*, the valence band maxima and conduction band minima, respectively). In molecular materials with high exciton binding energies like MOFs and OMIMs on the other hand, the complex structure of the molecular orbitals gives rise to highly localised optical transitions [55] that occur between the *Highest Occupied Molecular Orbital* (HOMO) and *Lowest Unoccupied Molecular Orbital* (LUMO). These transitions may be localised on a given ligand, or they may involve charge- or

energy-transfer between adjacent organic/inorganic building blocks.

Most MOF and OMIM ligands tend to be conjugated and/or aromatic in nature, and therefore absorb UV-vis photons (hence may be referred to as chromophores) in $\pi^* \leftarrow \pi$ and $\pi^* \leftarrow n$ transitions [56]. The more highly conjugated a system is, the closer in energy its ground and excited states tend to be [57]. Increasing the conjugation therefore redshifts the absorption profile of a chromophore (see Figure 2.2a) and is a common strategy to obtain MOFs with extended visible-to-*Near-Infrared* (NIR) light absorption [58]. Complex ligands with a bridged electron donor and electron acceptor structure may maintain *Charge-Transfer* (CT) transitions in which the excited electrons migrate from the donor to the acceptor site of the molecule.

Metal-centred optical transitions generally arise from intraconfigurational (f-f or d-d) transitions that become weakly allowed by ligand-field splitting, or from CT transitions. Ligand-field splitting is the mechanism responsible for the colour of most transition metal complexes and MOFs. Transitions in lanthanide ion (Ln^{3+}) complexes, however, are a more particular case. The shielding of valence 4f electrons by the Ln^{3+} xenon core results in a greater radial expansion of the $5s^2 5p^6$ subshells, which gives the valence electrons an ‘inner’ character. The valence electrons therefore minimally interact with coordinated ligands, and as a result, their ligand-field splitting remains small. Non-centrosymmetric interactions that arise when the lanthanide ion is under the influence of a ligand-field allow the mixing of electronic states of opposite parity into the 4f wavefunctions. This relaxes the selection rules, so that intraconfigurational f-f transitions become partially allowed, resulting in sharp characteristic emissions. Mixing of the 4f and 5d orbitals in the presence of the ligand field gives rise to high-energy, parity-allowed, 4f-5d transitions. These appear as broad features in the absorption spectra of Ln^{3+} complexes. Since the 5d orbitals overlap with the ligand orbitals, the energy of these 4f-5d transitions is largely influenced by the immediate chemical environment surrounding the lanthanide ions [59].

Some of the common CT transitions arising in molecular materials like MOFs and OMIMs include *Ligand-to-Metal Charge Transfer* (LMCT), *Metal-to-Ligand Charge Transfer* (MLCT), *Ligand-to-Ligand Charge Transfer* (LLCT) and *Metal-to-Metal Charge Transfer* (MMCT). These transitions involve the migration of an excited electron between ligands and/or metal ion centres. Many d-metal MOF, for example, host transitions involving electron transfer from the ligands into the d orbitals of the metal nodes or vice versa (Figure 2.2b). LMCT tends to occur in MOFs whose metal ions are in high oxidation states, and are therefore easily reduced. Conversely, MLCT is seen in those

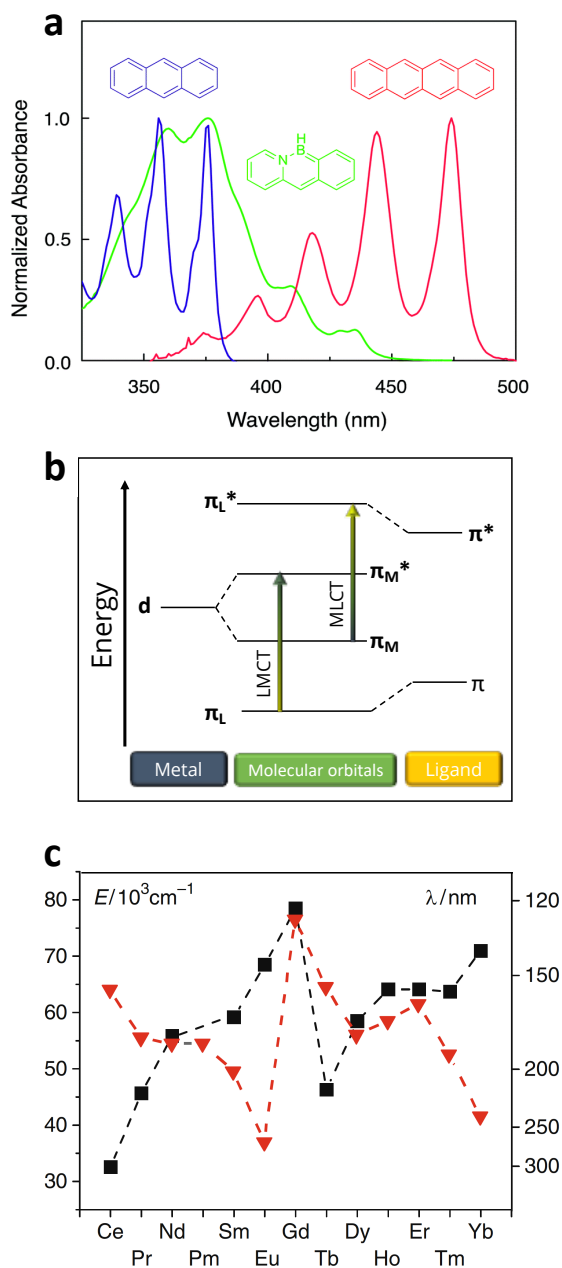


Figure 2.2 – Mechanisms of photon absorption in MOFs. **a.** Increasing the conjugation of aromatic molecules narrows the HOMO-LUMO gap, causing a red-shift in the $S_0 \rightarrow S_1$ transition energy. **b.** Ligand-field splitting gives rise to MLCT and LMCT transitions in MOFs as well as in metal complexes. These processes account for the colours of many transition-metal MOFs. **c.** Energy of the 4f–5d transitions in $\text{Ln}^{3+} : \text{CaF}_2$ (squares) and of the 2p (O)–4f LMCT transitions (triangles) demonstrate the high CT energy of most lanthanides. Reproduced with permission from [59].

MOFs whose metal centres are easily oxidised, and are coordinated to ligands with low-lying orbital vacancies [60]. Electrons involved in CT transitions moves through a considerable distance, which means that the resulting transition dipole moment tends to be large, however, there tends to be a small overlap between the ground- and excited-state wavefunctions in such transitions. For this reason, ligand-centred emission tends to be brighter than emission due to LMCT or MLCT [61,62]. Since the CT excitation of luminescent lanthanide ions is a key strategy for realising luminescent MOFs, it is important to note the CT transition energies in lanthanide complexes. As seen in Figure 2.2c, these transition energies are quite high, with the lowest-energy characteristic LMCT transitions observed in Eu^{3+} , Yb^{3+} , Sm^{3+} , and Tm^{3+} .

2.1.4 Dark excited-state processes

Before undergoing radiative decay, photo-excited electrons in a molecule may undergo a number of non-radiative relaxation and energy transfer processes. In this section we briefly summarise the key non-radiative, or dark, excited-state transitions that occur in molecular systems like MOFs and OMIMs. These processes, including vibrational relaxation, internal conversion, intersystem crossing, and energy transfer, are also highlighted in the Jablonski diagram in Figure 2.1.

Vibrational relaxation occurs within picoseconds of the optical excitation, with the excited electron thermally transitioning down the ladder of close-lying vibrational energy levels to reach S_1 , from where radiative decay generally occurs. When excited to a higher-lying energy (S_n), another radiationless de-excitation process may arise from the lowest vibrational level of S_n to a vibrational level of S_{n-1} . This process, known as *Internal Conversion* (IC), may precede vibrational relaxation, radiative decay, or non-radiative decay due to quenching processes.

The energetic position of the lowest triplet excited state, T_1 , in a molecule, plays a decisive role in the probability of having the third type of dark relaxation process, *Inter-System Crossing* (ISC), arise. Due to combined effects of spin-correlation and Coulomb repulsion, the spin-opposed T_1 level lies lower in energy than the spin-paired S_1 level [63]. In molecules and complexes that contain heavy atoms (e.g. S, I, transition metals, and lanthanides), and in which the T_1 state lies sufficiently close in energy to S_1 , coupling of electronic spin and angular momenta can lead to an overlap of the T_1 and S_1 orbitals. This gives rise to a nonzero probability for the electron to undergo a $S_1 \rightarrow T_1$ transition,

known as ISC, whereby its spin flips and it occupies the T_1 excited state. ISC is assisted by spin-orbit coupling, vibrational coupling, and the presence of paramagnetic ions [64], which is why it can be observed in many MOFs based on Ln^{3+} or period 6 metals.

In molecules with a donor-acceptor type structure, *Energy Transfer* (ET) processes occur in which the excited state is transferred from the donor to the acceptor. There are two mechanisms by which such donor-acceptor energy transfer can take place; *Förster Resonance Energy Transfer* (FRET), and *Dexter Electron Exchange* (DEE). FRET relies on Coulombic interactions between chromophores separated by around 1–10 nm. In this process, dipole–dipole coupling between the excited state of the donor and ground state of the acceptor allows for an excited state to be transferred from the donor to the acceptor without electron exchange [65]. This can occur if transitions of equal energy are possible in both species, and it requires a spectral overlap between the emission spectrum of the donor species and the absorption spectrum of the acceptor species, as illustrated in Figure 2.3a. DEE on the other hand, is a short-range process, typically occurring in a range of 10 Å, that relies on orbital overlap between a donor and acceptor chromophores. This overlap allows the excited electron and corresponding hole from the donor species to be injected to the acceptor, as shown in Figure 2.3b, in either a simultaneous or two-step process [65]. An important consequence of energy transfer is the so-called ‘antenna effect’, portrayed in Figure 2.3c, whereby a chromophore with efficient light-harvesting properties transfers its excitation energy to a neighbouring species that absorbs poorly. Exploiting the antenna effect is a common strategy used to populate the radiative excited states of luminescent Ln^{3+} ions, which are themselves poor absorbers. It is worth noting that ET processes are strongly influenced by the orientation and spacing of adjacent chromophores. Coulombic interactions tend to dominate many self-assembled structures like MOFs, which is why FRET is the predominantly observed energy transfer mechanism [66]. Having said that, the periodic arrangement of chromophores in MOF structures in general provides a great deal of opportunity to investigate, model, and interpret the many possible energy transfer pathways associated with these complex processes.

2.1.5 Emission processes

While the various non-radiative decay processes described above are common, if the $S_1 \rightarrow S_0$ or $T_1 \rightarrow S_0$ transition energy is too high to be dissipated by thermal interactions with the surrounding medium, the electron may then return to S_0 by emitting a photon.

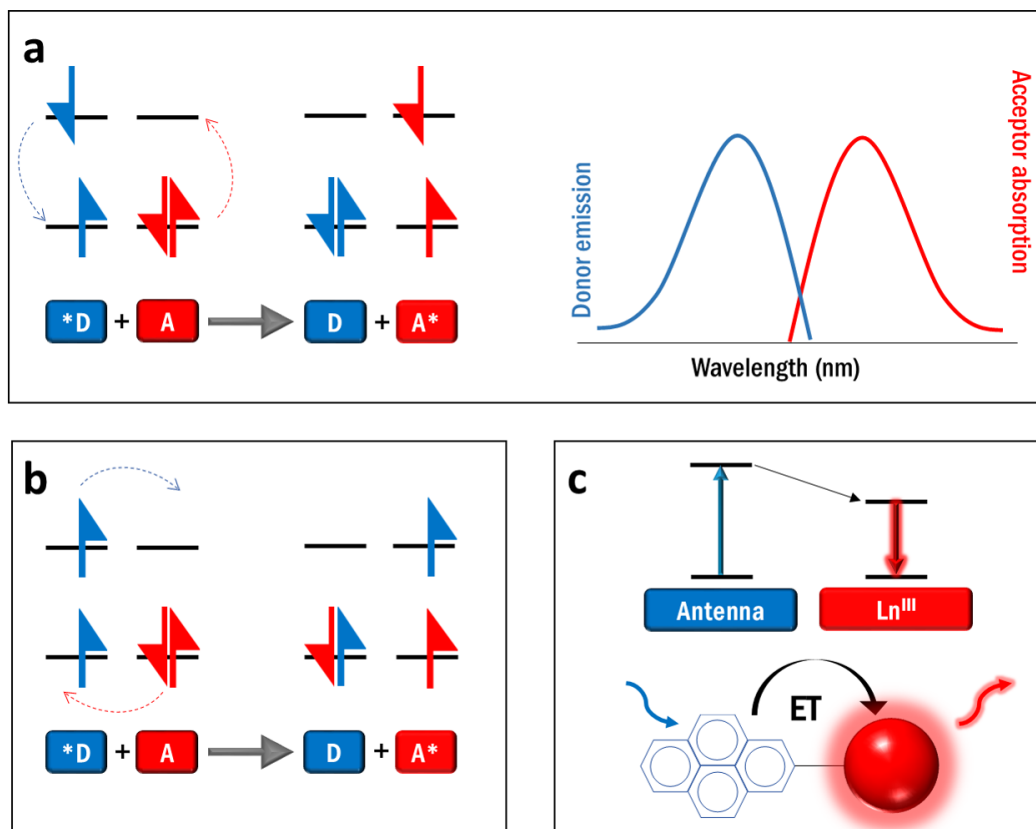


Figure 2.3 – Energy transfer processes. **a.** Long-range, Förster resonance energy transfer process, **b.** Short-range Dexter electron exchange process, **c.** Portrayal of the antenna effect for sensitizing luminescent lanthanide ions.

Since this thesis deals with luminescent materials, it is these spontaneous radiative decay processes that are of interest to us. Radiative decay can take the form of either fluorescence ($S_1 \rightarrow S_0$) or phosphorescence ($T_1 \rightarrow S_0$). Fluorescent and phosphorescent processes can be differentiated based on their typical photoluminescence lifetimes; fluorescence is characteristically fast with a lifetime of the order between ns to ms, while phosphorescent emissions last significantly longer, with lifetimes often approaching the scale of several minutes [23]. Since the S_1 energy level is, by definition, spin-paired with S_0 , $S_1 \rightarrow S_0$ radiative decay is favourable and fast. Systems that have undergone ISC, however, decay from T_1 , which is spin-opposed with respect to S_0 . $T_1 \rightarrow S_0$ decay is therefore spin forbidden, and as a result, the excess energy slowly leaks out in the form of a weak emission (phosphorescence) that continues over a long duration of time. Because of the various dark relaxation processes that precede fluorescence and phosphorescence, the

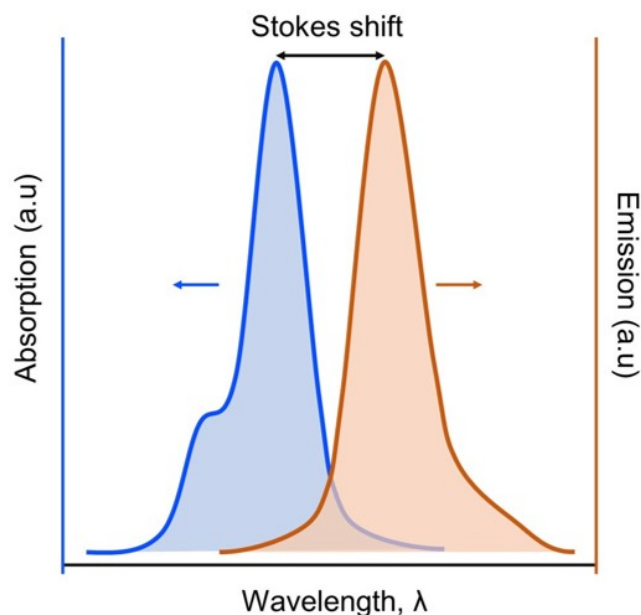


Figure 2.4 – The Stokes shift is the difference between positions of absorption and emission band maxima corresponding to the same electronic transition.

energy of the emitted photons is almost always redshifted with respect to the excitation energy (special cases of upconversion luminescence are not addressed in this thesis, but the interested reader can refer to [23, 67, 68]). This shift, named after Irish physicist George Stokes, is measured as the difference between the peak excitation and the peak emission wavelengths of the same electronic transition. The Stokes shift, illustrated in Figure 2.4, is larger in cases where the excitation of molecules results in the lengthening of chemical bonds. For complexes analysed in solution or suspension form as many MOFs and OMIMs are, the magnitude of the Stokes shifts is influenced by the polarity of the solvent, with polar solvents usually giving rise to more significant Stokes shifts [23]. There are two practical advantages to having a large Stokes shift in a luminescent molecule or complex. First, it allows easy separation of the luminescence signal from the excitation light source with the help of optical filters, enabling fluorescence detection to be measured with a very low noise background. Secondly, a large Stokes shift implies low overlap between excitation and emission wavelengths, which mitigates problems associated with re-absorption of emitted light that can lower the efficiency of luminescent materials.

In the following section, we take a look at how the various photophysical processes that we have discussed may manifest in MOF and OMIM structures. It should be noted that due to the relative infancy of OMIMs as a class of materials, there are few reports of

luminescent crystalline OMIMs. Therefore, although the principles discussed in this Chapter are equally relevant to MOFs and OMIMs, the following section focuses more on luminescence MOFs due to their relatively mature stage of development.

2.1.6 Luminescence in MOFs and OMIMs

While OMIMs may be constructed solely from organic chromophores, the optical properties of luminescent MOFs may arise from either one of their structural components, i.e. from their organic linkers or from their metallic nodes. In some cases, chromophoric or luminescent guest molecules may also be incorporated into the pores of these materials to enhance or tune their optical properties. For example, small-molecule dyes introduced into MOF pores give rise to extended absorption spectra in which the characteristic absorption peaks of both the MOF and the guest [69] are present. Similarly, fluorescent dye molecules or *Quantum Dots* (QD)s can be introduced as guest molecules to offer new luminescence properties [70] to the host structure. Figure 2.5 uses the depiction of a MOF to highlight the range of interactions involving light that can occur on such structures. The most common way of making luminescent MOFs is to use luminescent organic ligands with extended π -conjugation as linker components. In this way, the MOF scaffold has added functionality, and appropriate linkers can be chosen depending on the desired luminescence properties. MOFs with luminescent linkers may exhibit purely linker-centred emission, where both the photon absorption and emission are localised on the same organic ligand, or more complex emission involving absorption and emission that occur in separate parts of the framework. The latter type of emission is facilitated by non-radiative ET and CT processes such as FRET and DEE. As illustrated in Figure 2.5, transitions may occur between adjacent ligands, ligands and metal centres, or guest molecules and either of the building blocks.

It is important to note how immobilising luminescent ligands into ordered, regular positions as MOF linkers influences their optical properties. One important advantage is the enhancement of luminescence quantum yield that comes with locking chromophores into fixed, rigid positions and thus reducing vibrational and rotational losses [71]. The stacking and relative orientation of the linkers in MOF structures can affect the positions and profiles of their spectral peaks. For example, immobilizing chromophores as MOF linkers can result in intermolecular interactions that change the Stokes shift of a transition, as well as the *Full Width at Half Maximum* (FWHM) of its associated peaks, compared to the free chromophore [72]. Intermolecular stacking between adjacent linkers

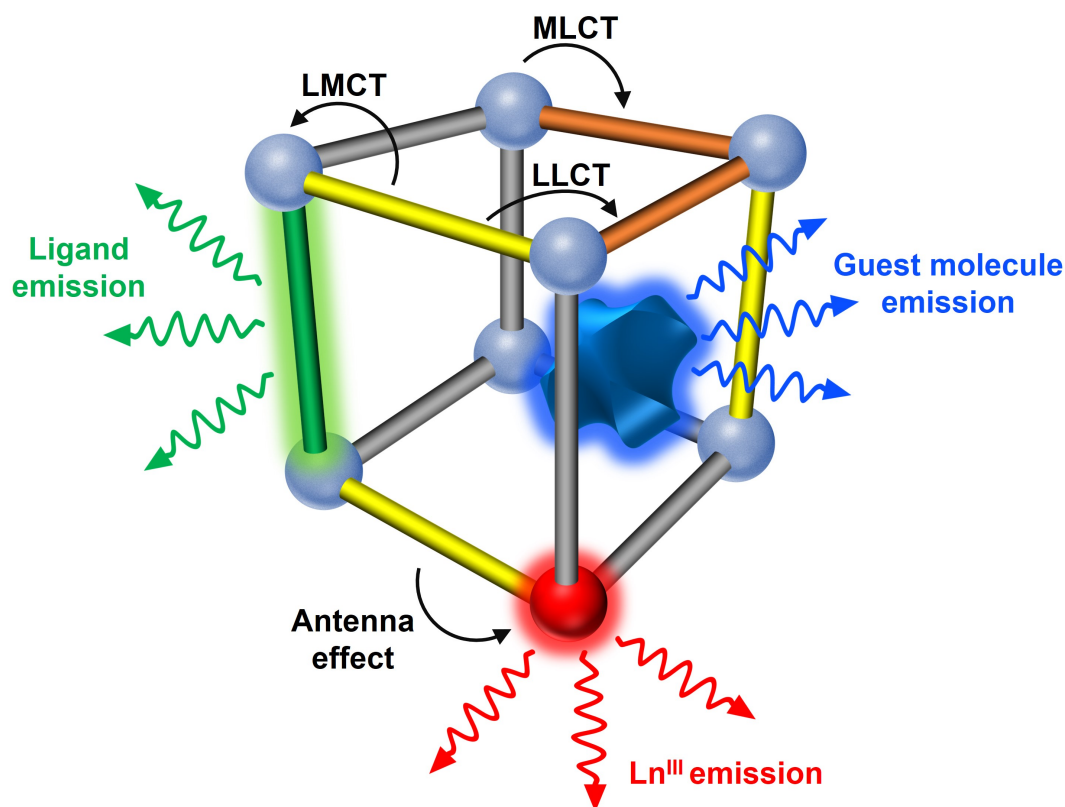


Figure 2.5 – The photophysical mechanisms arising in MOFs involve light absorption, charge- and energy-transfer processes, and ligand, metal, or guest-based luminescence. The chemical and structural versatility of such materials provides a wide range of opportunities to explore.

can also give rise to new absorption or emission features based on to LLCT transitions. In contrast to free chromophores or those in molecular complexes, where close chromophore packing results in significant electronic coupling, MOFs provide a pathway towards otherwise-inaccessible photophysical processes by separating and precisely organising the chromophores within their structures.

Luminescence involving the metal nodes of MOFs is a less common strategy, but one that also has unique advantages. Typically, transition metals do not significantly contribute to the luminescence properties of MOFs, other than affecting the ligand-based luminescence by the introduction of charge-transfer states. Luminescent lanthanides like Eu^{3+} , Tb^{3+} , Dy^{3+} , etc. on the other hand, tend to dominate the emission when incorporated into MOF structures. Since Ln^{3+} ions have small absorption coefficients, the excited-state levels in luminescent lanthanide MOFs are commonly populated by energy transfer from a sensitizing ligand via the antenna effect [73]. In the sensitization of Ln^{3+} ions, a photon

is captured by the MOF organic linkers, then the energy is transferred to the metal ion, which results in Ln^{3+} emission. As a result of the poor expansion of the 4f orbitals, the Ln^{3+} -ligand bonds show minimal mixing of the metal and ligand orbitals with a covalency of less than 10%. Because of this, photoexcited f-f transitions in lanthanides tend not to perturb the binding pattern of lanthanide complexes [59]. The excited states in the organic linkers and metallic nodes of Ln^{3+} MOFs can therefore be treated separately, and their resulting Ln^{3+} -emissions remain characteristically sharp.

The considerations briefly summarised in this Section make it possible to attribute the absorption and emission spectral features of MOFs and OMIMs to the appropriate corresponding processes. This is particularly true in simple structures exhibiting purely-ligand or Ln^{3+} -based optical features. However, since many MOF structures are exquisitely complex, it is common to have multiple simultaneous processes taking place, and the relative contributions of various concurrent processes can be much more challenging to deconstruct. In such cases, the inherent crystallinity of MOFs offers a great advantage. Given the regular orientation of chromophores in luminescent MOF structures, the atomic positions, relative distances, bond lengths, and angles of adjacent building blocks can be precisely determined by X-ray diffraction. This greatly favours the use of computational tools to model, predict, and gain deeper insights into the various interactions at play. In the following section, we review the key parameters needed to experimentally characterise the optical properties of a luminescent MOF or OMIM.

2.2 Characterisation of light emission

There are several key metrics by which to characterize the optical properties of luminescent MOFs and OMIMs. These include its UV-vis absorption, its photoluminescence and excitation spectra, its photoluminescence quantum yield (the number of photons emitted per photon absorbed), and its luminescence lifetime (how long the material remains in its excited state before radiative decay).

2.2.1 Steady-state absorption spectra

UV-vis absorption spectra are generally measured as the attenuation of a light covering a range of wavelengths as it passes through a sample surface. Due to the solid powder form in which most MOFs occur, they possess inherent surface inhomogeneities that cause

significant light scattering. UV-vis absorption spectra of MOFs are therefore typically calculated from their diffuse reflectance spectra. The diffuse reflectance of light (R) from a sample is first measured from a carefully-ground sample that is tightly packed into a cell of parallel quartz windows.

This spectrum is then treated by the Kubelka-Munk function [74], $F(R)$, given by Equation 2.2.

$$F(R) = \frac{(1 - R)^2}{2R} \quad (2.2)$$

Where $F(R)$ describes the absorption coefficient of the sample, k , over a scattering coefficient, s . By condensing the geometric irregularities of inhomogeneous samples into a single scattering coefficient in this way, $F(R)$ effectively describes the propagation of light through them.

The UV-vis absorption and diffuse reflectance measurements presented in this thesis were carried out on a Perkin Elmer UV-vis spectrometer fitted with an integrating sphere and a spectral range of 200 nm - 1000 nm, and a resolution of 1 nm. A barium sulfate standard was used to calibrate 100% reflectance.

2.2.2 Photoluminescence quantum yield

Photoluminescence Quantum Yield (PLQY) is the ratio of the number of emitted photons to the number of absorbed photons, and provides measure of a material's efficiency in converting absorbed photon energy into light. For this reason, PLQY has been a key criterion for the selection of luminescent materials in many applications. Measurements of absolute quantum yields were carried out using a Horiba Fluorolog-3 equipped with an integrating sphere. As best practice, reported quantum yield values are an average of five independent measurements.

2.2.3 Steady-state emission spectra

Emission spectra were measured using a PerkinElmer LS55 spectrophotometer. Measurements of MOF emission spectra in suspension were carried out in a quartz cuvette with four optically clear windows, while solid-state measurements were carried out by packing carefully ground MOF powders into a cell of anodized aluminium with one optically

transparent quartz window. Excitation spectra of the key steady-state photoluminescence peaks were measured on the same instrument in order to determine the optimum excitation wavelengths.

2.2.4 Transient photoluminescence

Time-resolved luminescence was recorded with an Edinburgh Instruments LP980-KS flash photolysis setup. A 355 nm nanosecond pulsed laser (5ns pulse duration, 10Hz, Ekspla NT342 model) with an integrated *Optical Parametric Oscillator* (OPO) system (from 355 to 2500 nm tunability) has been used as pump source. Wavelength-specific kinetic measurements were made using photomultiplier and digital storage oscilloscope.

2.3 Conclusions

In this Chapter, we laid out some of the key concepts and processes that play a relevant role in describing the photophysics of MOFs and OMIMs. We explained that MOFs and OMIMs are molecular systems in which localised optical transitions take place. We briefly addressed the physical principles governing the probability of optical transitions to occur, and the types of molecular systems in which forbidden transitions may be expected to arise. With these basics established, we followed the possible paths that a photoexcited molecular system may encounter on its way to radiative de-excitation. These pathways were addressed in the order of their occurrence, i.e. photoexcitation, possible excited-state transitions, and finally emission. We summarised how the various photophysical processes discussed may manifest in MOF and OMIM structures. Finally, we reviewed the methods and techniques that were used in this thesis to characterise optical properties and identify photophysical processes.

In the following Chapter, we report our first example of how the photophysical processes described here can be applied to the design and synthesis of a MOF with desirable properties. Using the principles of a lanthanide excitation via the antenna effect, we designed a luminescent MOF for the detection of trace contaminants in drinking water samples.

3

A Luminescent MOF for Sampling Water Quality

In the previous chapters, we reviewed the basic principles underlying the design and synthesis of *Metal-Organic Frameworks* (MOFs) and *Organic Molecules of Intrinsic Microporosity* (OMIMs), with a focus on luminescent structures. We then described some general mechanisms of luminescence originating from organic luminophores and from lanthanide ions, as well as methods by which luminescent MOFs and OMIMs may be realised and characterised.

In the following chapters, we turn to applications of luminescent MOFs and OMIMs, and provide two detailed examples which have been developed in the scope of this thesis. We start in this Chapter with chemical sensing applications. We review some important basics about chemical sensors, and then describe in detail how we exploited lanthanide ion luminescence to realise a new MOF for the selective, quantitative sensing of trace amounts of fluoride ion contaminations in drinking water sources. Both the organic and inorganic components of our MOF play key roles in its operation as a sensor. The organic ligand interacts with the target analyte, and the luminescent lanthanide metal centres act as optical transducers with a luminescence quenching response to the presence of fluoride ions. We conclude the Chapter with a brief overview of how the principles we used in this application can be extended for the detection of other chemical contaminants. The contents of Section 3.3 are largely based on the report of a luminescent Eu^{3+} -MOF sensor by Ebrahim¹ et. al, published under the title "Selective, Fast-Response, and Regenerable Metal-Organic Framework for Sampling Excess Fluoride Levels in Drinking Water", in the *Journal of the American Chemical Society* in February 2019. The contents of this section have been reproduced with permission from the publisher.

¹The contribution of F. M. Ebrahim was to determine the application, establish characterisation protocols, carry out optical and sensor characterisation experiments, optimise the sensing method, co-design and fabricate the device, and write the manuscript with contributions from all coauthors.

3.1 A Brief Overview of Chemical Sensors

Chemical sensing is a burgeoning application of MOFs that exploits their porosity, crystallinity and modularity to create novel, tailor-made structures for the detection of targeted analytes. The number of possibilities to exploit host-guest chemistry in the design of MOF-based sensors is matched by the infinite number of ligand and metal combinations that can be used in MOF synthesis. Even without turning to the design and synthesis of novel structures, well-established methods of *Post-Synthetic Modification* (PSM), including the introduction of defects to expose metal sites and post-synthetic ligand functionalisation to introduce new chemical functionalities, offer a range of possibilities in the synthesis of MOFs for chemical sensing.

Chemical sensors are important devices in areas spanning medical diagnostics, food and water quality control, environmental monitoring, and chemical threat detection. Regardless of the application, there are two key components that typically make up a chemical sensor. An active site, containing a recognition molecule (*i.e.* a receptor), recognises and interacts with the target analyte, and a transduction element that converts this interaction into a quantitative reading (Figure 3.1). A sensing event occurs when target analytes either chemically bind or physically adsorb onto the active site. This induces changes in certain physical properties of the sensor such as its rigidity or density, its electrical conductivity or capacitance, or its *Ultra-Violet* (UV)-visible absorption or fluorescence spectra. Depending on the type of physical change induced, an appropriate transduction element is selected to convert the sensing event into a conveniently readable (typically electrical) signal. Some common examples of the transducers used in MOF-based mechanical, electrochemical, and optical sensor devices, include microcantilevers or *Quartz-Crystal Microbalances* (QCMs), electrochemical cells, and photoresistors or photodiodes, respectively. Dynamic microcantilevers are oscillating cantilevers that resonate at frequencies determined by their dimensions and material properties [75]. An analyte binding event on the surface of a microcantilever will be detected as a shift in the cantilever's resonant frequency. In static microcantilevers on the other hand, analyte sorption is determined by the bending of the cantilever, and measured by a strain gauge [76]. QCMs are a type of acoustic wave sensor consisting of an AT-cut quartz substrate patterned with circular electrodes on either side. The application of an alternating voltage across the piezoelectric quartz crystal generates an oscillating shear deformation, the frequency of which changes upon guest adsorption [77]. Although the specific operating principles of different mechanical transducers are varied, the sensing

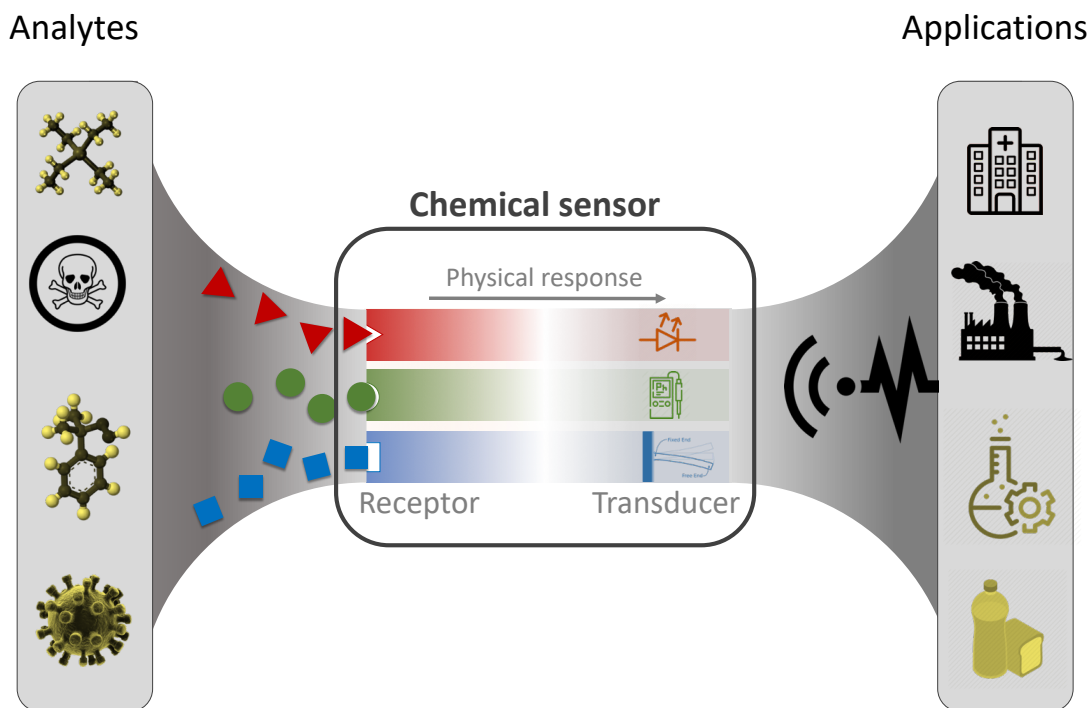


Figure 3.1 – Overview of chemical sensors. A standard sensor device consists of an active site, or receptor, that can bind to or interact with any one of a range of analytes. The binding triggers a change in the physical properties of the active site, and the measurement of this change makes it possible to quantify the concentration of the analyte present.

response in all such devices can equally be enhanced by coating the active mechanical component with an appropriate MOF. Several examples of mechanical sensors can be found in MOF literature; just two of which include sensing of alcohol vapours by ZIF-8 [78], and CO_2 by MIL-53(Al) [79], deposited on silicon microcantilevers. Figure 3.2 illustrates how MOFs can be coated onto micromechanical transducers.

The most commonly used electrochemical cells are based on a potentiometric operating principle, whereby an ion-specific electrode is placed in contact with a sample, and the concentration of a specific analyte is determined from changes in potential difference between a working electrode and a reference electrode [81]. The incorporation of MOFs into ion-specific electrodes can be achieved by fairly routine fabrication methods, and several examples can be found in the literature. Davydovskaya et. al demonstrated potentiometric sensing by drop-casting HKUST-1 onto TiN electrodes, resulting in potential difference responses upon exposure to trace concentrations of various aldehydes [82]. HKUST-1@graphene composites have been used for conductometric ammonia

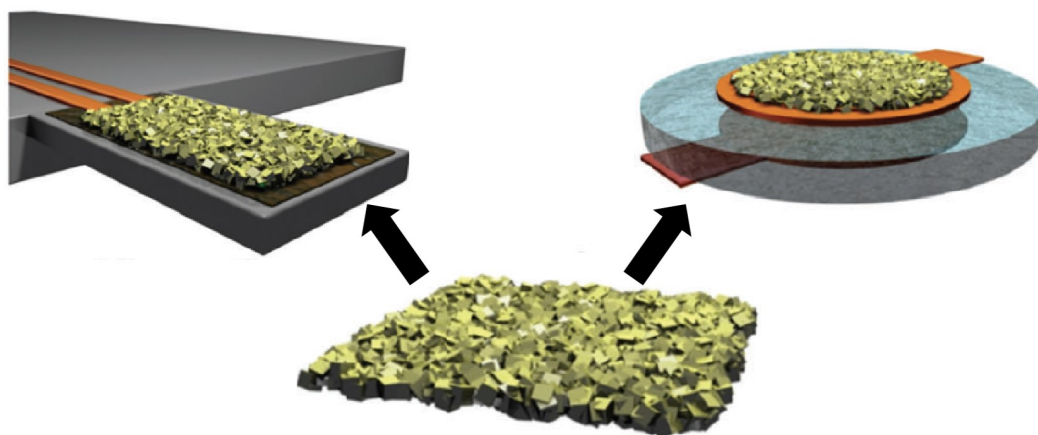


Figure 3.2 – Incorporating MOFs into micromechanical sensors. Films of packed MOF crystals or crystalline powders may be deposited onto micromechanical cantilevers (left) or QCMs (right) for sensing applications [80].

detection in devices fabricated by slurry blade-casting onto interdigitated electrode substrates [83]. This MOF-derived device exhibited reversible ammonia binding with a linear transduction response between 100 - 500 ppm at room temperature.

Simple photoresistors and photodiodes can be used as transducers when sensing events lead to a change in the luminescence intensity of the receptor at a given wavelength. Optical sensors that undergo changes in the position of absorption or emission peak positions on the other hand, require slightly more complex optical transducers, capable of measuring spectral changes. The richness of molecular photochemistry makes chromophores and luminophores in general excellent candidates for a wide range of sensing applications. This photochemistry is easily extended to MOF structures, as evidenced by abundant examples in the literature of MOFs that may potentially be used as optical sensors. There are several key parameters which are used as performance indicators of a chemical sensor [84]. These include:

- Selectivity, the ability of the sensor to accurately measure the concentration of the analyte in the presence of interfering molecules.
- Sensitivity, which refers to the minimum input that will create a detectable output change, and can more precisely be defined as the ratio between the output signal

and the measured analyte concentration.

- Linearity, the extent to which the actual measured curve of a sensor departs from the ideal curve.
- Range of operation, the maximum and minimum values of analyte concentration that can be measured.
- Response time, the time required for the sensor response to rise from 0 to a final settled value within a tolerance band of the correct new value.
- Precision, which refers to the degree of reproducibility of a measurement. An ideal sensor would output exactly the same value every time that a specific measurement is repeated.

In order to make a MOF chemical sensor viable for implementation into a practical device, it is crucial to keep these factors in mind. The process of developing a MOF-based sensor naturally starts with the target analyte. Once the analyte is chosen, a MOF with an appropriate receptor localised on the ligand or in the form of open metal sites, can be identified or designed to interact with the target molecule. Knowing that MOF sensors can be paired with different transduction mechanisms described in this Section to make a device, one must select an appropriate transduction mechanism for the chosen MOF to get the most selective, sensitive, precise, and rapid output. With the appropriate choice of transduction mechanism, the system can finally be tested for the desired application, characterised, and integrated into a device. These steps are nicely summarised in Figure 3.3. In the following section, we discuss why implementation of MOFs into devices can be challenging, and why optical transduction holds the most promise for practical implementation.

3.2 Integrating MOFs into sensor devices

In Section 3.1 we summarise the types of device formats into which MOF sensors can be integrated, and highlight the key characteristics of a good chemical sensor. We now address some of the practicalities of pursuing MOF-based sensors. A key challenge is that the widely-used synthetic methods involving solution-phase self-assembly of MOFs afford limited control over the homogeneity of crystal shapes and sizes [86]. This means that MOF films, formed by drop-casting or spin-coating a MOF suspension onto a

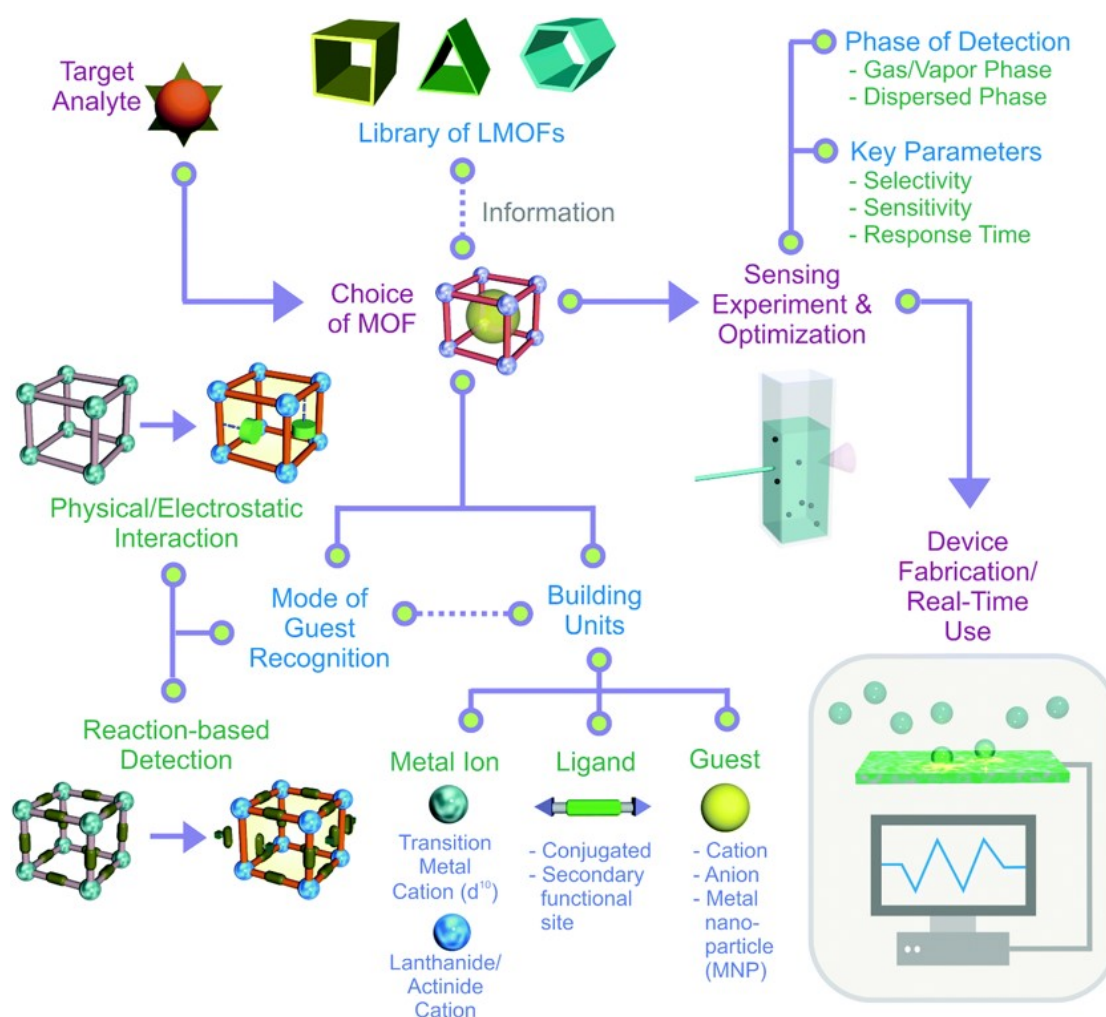


Figure 3.3 – The process of developing a MOF sensor. An illustrative flowchart describing the process of developing a MOF sensor. Reproduced from [85].

device substrate, contain a high density of non-uniform crystallites and grain boundaries, making calibration and reproducibility challenging issues for MOF-based electrochemical and mechanical sensor devices [86]. The crystalline powder form in which most MOFs occur does, however, make them well-suited to sensing applications based on optical phenomena such as fluorescence and colour-change. This is because crystals are typically carefully ground into evenly-sized crystalline particles, making both suspension- and dry powder-based optical characterisation more reliable. With particles of a relatively narrow size distribution either tightly packed together or homogeneously suspended in an appropriate solvent, possible error from scattering is minimised, and reliable spectral data can be recorded. This sample preparation strategy does not apply for electrical measurements as it only serves to increase the number of grain boundaries and interfaces.

As-synthesized luminescent or chromophoric MOFs may be therefore used for sensing in air, gas, or solvent suspensions, without the need for film formation or other additional processing [19].

Optical sensors range in complexity from simple chromic tools like litmus paper and pregnancy tests, to chemically complex molecular cages that release luminescent guest molecules upon interaction with an analyte. Chromic MOF sensors, which undergo a change in their UV-vis absorption spectra, can be implemented into test papers where the change in colour is easily detected by eye [87]. Common chromophoric ligands such as porphyrins and pyrenes, which possess aromatic or conjugated segments, can be used as the linkers to make chromic MOF sensors. Alternatively, ions of d-metals such as Cu, Fe, and Co, among others, can be chosen as the as node metals to lend chromophoric properties to MOF structures. An interesting example of a chromic MOF sensor, used for NH_3 sensing, is seen in the ship-in-a-bottle structure of SION-10, reported by Gladysiak et al [88]. The active site in SION-10 occurs in the form of mononuclear Cu^{2+} complexes that decorate the pores. Selective binding of NH_3 vapours results in an immediate green-to-blue color change in the MOF upon exposure. While this is arguably the simplest and most inexpensive way to convert a chemical sensing event into a signal, the sensitivity of chromic sensors tends to be quite low, and quantifying the concentration of an analyte with this method is difficult, at best. More accurate quantitative results might be obtained from soluble chromic sensors used in conjunction with a spectrometer, however this approach is extraneous to MOFs due to their insolubility.

3.2.1 Design of Luminescent MOF sensors

Chromic chemical sensors are based on a change in the colour of the sensing material when it interacts with an analyte. Luminescent sensors on the other hand emit light when they are photoexcited, and a sensing event causes a change in their luminescence colour or intensity. Chromic sensor responses from insoluble crystalline powders can be difficult to quantify. This is because the absorption spectra of solid powders are obtained from measurements of their diffuse reflectance. While peak shifts are easy to identify using this method, changes in intensity cannot be reliably measured due to the effects of light scattering. The results that can be obtained from chromic MOF chemical sensors are therefore binary in nature, and can indicate the presence of the analyte, but not its concentration. It is much easier to obtain reliable quantitative measurements from MOF sensors based on luminescence [19]. This is particularly true for MOFs that exhibit tuning

of luminescence intensity in response to a chemical sensing event. The most common form of signal transduction in luminescent MOFs is quenching, (less common is enhancement), of photoemission due to guest adsorption [23]. In molecules containing aromatic subunits (as many MOF ligands do) for example, UV excitation tends to populate the *Lowest Unoccupied Molecular Orbital* (LUMO), leaving a strongly oxidizing hole in the *Highest Occupied Molecular Orbital* (HOMO). Adsorption of an analyte that is either easily oxidized or reduced on such a ligand can inhibit the radiative process and thus attenuate photoluminescent signals. Commonly exploited interactions in MOF-based sensing are those in which there is significant electron-donor/electron-acceptor orbital overlap, where the MOF or analyte may play either role. As a consequence, the most easily-detected analytes are those that are strong electron donors (e.g., amines) or acceptors (e.g., nitroaromatics, including common explosives). Rather than being oxidised or reduced by interaction with the MOF, a target analyte may otherwise alter the redox potential of a built-in donor or acceptor, and thus impact the luminescence. Factors contributing to luminescence quenching/enhancement may also include steric effects, whereby interacting analytes alter vibration or torsional displacement, shifts in absorption spectra, or changes in the electronic structure of the luminescent MOF [89].

Typically, the change in luminescence intensity is directly proportional to the concentration of analyte present at the active site of the MOF sensor. Since the error in luminescence intensity introduced by light scattering and reflection is minimal, luminescence-based chemical sensors are easy to calibrate and have been shown to give precise quantitative measurements. Even in luminescent MOFs whose spectral response involves a large peak shift, the photoluminescence excitation wavelength in most cases remains constant, greatly simplifying the process of calibrating them as quantitative chemical sensors.

In order to drive luminescent MOF sensors an additional step closer to real-world application, some practical considerations need to be made, including:

1. the environment in which the sensing must be carried out,
2. the expected interferences or possible false positive triggers, and
3. the concentration range of interest.

The typical environment of a target analyte determines how important factors like MOF stability, hydrophobicity, and potential for film growth are. The expected interferences

will determine whether relying on mechanisms like physisorption or mechanical sieving will be sufficient, or if chemical functionalities need to be introduced to the pores to improve selectivity. Finally, the concentration range of interest is an important factor to consider at the device design and engineering stage.

Interaction with target analytes may occur in the form of physisorption, electrostatic interactions, π - π stacking, bond formation or bond cleavage [90]. Electrostatic and chemical interaction sites can be introduced into MOF structures either via ligand functionalization or the exposure of open metal sites, while π - π stacking interactions will arise in MOFs with conjugated ligands. In many cases, the interaction mechanism can be selected based on the nature of the target molecule. For example, aromatic compounds may be targeted by stacking, and ionic compounds by electrostatic or Lewis acid-base interactions.

Since mechanisms like physisorption and π - π stacking tend to be non-specific, it is important to introduce features into the MOF structure that make it selective to the target molecule. The existing literature on gas separation by MOFs offers considerable insight into what types of structures and functionalities may be useful for specific analytes. The simplest approach is via size exclusion (i.e. molecular sieving); whereby the pore structure is chosen or tailored according to the kinetic diameter of the target molecule and potential interferences present in the sample [91]. Molecular sieving exploits the fact that molecules that are smaller than the MOF apertures can be absorbed, but larger molecules cannot. We described in Chapter 1 how pore sizes may be determined by the topology of a MOF, as well as the *Secondary Building Unit* (SBU)s, organic ligands and the presence of functional groups added to the linkers. It is worth recalling that while larger linkers might be expected to result in larger pores and/or apertures, MOFs with long linkers tend to interpenetrate, resulting in smaller pores. To avoid this, it is recommended to use chelating metal clusters as nodes, bulky linkers with some steric hindrances, and/or to assemble MOFs in dilute conditions. PSM can be used to tune pore dimensions by solvent removal, or by replacing coordinated solvent molecules with functional ligands. Many examples exist where ligands functionalized with -NH₂, -SH, and -OH groups have been used to construct MOFs for sensing [19]. These functional groups offer analyte recognition opportunities for a wide range of chemical species. For this reason, PSM strategies have become an important way of introducing functionality to MOF the accessible volume of MOF pores. Exposure of open metal sites can be achieved by introducing missing linker defects. The method for defect growth varies from MOF

to MOF, with the most well investigated example being that of UiO-66, in which the addition of small amounts of formic acid or acetic acid during synthesis lower the kinetic growth rate, giving rise to a higher density of open metal sites. Post-synthetically, the removal of coordinated solvent molecules from the metal ions or clusters by activation can also yield exposed Lewis acid metal sites. These can be used for reversible bonding interactions, such as NO binding to Co^{2+} , Cu^{2+} , or Ni^{2+} ; or, they can be engage in purely electrostatic interactions, such as quadrupole/charge interactions between CO_2 molecules and cobalt or aluminium ions.

Since spectroscopic characterisation methods require optical instrumentation that can be challenging to miniaturise into practical sensor device formats, the bulk of MOF literature reporting new structures for optical sensing demonstrate laboratory-level characterisation results. In this thesis, we aim to address the gap in MOF-sensor device integration, by focusing on the development of a novel luminescent MOF with a quantifiable turn-off response.

3.3 A Luminescent Ln-MOF for sensing trace contaminants in drinking water

Fluoride (F^-) is commonly associated with the prevention of dental cavities, as low concentrations promote the formation of enamel-strengthening fluorapatite on dental surfaces [92]. Less recognized are the potentially severe detrimental effects that over-consumption of F^- can cause. Prolonged consumption of water contaminated with F^- at concentrations exceeding 1.5 ppm can lead to considerable health implications, particularly in children and developing embryos. Over time, an intake of beyond 0.05 mg per kg of body weight per day leads to excess mineralization within tissue and organs, resulting in mottled enamel, [93] hindered functioning of the kidneys, [94] thyroid, [95] [96] and brain, [95, 97] and crippling bone deformities most commonly manifested in the legs and spine [98, 98]. Such forms of chronic F^- toxicity are endemic in over 25 countries, with contamination typically leaching into drinking and irrigation water supplies through rocks rich in F^- minerals, or waste from such industrial processes as aluminium smelting and glass processing. [99] Research into new solutions for detecting F^- contamination aims to surpass existing commercial devices in their accessibility to non-expert users who require regular, laboratory-free sampling, such as remote populations in areas where chronic F^- toxicity is endemic.

The majority of recently reported methods for F^- sensing include molecular complexes exhibiting turn-on [100], turn-off, or ratiometric color changes [101] arising from Si-O bond cleavage, H-F bond formation, or Lewis acid-base interactions in the presence of F^- [102]. In addition to molecular F^- sensors, a few reports have been published on ion sensors based on MOFs. The reported MOF-based solutions include a turn-on optical sensor in which signal transduction relies on the decomposition of the MOF to release a fluorescent reporter molecule [103] and a turn-off optical sensor that uses a combination of ligand-based and lanthanide-based luminescence to achieve highly sensitive ratiometric fluorescence quenching signals when F^- covalently binds to the ligand functional group [104]. These notable examples demonstrate the promising potential of MOFs in water-sampling applications. To further advance the performance of chemical sensors in general and F^- sensors in particular, it is pertinent to focus on the architecture of the active site where interactions with the analyte occur. Sensors relying on covalent bond cleavage are mainly non-recyclable, while those based on covalent bond formation may be difficult to regenerate without additional treatment under harsh conditions (e.g., with a strong acid or base, which is particularly detrimental to many MOF sensors). Electrostatic interactions, on the other hand, though easy to reverse, are non-specific, resulting in poor selectivity [105,106].

We describe a water-stable, recyclable, luminescent lanthanide MOF, referred to as Sion-105, which was synthesised to address these challenges. The active site in Sion-105 is a three-coordinate boron (B) atom in a ligand that exploits Lewis acid-base interactions with F^- . The turn-off optical transduction mechanism relies on F^- -triggered quenching of the photoexcited red luminescence from the europium (Eu^{3+}) metal nodes. Both components of the MOF therefore contribute to its action as a F^- -selective optical sensor. When the ligand is linked to Eu^{3+} dimers to form crystalline Sion-105, it adopts a propeller-like structure with B in the center, which, unlike the planar ligands, inhibits access to the receptor. With the targeted F^- ion being the smallest anion commonly found in drinking water, non-selective binding with potentially interfering ions is prevented by further protecting the active site with bulky, protruding methyl groups. This architecture of the active site leads to size-selective, weak electrostatic interactions with the F^- , resulting in a regenerable sensor with a rapid turn-off optical response that stabilizes instantly. Using Sion-105, an easily reproducible F^- test method is devised and incorporated with a portable prototype sensor device that was designed and built in-house. The reliability of Sion-105 as a sensor is confirmed with blind tests on groundwater samples collected from three countries spanning the Middle East and

Far East Asia. Sion-105 is thus proposed as a practical solution for F^- concentration sampling that is safe and accessible to non-expert users in communities impacted by chronic fluoride toxicity.

3.3.1 Design and synthesis of Sion-105

The constituent blocks of Sion-105 were carefully selected to realize an effective F^- -sensing material. The B-functionalized tris(p-carboxylic acid)tridurylborane ligand ($tctb^{3-}$) was chosen because the central three-coordinate B acts as a Lewis acid active site for F^- ions, with the surrounding duryl groups offering size-selective steric protection from unwanted interferences. Eu^{3+} was selected as the metal node to exploit its visible-light emissive properties. UV irradiation of Sion-105 photoexcites the ligand, which then transfers energy to the radiative 5D_0 energy level of the Eu^{3+} ions via the antenna effect, described in Chapter 1. Subsequent $^5D_0 - ^7F_J$ ($J = 0-6$) transitions result in a bright characteristic Eu^{3+} luminescent emission, with a peak at 625 nm corresponding to the $^5D_0 - ^7F_2$ transition. This emission is quenched upon interaction of F^- ions with the B Lewis acid site, to which larger ions have limited access. The interaction of F^- with the B active site, rather than with the Eu^{3+} dimers, is indicated by the turn-off luminescence quenching response of Sion-105 to F^- . As is well known from the literature, substitution of a Eu^{3+} -coordinated H_2O molecule with a F^- ion would instead lead to a turn-on optical signal due to the subsequent decrease in vibrational coupling [59]. The reliability of Sion-105 as a sensor is confirmed with blind tests on groundwater samples collected from three countries spanning the Middle East and Far East Asia. Sion-105 is thus proposed as a practical solution for F^- concentration sampling that is safe and accessible to use.

The formation of Sion-105 occurs via self-assembly during a one-step reaction of H_3tctb with $Eu(NO_3)_3$ in a DMF/ H_2O solution at 120°C for 72 h. The resulting rod-shaped colourless crystals, shown in Figure 3.5a, with the formula $[Eu(tctb)(H_2O)]2DMF$, crystallize in the C_2/c monoclinic space group. The asymmetric unit of Sion-105 is seen in Figure 3.5b, and is composed of one Eu^{3+} atom, one $tctb^{3-}$ ligand, and one coordinated H_2O molecule, while the non-coordinated DMF molecules are disordered within the pores. The main constituent of the crystal structure of Sion-105 consists of binuclear Eu^{3+} clusters (Figure 3.5c), with two Eu^{3+} atoms a distance of 3.9679(11) Å apart, linked together by two μ_2 -bridging H_2O molecules and two $tctb^{3-}$ ligands with $\eta^1 : \eta^1$ -bridging modes. The interconnection between Eu^{3+} dimers and tridentate $tctb^{3-}$

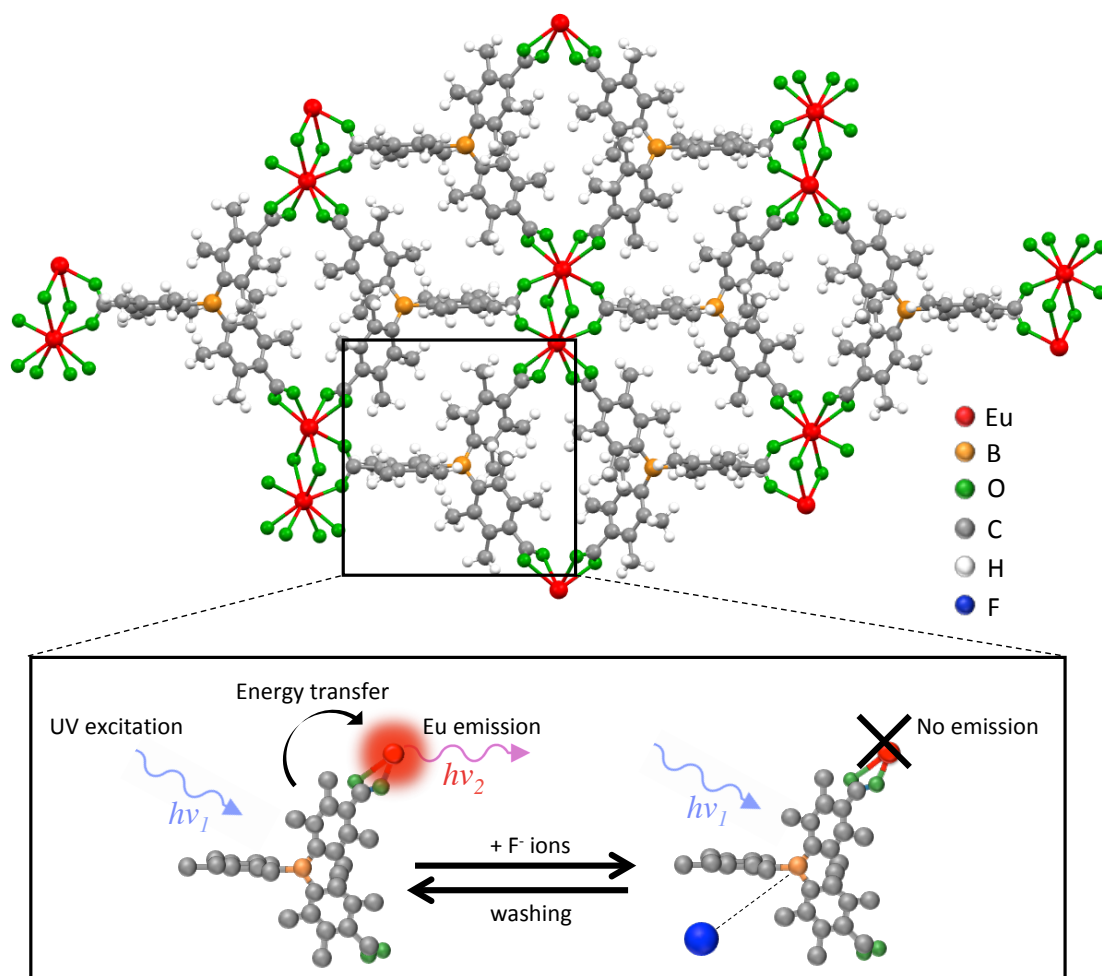


Figure 3.4 – Structure and proposed luminescence mechanism of Sion-105. The structure of Sion-105 consists of a sensitizing ligand coordinated to Eu^{3+} dimers that are bridged by two H_2O molecules. The inset below illustrates the proposed turn-off optical sensing mechanism, whereby interaction of F^- ions with the Lewis-acidic active site of the ligand leads to quenching of the Eu^{3+} emission. H atoms are omitted for clarity.

ligands leads to the formation of a polymeric framework extending in three dimensions. The phase purity of Sion-105 and its stability upon activation, immersion in pure water, and exposure to buffer solutions of pH 4 and 9 are confirmed by *Powder X-Ray Diffraction* (PXRD) as shown in Figure 3.5d and e.

The stability of Sion-105 is further demonstrated by *Thermo-Gravimetric Analysis* (TGA) measurements, which reveal thermal stability up to temperatures of 300°C . While non-porous to nitrogen, Sion-105 is porous to CO_2 at 195 K and 1 bar with a *Brunauer–Emmett–Teller* (BET) surface area of $216 \text{ m}^2/\text{g}$.

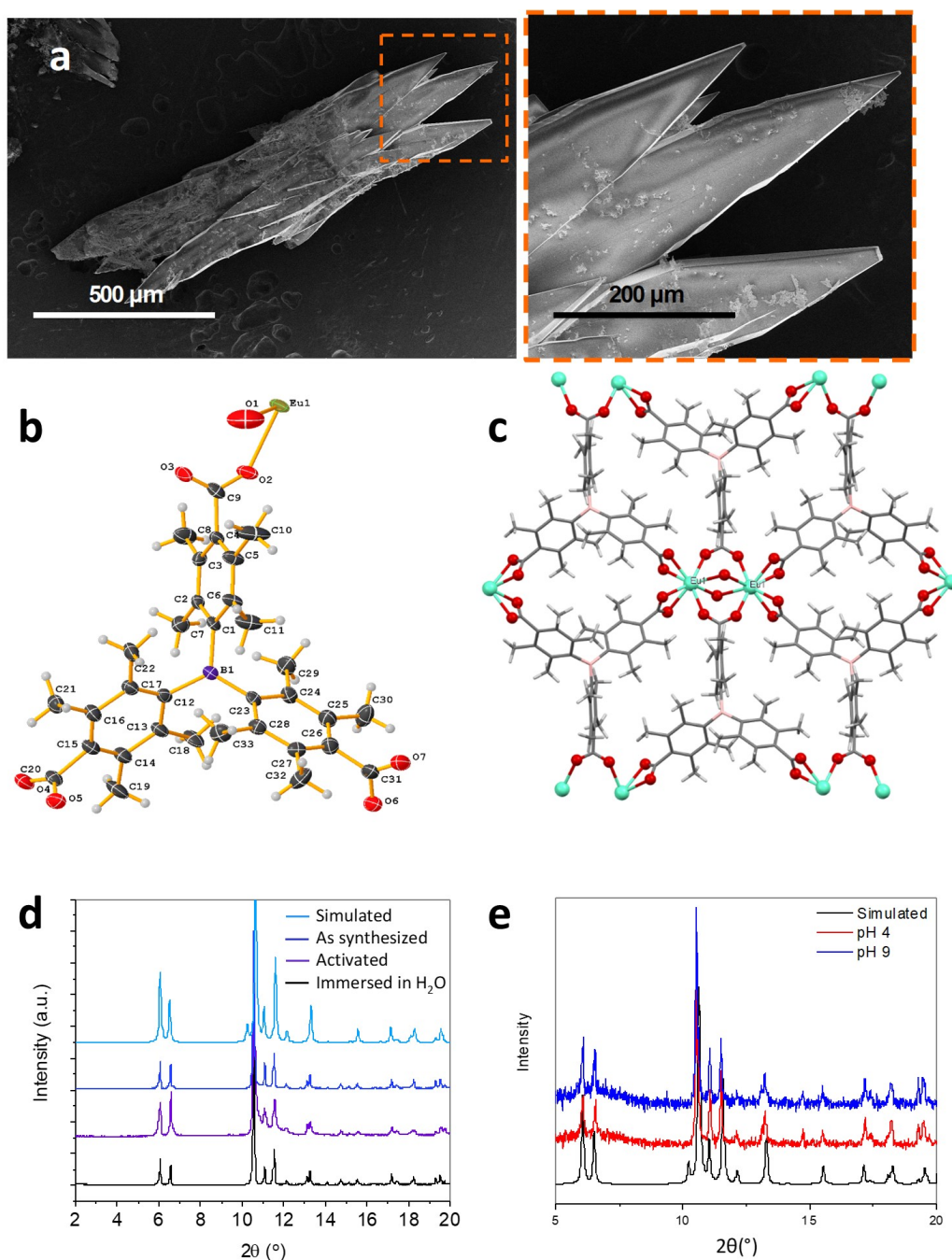


Figure 3.5 – Crystal structure of Sion-105. **a.** SEM images of as-synthesised Sion-105 crystals, **b.** Asymmetric unit of Sion-105 drawn with labels for all non-H atoms. Ellipsoids denote the respective atomic displacement parameters, **c.** A Eu³⁺ dimer and its coordination environment, viewed along [010], **d.** PXRD patterns indicate that Sion-105 maintains its crystal structure after activation and immersion in pure water, and **e.** in pH 4 and pH 9 buffer solutions.

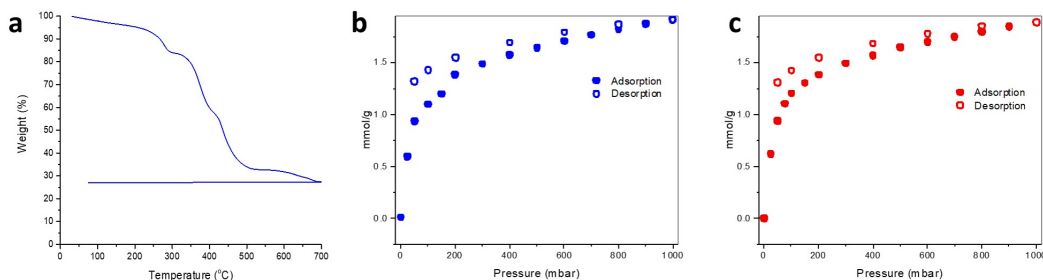


Figure 3.6 – Stability and porosity of Sion-105. **a.** TGA data showing stability of Sion-105 up to 300°C, and **b.** CO₂ adsorption-desorption isotherms collected on Sion-105 before, and **c.** after fluoride sensing experiments show a negligible change in BET surface area from 216 m²g⁻¹ (before experiment) to 205 m²g⁻¹ (after experiment).

3.3.2 Calibration of Sion-105 for fluoride

A simple method for quantifying the F⁻ concentration in water samples was devised with Sion-105 using a commercial fluorescence spectrometer (PerkinElmer LS55). This method yields a linear luminescence quenching response to F⁻ in the concentration range pertinent to drinking water, which is between 0.5 and 2.0 ppm. First, Sion-105 crystals are carefully ground into a fine powder. This powder (0.5 mg) is then suspended in 2.5 mL of *Tetrahydrofuran* (THF) and briefly sonicated to obtain a uniform dispersion. This is done because the hydrophobic nature of Sion-105 causes it to aggregate in pure aqueous solutions, while in THF the powdered crystals form a homogeneous suspension suitable for reproducible measurements. UV irradiation ($\lambda_{exc} = 350$ nm) of the Sion-105/THF suspension results in bright-red Eu³⁺-based emission centred at 625 nm. Then, 250 μ L of pure aqueous *Sodium Fluoride* (NaF) solution is added to the Sion-105/THF suspension and briefly shaken by hand before remeasuring the sample luminescence. The addition of NaF aqueous solutions with concentrations of 0.5 to 2.0 ppm results in a linear luminescence quenching response seen in Figure 3.7 such that an aqueous NaF solution with a concentration beyond the safe upper limit of 2.0 ppm yields close to the maximum quenching, within a 0.1 ppm *Limit Of Detection* (LOD).

To determine the F⁻-B association strength, and to optimize F⁻ detection conditions, NaF titrations were performed in which increasing amounts of NaF were introduced to 0.5 mg samples of Sion-105 and the resulting luminescence quenching observed. To perform a titration, five vials of 0.5 mg of Sion-105 suspended in 2.5 mL of THF were prepared. The suspensions were sonicated for 5 minutes, and the luminescence intensity

of each suspension was recorded. Then, 250 μL of aqueous NaF solution was added to each vial, with NaF concentrations ranging from 0.0 ppm (blank) to 2.0 ppm in steps of 0.5 ppm. Subsequently, the change in luminescence intensity was recorded. The titrations were repeated 15 times, and the mean of the results used to plot a curve of I/I_0 (luminescence quenching) versus F^- concentration. The graphs (in Figure 3.7) are normalized to the 0.0 ppm blank. The inset of Figure 3.7a is a box chart comprising the data from all 15 NaF titrations, where whiskers indicate minimum and maximum values, median lines are indicated as horizontal lines and mean values are indicated by solid squares. It is worth noting that upon introduction of the aqueous test sample, the overall F^- concentration in the measurement vial is an order of magnitude lower than that of the sample itself. Indeed, the sensitivity of Sion-105 is thus in the range of 0.0091 ppm. For the purpose of physiologically relevant water sampling, however, suspending the MOF in THF prior to introducing the sample optimizes the uniformity of the suspension and thus the reproducibility of the results.

The positive deviation of the *Stern-Volmer* (SV) plot (Figure 3.7a) from linearity is characteristic of fluorophore-quencher systems in which both static and dynamic interactions impact the luminescence quenching behaviour [107]. Static luminescence quenching is generally associated with the formation of ground-state complexes upon addition of the quencher, whereas dynamic interactions are associated with diffusion-controlled quenching in which collisions between quenchers and excited fluorophores result in deactivation of the excited states. Combined static and dynamic quenching is often observed in fluorophore-quencher systems containing two populations of fluorophores, one of which is less accessible to quenchers than the other [108]. This is a characteristic feature of systems in which the quencher has limited access to some of the active sites buried in the fluorophore [109]. In the case of Sion-105, the introduction of F^- results in a $\text{B} \cdots \text{F}$ interaction that prevents emissive de-excitation, accounting for static quenching, while increasing the concentration of F^- promotes more interactions with the B active sites (protected by duryl groups of the ligand), resulting in the quadratic dependence described by Equation 3.1,

$$\frac{I_0}{I} = (1 + K_{SV}[F])(1 + K_a[F]) \quad (3.1)$$

where I_0 is the emission intensity from Sion-105 in the absence of F^- , I is the intensity in the presence of F^- , K_{SV} is the SV constant describing the dynamic quenching efficiency, and K_a is the association constant describing the efficiency of $\text{B} \cdots \text{F}$ interactions. While

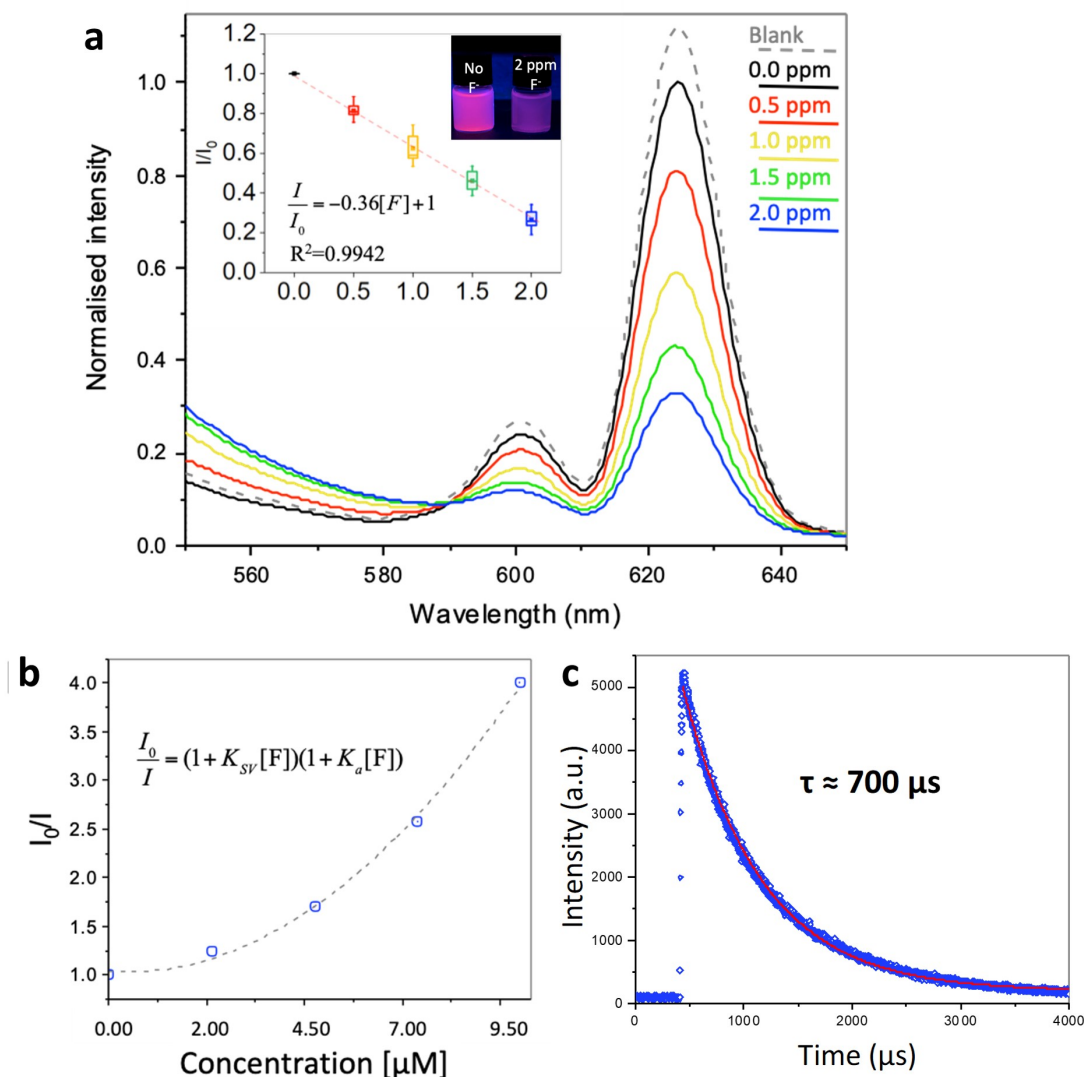


Figure 3.7 – Luminescence properties of Sion-105. **a.** Representative spectra from one NaF titration show the quenching of Sion-105 luminescence at varying F^- concentrations. Inset: Photograph illustrating drop in luminescence intensity upon addition of F^- to Sion-105 suspension, and a box chart constructed from 15 titrations illustrating the linear quenching response of Sion-105 to F^- . Blank refers to the Sion-105/THF suspension before addition of water sample. Both graphs are normalized to 0.0 ppm. **b.** Nonlinear Stern-Volmer plot of quenching with increasing F^- concentration, **c.** Eu^{3+} -based long-lifetime phosphorescent emission from Sion-105

K_{SV} and K_a have similar values (9.125×10^4 and $9.126 \times 10^4 M^{-1}$, respectively), as determined from a nonlinear regression analysis of the experimental data plotted in Figure 3.7b, further consideration highlights the dominance of static quenching in Sion-105.

Given the measured luminescence lifetime of Sion-105 in the absence of F^- ($t_0 = 704 \pm 3 \mu s$) (Figure 3.7d), the bimolecular quenching rate constant, k_q , which reflects the collisional quenching efficiency, is calculated from Equation 3.2,

$$k_q = \frac{K_{SV}}{\tau_0} \quad (3.2)$$

The resulting value of $k_q = 1.30 \times 10^8 \text{ M}^{-1}\text{s}^{-1}$ is two orders of magnitude lower than that expected from purely diffusion-controlled quenching ($10^{10} \text{ M}^{-1}\text{s}^{-1}$), as is typical of systems in which the steric shielding of fluorophores limits the number of collisional quenching encounters taking place. The dominance of static luminescence quenching in Sion-105 is further shown by the negligible decrease in the emission lifetime from 704 ± 3 to $670 \pm 2 \mu s$ at a F^- concentration of 2.0 ppm. The value of K_a obtained from the experimental data can be used to qualitatively estimate the concentration of nonemissive $B \cdots F$ pairs in the sample as a function of F^- concentration using Equation 3.3

$$K_a = \frac{[B \cdots F]}{[B][F]} \quad (3.3)$$

$[B \cdots F]$ and $[F^-]$ represent the concentrations of $B \cdots F$ pairs and F^- after 300 s of introducing the water sample to the Sion-105 suspension. Although the response time of Sion-105 in low concentrations of F , such as those relevant to the desired sampling range, is extremely fast, with the signal equilibrating within seconds, a conservative equilibration time of 300 s was applied. This is because in very high concentrations of around 500 ppm or more, diffusion of the F^- analyte through the pores of the MOF is slightly slower, resulting in a slightly longer equilibration time, as seen in Figure 3.8. $[B]$ is the molar concentration of B active sites in the measurement suspension, considering 1 mole of B per mole of MOF. If all of these active sites were accessible and homogeneously distributed in solution, 100% of the B sites would be occupied by a F^- ion at a 1:1 molar ratio of B/F . However, the luminescence quenching behaviour observed in the Sion-105 method suggests that even in the presence of a 20.0 ppm F^- sample, a maximum of 46% of all B active sites tend to be interacting with F^- ions, indicating that not all B active sites are occupied. This could be because several F^- ions may be interacting with a given B receptor site.

The mechanism of luminescence quenching in Sion-105 was probed by phosphorescence spectroscopy measurements on an isostructural gadolinium (Gd) MOF, Gd-Sion-105

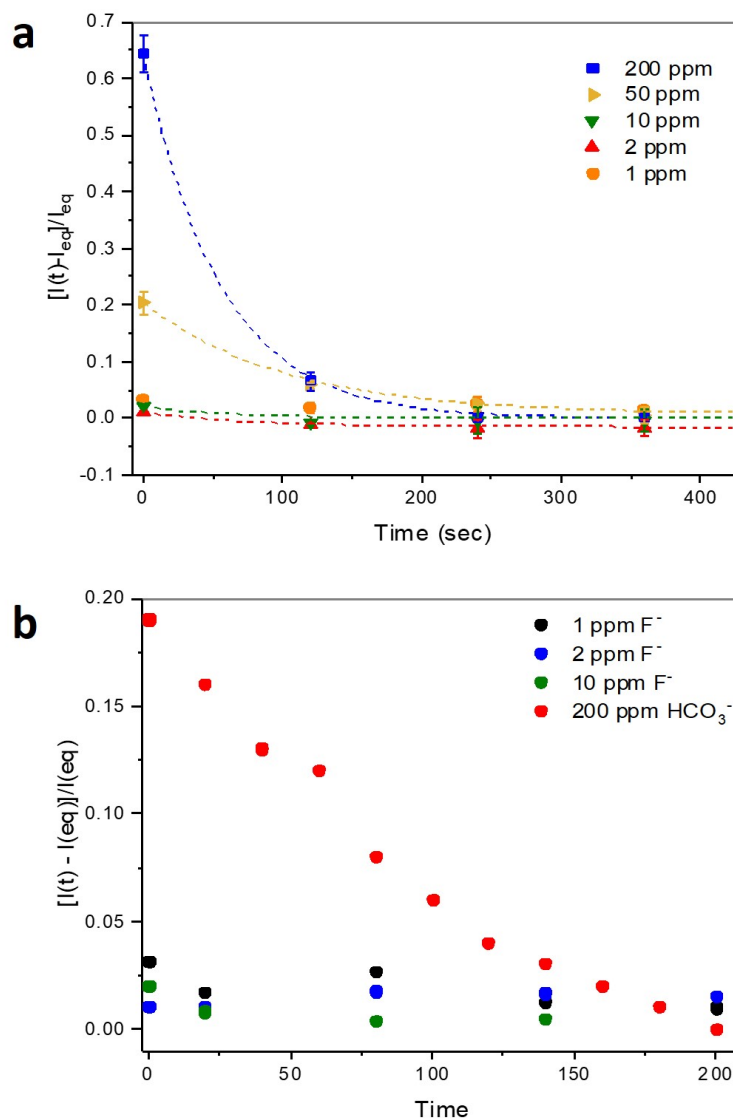


Figure 3.8 – Response time of Sion-105. **a.** Measurements of time-dependent intensity normalized to equilibrium intensity for a range of F^- concentrations from 1 ppm to 200 ppm demonstrate the fast response time of Sion-105. In particular, in the range from 1 ppm to 10 ppm (i.e. five times higher than the maximum concentration of interest), the response of Sion-105 to F^- is instantaneous. This instantaneous response is exploited to isolate the F^- signal from potential. **b.** The response time (in seconds) of Sion-105 to HCO_3^- (red circles) over a span of 200 s shows how a rapid testing protocol can be used to isolate the signal due to F^- .

(Figure 3.9). Because the emissive state of Eu^{3+} is excited via the antenna effect from the lowest ligand triplet level (LT_1), it is informative to probe any shifts in LT_1 that may

result from the presence of F^- in the structure. The choice of Gd^{3+} is based on the high energy of its emissive ${}^6P_{7/2}$ state, which prevents the possibility of ligand-to-metal energy transfer, thus allowing the triplet energy of the ligand to be probed. The lowest-energy peak in the ligand phosphorescence spectrum of Gd-Sion-105, which is associated with LT_1 , undergoes a negligible shift when F^- is present in the structure, suggesting that rather than a significant shift in LT_1 , the interaction between F^- and B results in the formation of nonradiative decay pathways that quench Eu^{3+} emissions.

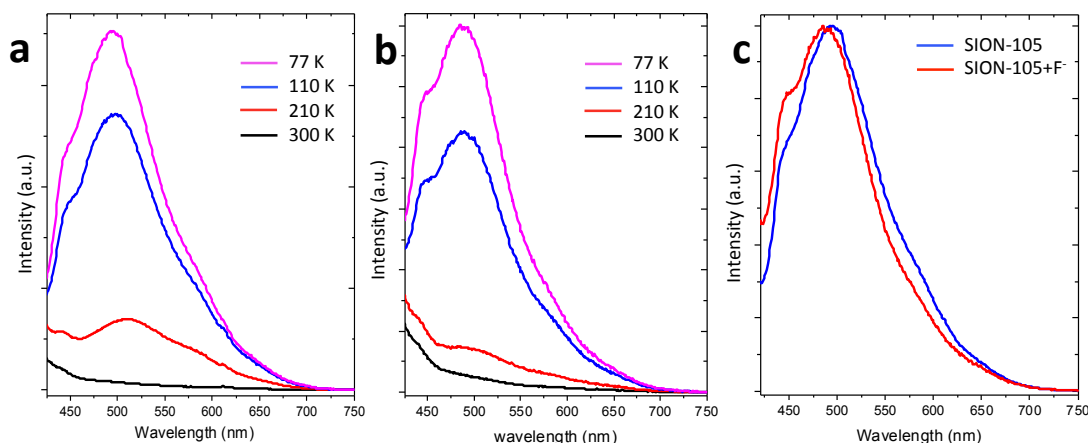


Figure 3.9 – Phosphorescence spectra of Gd-Sion-105. Temperature-dependence of emissions of **a.** unloaded, and **b.** F^- loaded Gd-Sion-105 confirm the phosphorescent nature of the ligand emission; **c.** Comparison of ligand-based phosphorescence spectrum from Gd-Sion-105 before and after loading with F^- show nominal shift in the ligand triplet energy, thus suggesting the formation of non-radiative decay pathways that lead to luminescence quenching in Gd-Sion-105 in the presence of F^- .

3.3.3 Structural Advantages of Sion-105

The specific advantages of the active-site structure in Sion-105 are threefold. First, the rigidity of Sion-105 and the protection of the B sites limit the $B \cdots F$ interaction to being electrostatic in nature. The electrostatic nature of the $B \cdots F$ interaction is supported by *X-ray Photoelectron Spectroscopy* (XPS) measurements probing the B chemical environment before and after the addition of F^- . Because of the lack of reports in the literature on $B \cdots F$ XPS in metal complexes, the $tctb^{3-}$ ligand was analyzed before and after exposure to F^- and used as a benchmark to locate the expected B-F peak, as seen in Figure 3.10. The XPS spectra of as-made and F^- -loaded samples of

Sion-105 corroborate the presence of F^- in the MOF sample; however, no change is observed in the B environment in the case of the MOF. Because of the weak nature of this interaction, the structure is protected from potential collapse, phase transition, and partial loss of crystallinity, which would have been observed in the case of covalent B-F bond formation because the B geometry would shift from trigonal to tetrahedral. PXRD patterns of Sion-105 before and after exposure to aqueous solutions of several ions (Figure 3.11) confirm the preservation of the crystal structure, even upon loss of emission intensity in the presence of F^- . The stability of Sion-105 in the presence of various ionic species was confirmed by leaving samples of Sion-105 overnight to soak in pure H_2O , pure THF, and solutions of F^- , HPO_4^- , and SO_4^{2-} . After re-isolating the MOF via centrifugation and drying in air, PXRD patterns seen in Figure 3.11 show no loss of crystallinity. Furthermore, single-crystal X-ray diffraction on the F-loaded Sion-105 crystals confirmed that B retains its trigonal geometry while the pores are filled with disordered guest molecules. Finally, *Inductively-Coupled Plasma Optical Emission Spectroscopy* (ICP-OES) reveals that a negligible amount of Eu^{3+} is leached out after the F^- loading (Table 3.1). These findings confirm that the B sites are sufficiently protected by the protruding methyl groups in the ordered structure to ensure a weak interaction between F^- and B.

F^- [ppm]	% Eu^{3+}
2	1.34
10	1.56

Table 3.1 – Results of Eu-ICP-OES analysis of Sion-105 after introducing F^- .

The second advantage of the Sion-105 active-site architecture lies in how the Eu_2^{3+} dimers distort the ligand into a rigid propeller shape, to form pores with restricted apertures. Figure 3.12a shows how the binding site at the center of the ligand is surrounded by oblique duryl groups. Not only does this lead to the reversible electrostatic nature of the Sion-105- F^- interaction, that is depicted in Figure 3.12b, it importantly prevents access to the active site by larger anions that may potentially act as interferences. The channels of Sion-105, visualised in Figure 3.12c, therefore have restricted access. The net topology of Sion-105 is shown in Figure 3.12d, with the B-active sites coloured in pink and the Eu_2^{3+} dimers coloured in green.

This restricted nature of the resulting binding site, illustrated in the space-filling model in Figure 3.13, enhances the selectivity of Sion-105 to F^- . Measurements of emission

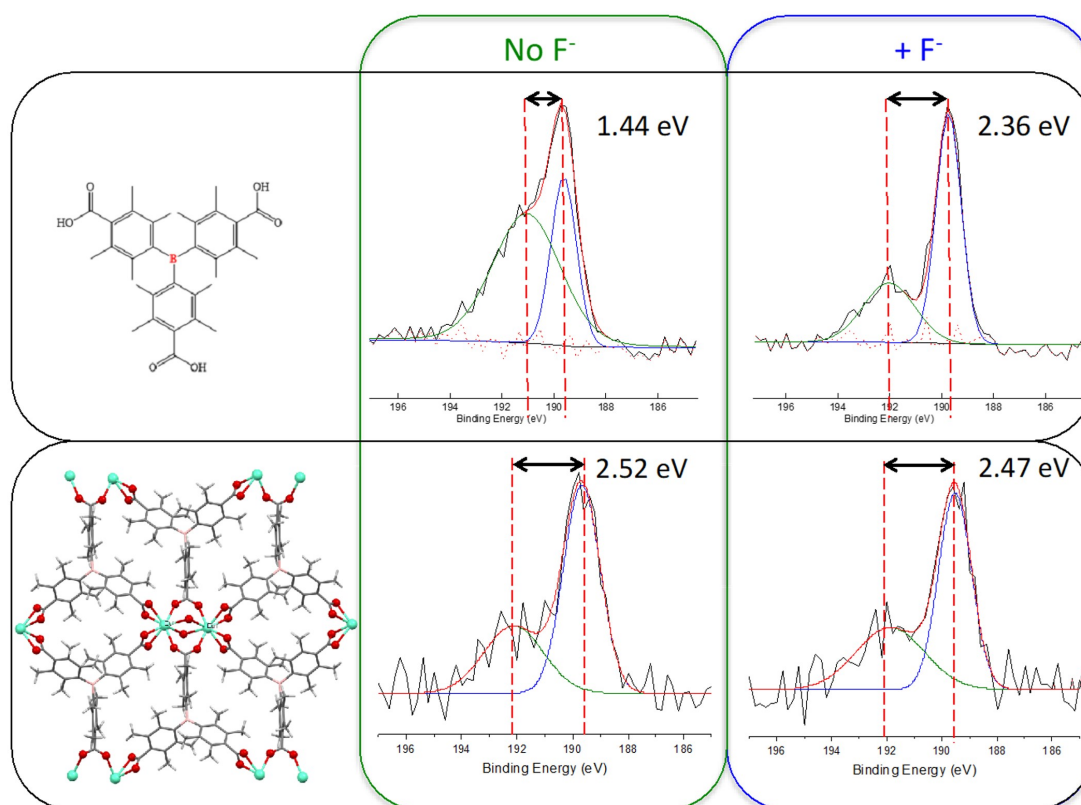


Figure 3.10 – Sion-105- F^- interactions. XPS spectra of B 1s peak of free H_3tctb ligand and Sion-105 with and without F^- . The peak around 189 eV is associated with a boron sub-oxide present on the surface, while the higher-energy peaks are associated with the ligand B. The approximate 1 eV shift of the high-energy peak in the presence of F^- in the free ligand suggests a bond-induced change in the chemical environment of B. This shift is consistent with observations reported in the literature. In the case of Sion-105 however, the peak positions are marginally different after the introduction of F^- , thus supporting the hypothesis that the $B \cdots F$ interaction in Sion-105 is weak in nature.

intensity after adding equal (2.0 ppm) concentrations of a range of anions and cations commonly found in drinking water show that only F^- , being the smallest anion, has a significant quenching effect (Figure 3.13a). Furthermore, measurements in which F^- was added to three different purchased bottled mineral water samples, each with varying concentrations of commonly found anions and cations listed in Table 3.2, also showed a linear quenching response selective to F^- . These samples were intentionally contaminated with F^- to achieve final F^- concentrations between 0.5 to 2.0 ppm, and the results of measurements carried out are plotted in Figure 3.14b. N/A indicates no information available.

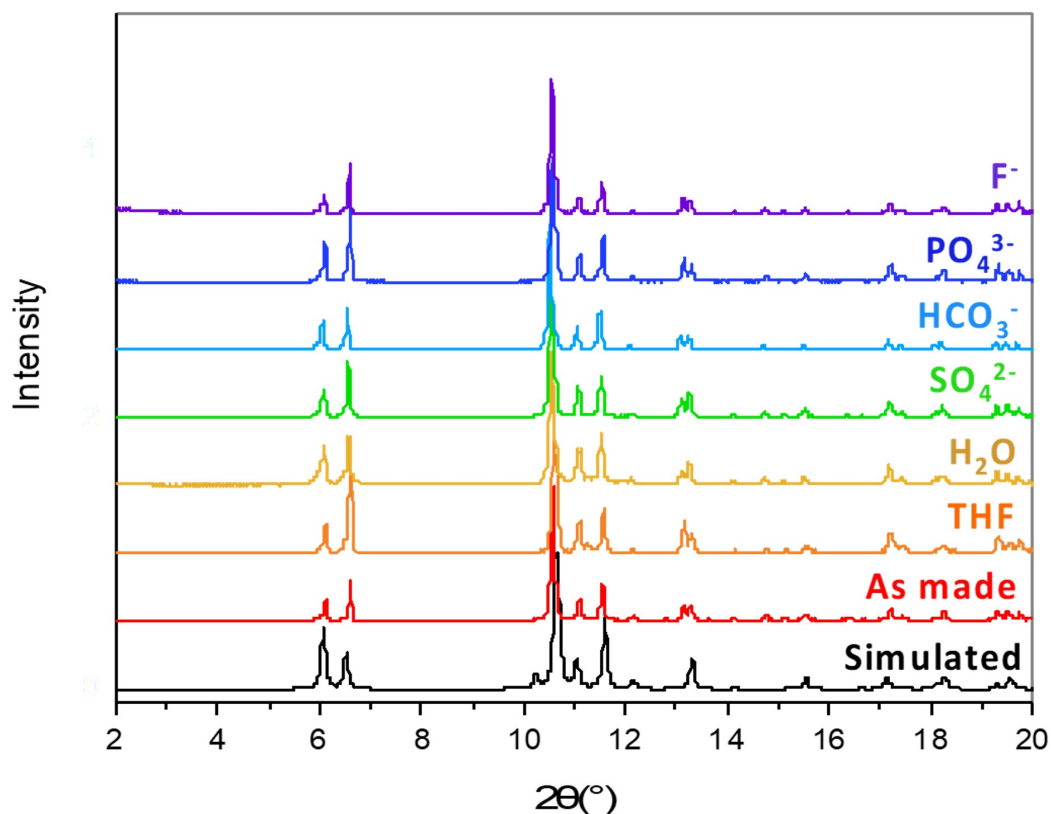


Figure 3.11 – Stability of Sion-105 in aqueous salt solutions PXRD spectra of Sion-105 after immersion in aqueous solutions of various salts commonly found in drinking water confirms the stability of the MOF, even in the presence of NaF solution, which results in luminescence quenching.

Finally, the advantage of weak B...F interactions is that they allow us to exploit the easy reversibility of the method by simply washing in ethanol to flush out the F⁻ quenchers, thus regenerating the Eu³⁺ luminescence and the functionality of the MOF (Figure 3.13c). Unlike other systems reported in the literature, Sion-105 is specific to F⁻ despite relying on reversible, weak interactions. While direct comparison with reports from the literature is challenging because of the variation of experimental conditions used in different systems (reports include the detection of F⁻ in organic solvents rather than in water or the use of tetra-n-butylammonium fluoride as the analyte rather than using the naturally occurring fluoride salts, and in some cases, reaction times are very slow and therefore the signal stabilization can last for hours), the performance of Sion-105 meets the requirements for F⁻ sensing in drinking water.

Overall, these properties, in addition to its facile, high-yield, and reproducible synthesis,

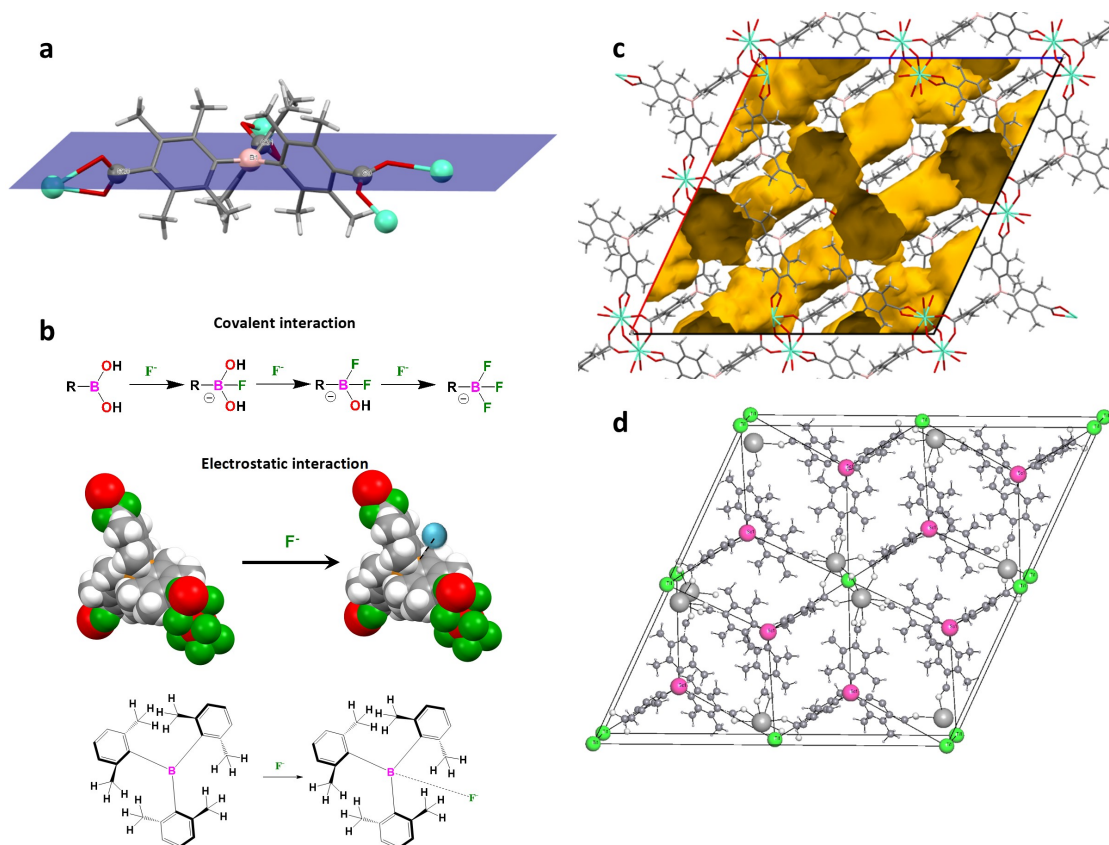


Figure 3.12 – Binding site of Sion-105 **a.** A propeller-shape $tctb^{3-}$ ligand with a plane drawn across the C9, C20, and C31 atoms. Note the oblique position of the duryl groups towards this plane. A view along [154]. **b.** Schematic illustration of the covalent B-F interactions in boronic acid (top) vs electrostatic B...F interactions in Sion-105 (bottom). In the case of covalent interactions, the OH groups in boronic acid are substituted by F^- ions to form covalent B-F bonds, which can be broken by the addition of a strong base. The spacefill model of Sion-105 shows the extent of B receptor (orange) protection by the surrounding methyl groups, which limit access to F^- ions (turquoise). The limited access means that the B-F interactions are electrostatic, and can be reversed by simply washing the MOF to flush out F^- . **c.** Packing of the crystal structure of Sion-105 with the structural voids visualized with MERCURY marked as golden surfaces. Calculation details: probe radius 1.2 Å; grid spacing 0.7 Å. **d.** Net topology of Sion-105. Pink spheres denote the 3-coordinated node positioned in the center of the $tctb^{3-}$ ligand, whereas green spheres represent the 6-coordinated node corresponding to the Eu_2^{3+} dimer. The atomic structure of Sion-105 is overlaid onto this topological diagram. A view along [010].

place the performance of Sion-105 in a promising position with respect to previously reported work, which relies on the formation of covalent B-F bonds with a more exposed receptor [110]. An added advantage of exploiting the structure of the active site for higher sensitivity and selectivity and relying on Eu^{3+} emissions alone for optical transduction

Ion	Sample 1	Sample 2	Sample 3
F ⁻	0.01	N/A	N/A
HCO ₃ ⁻	86.9	357	360
Cl ⁻	4.1	5	2.2
HPO ₄ ⁻	N/A	N/A	0.03
SO ₄ ²⁻	2.74	10	941
Ca ⁺	19.37	78	47
Mg ³⁺	4.02	54	N/A
Na ⁺	2.2	N/A	10.5
NO ₃ ⁻	N/A	14	25.6
Silica	N/A	14	25.6
K ⁺	<0.2	1	1.4

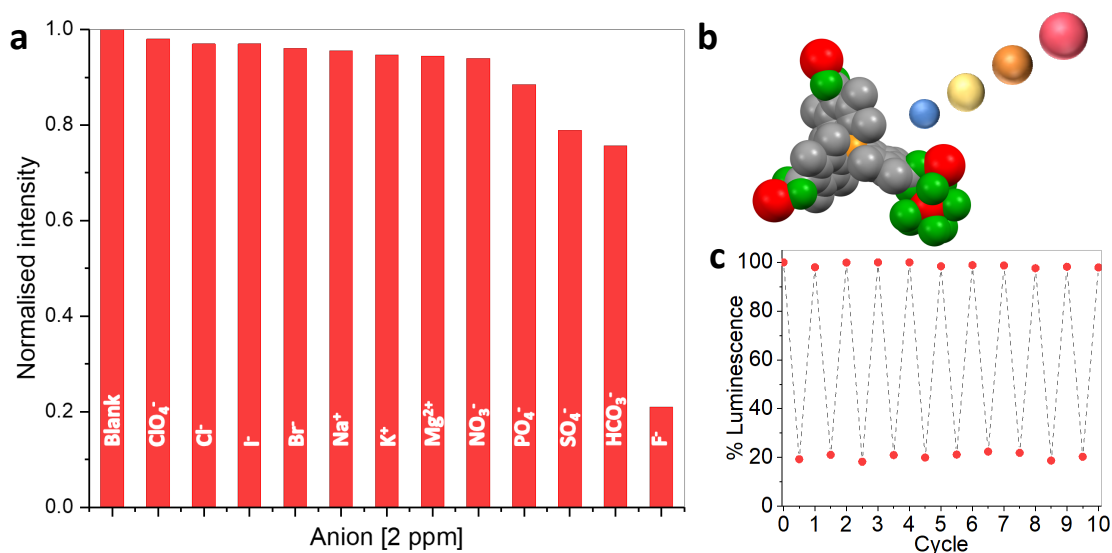
Table 3.2 – Contents of bottled mineral water tested using Sion-105.

Figure 3.13 – Selectivity of Sion-105 to fluoride. **a.** Fluorescence intensity measured after subsequent additions of a range of potential interferences to Sion-105 demonstrate its selectivity to F⁻. **b.** Space-filling model of the postulated binding site in Sion-105 (H omitted for clarity), which explains the size-selectivity of the B site by scaled comparison to F⁻ (blue), Cl⁻ (yellow), Br⁻ (orange) and I⁻ (pink); **c**) Recyclability of Sion-105 observed over ten cycles. Note that in **a** and **c**, the luminescence intensity is normalized to the pure Sion-105/THF suspension (before addition of aqueous samples), and not to the 0.0 ppm blank as in Figure 3.7.

lies in the fact that monitoring the intensity of sharp, single-wavelength emissions such as those from Eu³⁺ is far simpler than monitoring that from dual-emission compounds. This simplicity of measurement allowed us to construct a low-cost, portable fluorimeter device for use in conjunction with Sion-105.

3.3.4 Integration of Sion-105 into a portable device

The performance of Sion-105 makes it a promising contender for real-world F^- -sensing applications. Aside from existing portable electrochemical devices, which require frequent calibration and careful handling to extend their shelf life, the colorimetric sensing solutions that exist suffer from interferences that may require complicated or hazardous sample preparation steps to remove. These methods are thus restricted to use in laboratories by skilled technicians, and a rapid, reliable method for untrained users in need of frequent sampling is needed. To address this, we designed and constructed a miniaturized fluorimeter device as a portable prototype for water sampling with Sion-105 (Figure 3.14). The compact (10 cm x 10 cm x 12 cm) device consists of a cuvette holder mounted internally with three 360 nm UV LEDs (LED Engin LZ4-04UV00), a 590 nm long-pass filter, and a sensitive photodiode integrated with an operational amplifier (Burr-Brown OPT 301). The holder is fitted with an anodized aluminium lid and a safety switch to ensure that the UV *Light-Emitting Diodes* (LEDs) can turn on only when the lid is placed over the holder. The device is powered by a 12 V source and consists of an LED display connected to a microcontroller (Arduino UNO) coupled to a voltage divider circuit. The information visualized on the display is the change in voltage across the photodiode on addition of F^- , converted to the corresponding F^- concentration. Measurements are carried out using prepared vials of the Sion-105/THF suspension (0.5 mg in 2.5 mL). First, after briefly shaking the suspension, the vial is placed in the holder. Placing the lid over the holder releases the safety switch so as to turn on the UV LEDs that excite the sample, and a blank measurement of the resulting Sion-105 luminescence is acquired. Subsequently, the water sample is added to the vial, which is shaken and reintroduced into the holder. The Arduino is programmed to convert the change in luminescence intensity to its corresponding F^- concentration, which is displayed on the LED screen. Because of the nature of the $B \cdots F$ interaction in Sion-105, no recalibration is needed prior to measurements, even after regeneration of the material.

Using this device, we tested samples of groundwater taken from Vietnam, the United Arab Emirates, and Saudi Arabia, which we labelled ‘GW1’, ‘GW2’ and ‘GW3’. The concentrations of F^- in these samples measured using Sion-105 showed remarkable agreement with the results from *Internal Conversion* (IC). These results, listed in Table 3.3, highlight the performance and reliability of Sion-105 as a F^- sensor and, coupled with the portable device, cement its potential as a user-friendly solution for water sampling in remote areas where frequent F^- concentration monitoring is essential.

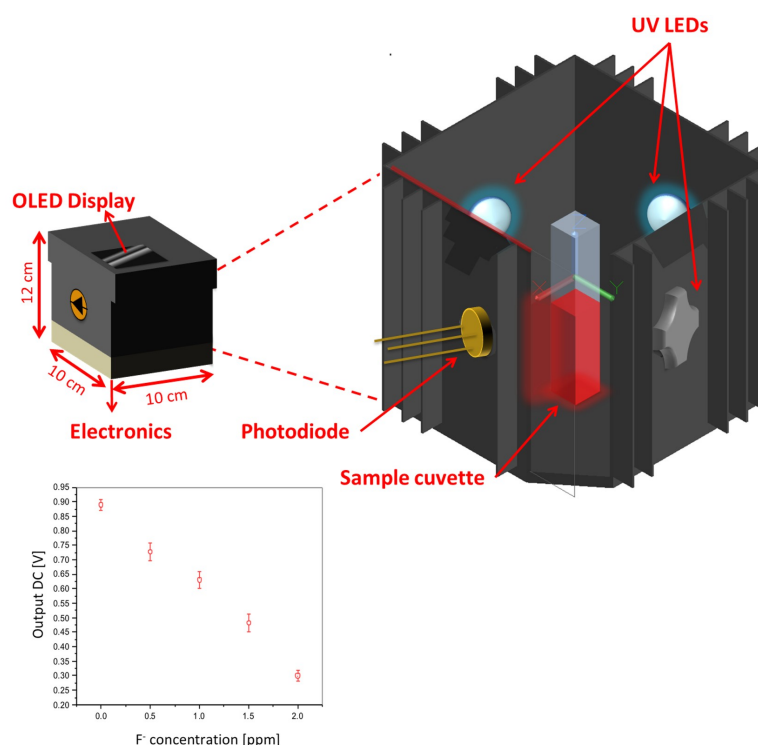


Figure 3.14 – Sion-105-based portable sensor. Schematic diagram of the portable device used with Sion-105. Data in inset shows the linear response in voltage across photodiode upon introduction of F^- ions to water samples. The data presented is an average response measured in three different samples of purchased bottled mineral water, contents of which are listed in Table 3.2

3.4 Conclusions

In this Chapter, we discussed the tailored design of a new luminescent MOF structure for the selective detection of trace ionic contaminants in drinking water sources. We began with a general overview of the different types of sensors into which MOFs may be incorporated, and justified our interest in focusing on a luminescence-based sensor. We then described how we selected the building blocks for our new MOF. The ligand acts as a receptor to interact with the target analyte, the luminescent lanthanide nodes act as a reporter to signal that an interaction has taken place, and the overall rigid structure acts as a molecular sieve, making our MOF highly selective in the presence of a wide range of potential interferences, in various concentrations. Finally, we described how we designed and fabricated a small device that can be used to carry out reproducible measurements with our MOF, without the need for repeated calibration. The fact that the MOF we report is easily regenerable by washing with ethanol is favourable in terms

Sample	$[F^-]$ (IC)	$[F^-]$ (Sion-105)
GW1	0.472	0.489 ± 0.09
GW2	1.780	1.75 ± 0.15
GW3	0.435	0.47 ± 0.12

Table 3.3 – ppm Concentrations of F measured in three groundwater samples taken from wells in Vietnam (GW1), the U.A.E. (GW2), and Saudi Arabia (GW3). Results of measurements via ion chromatography and Sion-105 show strong agreement.

of the environmental impact of the test method.

The overall performance of Sion-105 in comparison to other candidates for the detection of F^- from recent literature is given in Table 3.4. It should be noted that in the test method that we developed, which we designed for the practical purpose of physiologically relevant water sampling, we suspend the MOF in THF prior to introducing the sample. This optimizes the uniformity of the suspension and thus the reproducibility of the results. In evaluating the performance of the MOF itself as a sensor, we consider that upon introduction of the aqueous test sample, the overall F^- concentration in the measurement vial is an order of magnitude lower than that of the sample itself. The sensitivity of Sion-105 is thus approximately 0.0091 ppm.

Ref.	Description	Sensitivity	Selectivity	H ₂ O Samples	Recyclability
[111]	MOF-76	1900 ppb	Moderate	No	No
[101]	H ₃ BO ₃ MOF	67 ppb	Good	Yes	Not specified
[103]	FITC@MOF	15 ppb	Good	Yes	No
This work	Sion-105	9.1 ppb	Good	Yes	Yes

Table 3.4 – Comparison of Sion-105 with existing MOF-based F^- - anion sensors for drinking water sampling

In the following Chapter, we present an alternative approach to achieving luminescence, which we implement for a different application. We explore the design, synthesis, and characterisation of a luminescent OMIM for white light emission.

4

A Luminescent OMIM for White Light Emission

In the previous Chapter, we described the design, characterisation, and synthesis of a novel luminescent *Metal-Organic Framework* (MOF) for sensing. While the linkers of our luminescent MOF, named Sion-105, are functionalised to interact with a target analyte, the MOF relies on luminescence from its Eu^{3+} metal clusters to report that an interaction has taken place. In this Chapter, we take an entirely different approach to the application-targeted design of luminescent, porous crystals.

We report a new, luminescent *Organic Molecule of Intrinsic Microporosity* (OMIM) for white light emission. Achieving broad-spectrum white-light emission from a single molecular species is a challenge. We describe how we took inspiration from natural bioluminescent organisms to create an OMIM, which we named Cu_2L_3 , that emits white light. The broad emission of Cu_2L_3 arises from its biomolecule-inspired ligand. In forming a coordinated metal complex from this ligand, we have two advantages with respect to an uncomplexed molecular emitter. First, the formation of void spaces in our rigid metal complex allows us to exploit tuneability of the emitted colour via host-guest chemistry. Second, the rigidity of the complex results in an enhancement of the *Photoluminescence Quantum Yield* (PLQY) compared to the uncomplexed emitter. The work presented in this Chapter is based on a manuscript entitled "Tuneable luminescent from a biomolecule-inspired single species emitter of white light", by F. M. Ebrahim¹ et. al, which is currently in submission. The authors have also filed a patent of the same name, which is currently under consideration. In the following section, we precede a detailed description of the work with a brief introduction to white light emission.

¹The contribution of F. M. Ebrahim was to conceive the project, synthesise the material, carry out the characterisation of optical properties, and write the manuscript with contributions from all authors.

4.1 White Light Emission

Up to one-fifth of the energy produced globally is spent on ambient and display lighting [112–115]. The birth of the blue LED has led a transition to more efficient, solid-state, lighting solutions that provide some relief to the energy expense of traditional technologies. Semiconductor LEDs suffer, however, from relatively high cost and relatively poor light quality, and have a limited large-area applicability [116, 117]. The opportunities for improvement have fuelled a surge of interest in developing alternative technologies, such *White Organic Light-Emitting Diodes* (WOLEDs).

Organic LEDs in general possess unique advantages including easy processability, mechanical flexibility, and the prospect of providing high-efficiency diffuse lighting; features that offer them a key position in future, large-area, thin and flexible lighting solutions [118–120]. The seminal first reports of efficient green *Electroluminescence* (EL) from *tris* (8-hydroxyquinoline) aluminium (Alq3) in 1987 [121] and from *poly*(*p*-phenylene vinylene) (PPV) in 1990 [122], served to mobilise research into the use of organic EL emitters for display technology. Particularly attractive aspects include their easy solution-processable production methods, high luminance, wide viewing angle, low operating voltage, and potential light emission spanning the entire visible spectrum. Unlike LCDs, OLEDs are self-emitting, and in the absence of backlighting, can be made ultra thin, flexible, and compact.

The first example of an OLED that exhibited broad-spectrum white light was reported in 1995 [123] by Kido et. al, who vacuum-deposited layers of Alq3 doped with different fluorescent emitters. Since then, much like their semiconductor counterparts, the bulk of WOLEDs rely on combining discrete, multi-component (blue and yellow, or red, green and blue) emitters to obtain white light [124, 125]. The most common approach to generating white light in an organic device is to stack emitters with varying emission colours over each other, as illustrated in Figure 4.1.

The stacked emissive layer is typically sandwiched between a transparent anode such as *Indium Tin Oxide* (ITO), and a low-work-function cathode. Layers of appropriately-selected organic *Hole Transport Material* (HTM) and *Electron Transport Material* (ETM) are applied to the anode and cathode respectively. When an external bias is applied, electrons are injected from the cathode, and holes from the anode, into the layers. The ETM (HTM) layer serves to block the transport of holes (electrons) to the cathode(anode). The layers are therefore chosen according to the positioning of their energy levels, so that

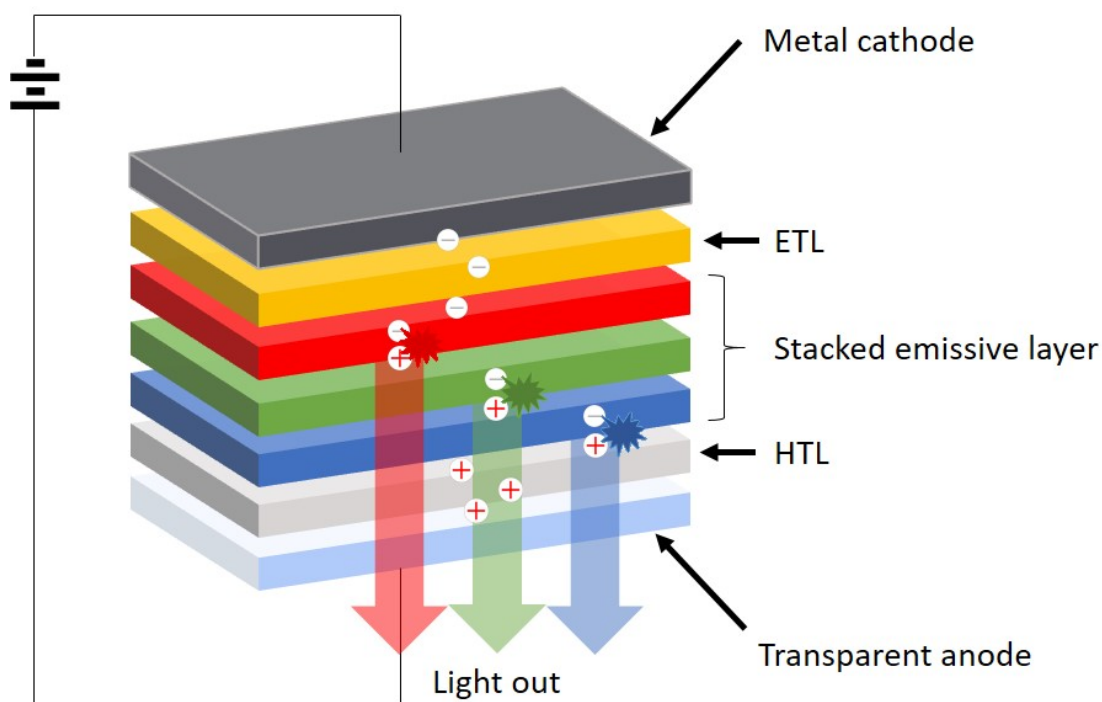


Figure 4.1 – Structure of a stacked WOLED device. Red, green, and blue emitters are typically layered over each other, and sandwiched between a metal cathode and a transparent anode that allows the light to be coupled out. Electron- and Hole-transport layers (ETL and HTM) promote charge injection into the emissive layer, where radiative recombination occurs.

they favour charge injection into the emissive layer, where the injected electrons and holes form excitons, which radiatively recombine. In stacked WOLEDs the recombination occurs first on the blue emitters, where high-energy excitons are formed that are then transferred to the lower-energy emissive layers. It is important to ensure that not all the higher-energy excitons are harvested by lower-energy emitters in the adjacent layers, and this sometimes addressed by introducing additional interfaces into the stack. Maintaining a balanced distribution of emission peak intensities in such structures is a challenge, and often requires complicated and expensive device fabrication procedures. These bottlenecks fuel the hunt to develop single-species white light emitters for OLED applications. A single-species white light emitter with high photoluminescence quantum yield, though challenging to realize, would be the first step towards stable and efficient WOLEDs with viable market penetrability [126, 127].

There are a number of different mechanisms by which broad-spectrum white light emission may arise from a single emitter. These include excimer formation, *Energy Transfer* (ET)

or *Charge-Transfer* (CT) transitions, and *Excited-State Intramolecular Proton Transfer* (ESIPT), and phosphorescence. Excimers are molecules whose excited-state wavefunctions overlap, resulting in the formation of bound dimers in the excited state. The fact that the ground-state wavefunctions of excimers do not overlap results in efficient CT from the higher-energy donor constituent to the lower-energy acceptor constituent. This gives rise to the characteristic emissions from both constituents, which in turn results in a broad luminescence spectrum. ET or CT transitions can arise in *Donor-Acceptor* (D-A) structures in which the wavefunction of higher-energy donor emitter overlaps with that of the lower energy acceptor emitter. This overlap should be sufficient for ET or CT to occur, but small enough to prevent quenching of the donor. ESIPT describes the picosecond-scale proton transfer from an excited-state H-donor to an H-acceptor through the intramolecular hydrogen bond. This transfer results from the tautomerisation of an emitter molecule from an enol to a keto form, such that the excited molecule exhibits the fluorescence peaks of both constituents. This particular approach is relevant to the work presented in this Chapter, and will be revisited in Section 4.3.3.

4.2 Characterising white light emitters

In the previous section, we highlighted the value of developing novel single-species white light emitters, and reviewed some interesting strategies by which this can be done. We now consider the features of single-species white light emitters that are important for their implementation into WOLED devices. Three of the most important characteristics of a WOLED are its quantum efficiency, its lifetime, and its emission colour. Although the fabrication of WOLED devices is beyond the scope of this thesis, it is important to take these characteristics into consideration when designing new materials for use as potential WOLED emitters. For this reason, we briefly address all three of these key factors in this section.

The quantum efficiency of an OLED device can be assessed in terms of its *Internal Quantum Efficiency* (IQE) or its *External Quantum Efficiency* (EQE). The IQE is measured as the number of photons generated within the device per electron-hole pair injected, while the EQE is the number of photons emitted from the device per electron-hole pair injected. The EQE therefore also takes into account the outcoupling efficiency of the device. For fluorescence-based emitters, like the one addressed in this thesis, we therefore highlight that having a high PLQY is very important.

The lifetime of a device is defined by the number of operational hours it can withstand before its intensity drops to 50%. One of the greatest advantages of LEDs over traditional light sources like incandescent bulbs is their extended (around ten times longer) operational lifetimes. Since OLEDs still suffer from very short lifetimes with respect to inorganic LEDs, white light emitter stability is a crucial factor to consider.

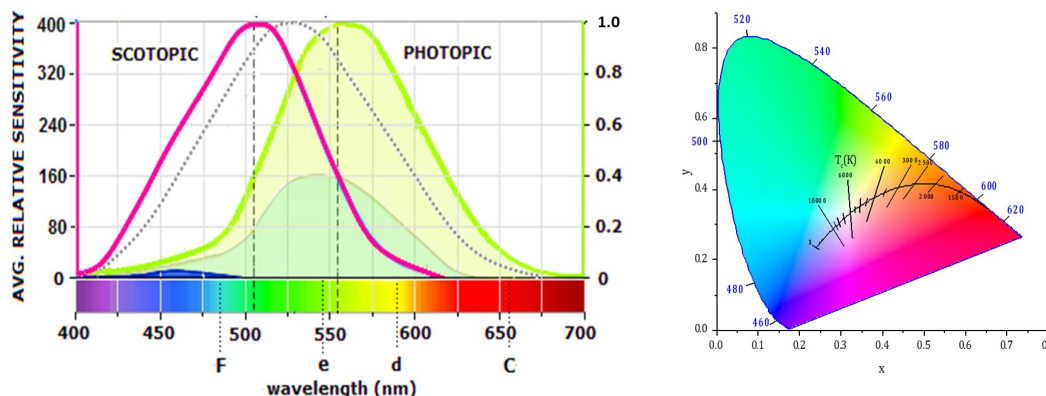


Figure 4.2 – Characterising the colour of white light. The spectral sensitivity of the human eye under bright (photopic) and dim (scotopic) conditions (left) is taken into consideration when converting a photoluminescence spectrum into its corresponding coordinates on a CIE diagram (right).

Control over the colour white light obtained from an emitter is important because it would allow the realisation of purpose-built lighting for a range of environments spanning homes, offices, hospitals, and more. The colour of light emitted by a molecule is evaluated by converting its photoluminescence spectrum into a set of coordinates that can be mapped onto a chromaticity diagram like the one in Figure 4.2. Due its complex anatomy, the colour of light that is perceived by the human eye is not the same as the colour emitted by a source. This is because our retinal cone cells, which are responsible for colour perception of vision in high-intensity (*i.e.* ‘photopic’) conditions, are more sensitive to light of certain wavelengths. The conversion of a photoluminescence spectrum into the chromaticity coordinates defined by the *International Commission on Illumination* (CIE) as the CIE 1931 colour space takes into account the peaks of spectral sensitivity associated with the cone cells. The spectrum is weighted by individual spectral sensitivities so as to render an objective value corresponding to the perceived colour of the light source. The spectral response of the eye under photopic and scotopic (*i.e.* bright and low-light respectively) conditions is given in Figure 4.2 on the right, while the CIE 1931 colour map is shown on the left. The coordinates corresponding to ideal, pure white light are found at the

center of the CIE 1931 colour map, with values of (0.33, 0.33). A light source with these CIE coordinates has a colour that most closely resembles that of natural sunlight. It is therefore the ultimate goal in terms of the colour of a white light emitter.

We mentioned in Section 4.1 that the colour obtained from WOLEDs can be challenging to control. In the following section, we report the unique strategy that we adopted to synthesise a novel, single-species white light emitter with tuneable the emission colour.

4.3 A Bio-inspired, Single-species, White-light Emitter

The previous sections highlight the challenges of realising single-species white-light emitters that exhibit spectral and environmental stability, as well as high photoluminescence quantum yields. In the following sections, we describe our exploration of a novel approach to this problem, inspired by bioluminescence seen in fireflies and click beetles (Figure 4.3a). Using this bioluminescence-inspired strategy, we designed an OMIM that allows us to exploit the photochemical properties of LH_2 . Adjusting the solvent composition in the void spaces of the crystallised OMIM tunes the emitted colour, with the optimum composition giving nearly perfect white light. This solvent-based tuneability in a rigid metal complex gives us amongst the highest photoluminescence quantum yields reported for a single-species white-light emitter. Further, it mimics colour changes observed in different organisms, allowing our results to suggest a molecular mechanism that explains these phenomena.

4.3.1 Luminescence of D-Luciferin

Fireflies, click beetles, and railroad worms, like those seen in Figure 4.3a, are remarkable organisms that emit yellow, green, and red light respectively, all using the identical bioluminescent substrate, D-Luciferin (LH_2). Although the mechanism underlying the different emission colours of these different creatures is still under debate by biologists, the existence of LH_2 as a chemically unbound species within protein matrices in organisms has made it possible to probe its photochemical properties extensively.

Studies of LH_2 and derivative molecules reveal high quantum yields and colour tuneability, whereby the colour of light emitted can be varied by altering its chemical environment, as illustrated in Figure 4.3b or by introducing changes in its structure, as shown in Figure 4.3c.

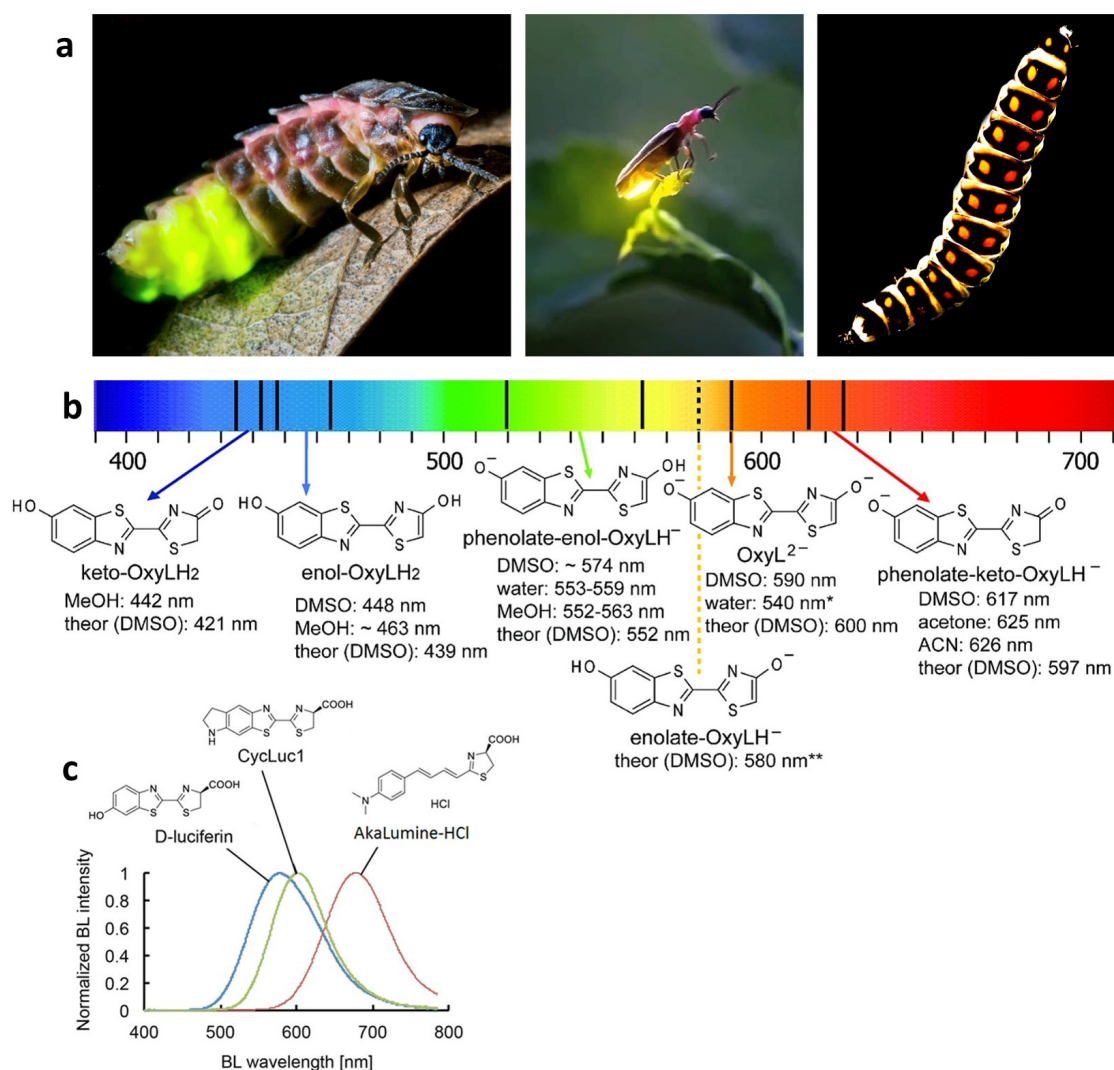


Figure 4.3 – Bioluminescence in beetles. **a.** Photographs of green-emitting bioluminescent fireflies and a red-emitting bioluminescent railroad worm. **b.** Changes in optical spectra of the LH₂-based bioluminescent molecule in different solvents arise from changes in the protonation states of its terminal groups [128], **c.** Structurally modified derivatives of luciferin exhibit different fluorescence emission peaks [129].

For example, increasing π - π overlap between the thiazole and benzothiazole heterocycles, as shown in Figure 4.3c, can shift the position of the emission peak well into the red [130,131]. Alternatively, the emission of a given structural analogue will undergo spectral shifts triggered simply by changes in the microenvironment surrounding the terminal groups of its thiazole/benzothiazole fragments [128,132,133]. Such microenvironment phenomena underlie the elegant colour tuning mechanism observed in-vivo. While no generally-accepted theory exists to fully explain the origin of bioluminescence colour

tuning, the conformation of the surrounding protein matrix [134], as well as residues in the immediate environment of the luciferin molecule [135], have been shown to impact the emitted light colour.

In the following section, we demonstrate how both structural and microenvironment-triggered tuneability can be exploited to harness the photochemical properties of LH₂ in solid-state synthetic complexes, which we named Cu₂L₃. To achieve this, copper ions are used to fuse LH₂ molecules into stable molecular complexes that crystallise in such a way as to exhibit extrinsic porosity in the form of voids. Importantly, the colour-tuning terminal groups of the ligands in these complexes face the void spaces that are present in the crystallised material. Similar to those in some naturally-occurring protein-complexed LH₂ systems, these terminal groups are then free to interact with their surrounding environment, thus introducing the emission colour tuneability into the solid state.

4.3.2 Synthesis and Structure of Cu₂L₃

The synthesis of Cu₂L₃ is carried out by reacting D-LH₂ with Cu(NO₃)₂ · 2.5H₂O at 373 K in an appropriate ratio in a H₂O/DMF/EtOH solution. The reagents are introduced into borosilicate glass scintillation vials, which are then sealed and heated for 16 hours, resulting in the formation of relatively insoluble reddish-brown crystals of Cu₂L₃, like those in Figure 4.4a, at a 70% yield. During the synthesis, the D-LH₂ precursor partially reduces some of the Cu²⁺ to Cu¹⁺, while simultaneously being oxidized to its planar aromatic 2-(6'-hydroxy-2'-benzothiazolyl)-thiazole-4-carboxylic acid (dehydroluciferin, L) form, which is shown in 4.4b. The oxidation of LH₂ to form L removes the chirality of the ligand precursor. Cu₂L₃ thus crystallises in the triclinic centrosymmetric space group P $\bar{1}$ with one metal complex present in the asymmetric unit. Each metal complex of Cu₂L₃, shown in Figure 4.4c, is composed of three L molecules acting as ligands linked by two Cu ions. Cu1 links L1 to L2 via coordination bonds to the L1 3N, L1 4-COO, L2 3S, and L2 3'N. Bridging of L2 3S, and L2 3'N by Cu2 fixes the C2-C2' bond, presumably contributing to the enhanced photoluminescence quantum yield of the Cu₂L₃ complex with respect to the free ligand. Cu2 links L2 to L3 via the 3N and 4-COO groups of both ligands. Both Cu1 and Cu2 display distorted tetrahedral coordination geometries, with Cu1 in the 1+ oxidation state and Cu2 in the 2+ oxidation state.

To confirm the assignment of Cu1 and Cu2 oxidation states, the presence of Cu¹⁺ and Cu²⁺ in the crystal structure was confirmed by *X-ray Photoelectron Spectroscopy* (XPS).

XPS measurements confirmed the presence of Cu^{1+} and Cu^{2+} in a 1:1 ratio. Fitting of the Cu $2p_{3/2}$ line (Figure 4.4c) shows two components with similar integrals, at binding energies of 932.5 eV and 934.4 eV, which are assigned to Cu^{1+} and Cu^{2+} respectively. Since a binding energy of 933 eV may typically correspond to either Cu^{1+} or Cu^0 , assignment of the 932.5 eV peak to Cu^{1+} rather than Cu^0 was further verified by Auger transitions (Figure 4.4e). Cu LMM transitions are similar (916 eV) in Cu^{2+} and Cu^{1+} , but higher in energy (918 eV) in Cu^0 . The presence of a single peak at 916 eV in the Cu LMM line of Cu_2L_3 confirms the absence of Cu^0 in the complex. XPS data thus confirm that Cu_2L_3 contains about 50% Cu^{2+} and 50% Cu^{1+} .

Both Cu ions form coordinate bonds with the N atoms of all three thiazole rings, as well as with the O atoms of all the ligand terminal carboxylate groups. Cu1 additionally bridges the thiazole and benzothiazole fragments of the central ligand via the S and N atoms. The 6'-OH hydroxyl terminals of the ligands, with their ground-state pK_a [136] of 8, remain protonated during synthesis and do not take part in coordination to the Cu ions. Despite the ligands of Cu_2L_3 being planar, the coordination geometries of Cu1 and Cu2 impose an overall zigzag shape on the metal complex, with the outer ligands rotated 90 degrees with respect to the central ligand. This awkward shape results in an inefficient but regular crystal packing (Figure 4.5), characteristic of OMIMs. These materials are extrinsically porous by definition, as the inefficient crystal packing produces regular void spaces. In the case of Cu_2L_3 , the void spaces account for 13.1% of the unit-cell volume, and when crystallised, manifest as 1D channels that extend along the c axis (Figure 4.5b, c). Crystallinity of the as-synthesized complex was confirmed by *Powder X-Ray Diffraction* (PXRD) (Figure 4.5d). *Scanning Electron Microscopy* (SEM) and *Energy-Dispersive X-ray Spectroscopy* (EDX) images (Figure 4.5e, f) of Cu_2L_3 show the flat, rectangular shape of the copper-rich crystals.

Two particularly notable structural aspects of Cu_2L_3 are the planar, aromatic form of the thiazole fragments, and the void-facing positions of the photoacidic 6'-OH terminals (Figure 4.5b, c). The enol form of LH_2 , in which blue and green emissions arise, also has a planar aromatic thiazole fragment. In biological systems such as the *L. cruciata* firefly, this form is said to be stabilised by the short ($<2 \text{ \AA}$) distance between the N3 of the emitter and an O of a proximate phosphate in the surrounding protein. Comparable bond lengths are present between the N3 and Cu centres of Cu_2L_3 (Figure 4.4c). Stabilisation of the thiazole heterocycle in a single form allows greater control over the optical properties of the overall complex, by excluding the effects of potential

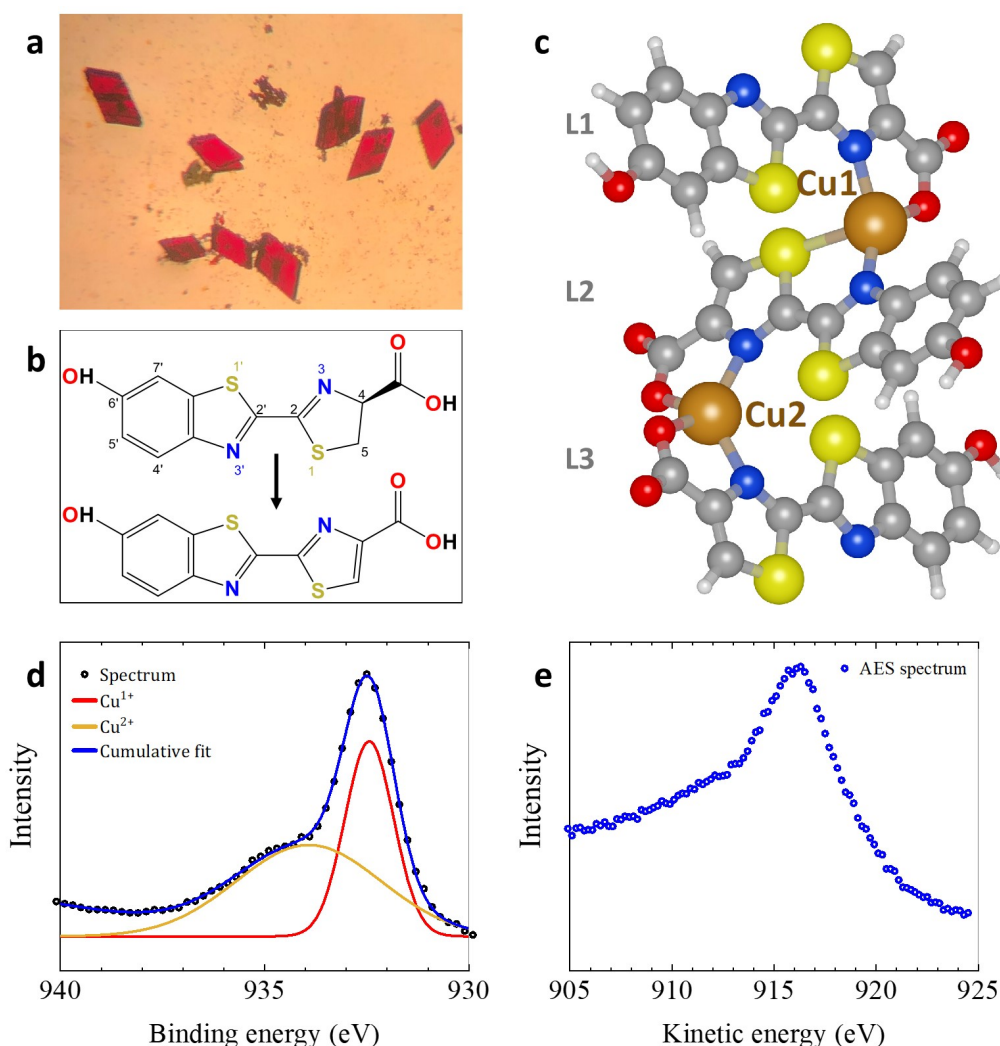


Figure 4.4 – The Cu_2L_3 complex. **a.** Optical microscope image of Cu_2L_3 crystals, **b.** (top) LH_2 transforms into dehydroluciferin (L, bottom) by means of an oxidizing agent (Cu^{2+}). The atom numbering scheme is indicated for LH_2 , **c.** Asymmetric unit of Cu_2L_3 consisting of three L units bridged by two Cu ions. Atom colour scheme: C = gray, H = white, O = red, N = blue, S = yellow. **d.** Cu 2p XPS spectrum of as-synthesised Cu_2L_3 , **e.** The presence of a single peak at 916 eV in the kinetic energy spectrum of CuLMM transition in Cu_2L_3 confirms the absence of Cu^0 in the material.

tautomerization. Void-facing positions of the unbound 6'-OH terminals, on the other hand, give the voids a synthetic binding pocket-like feature. Similar to the biological binding pocket, adsorption of different guest molecules affects the photochemistry of the complex due to interactions with its 6'-OH terminals. This is important because deprotonation of the 6'-OH terminals has been shown to play a key role in redshifting the colour emitted by LH_2 -like molecules [137].

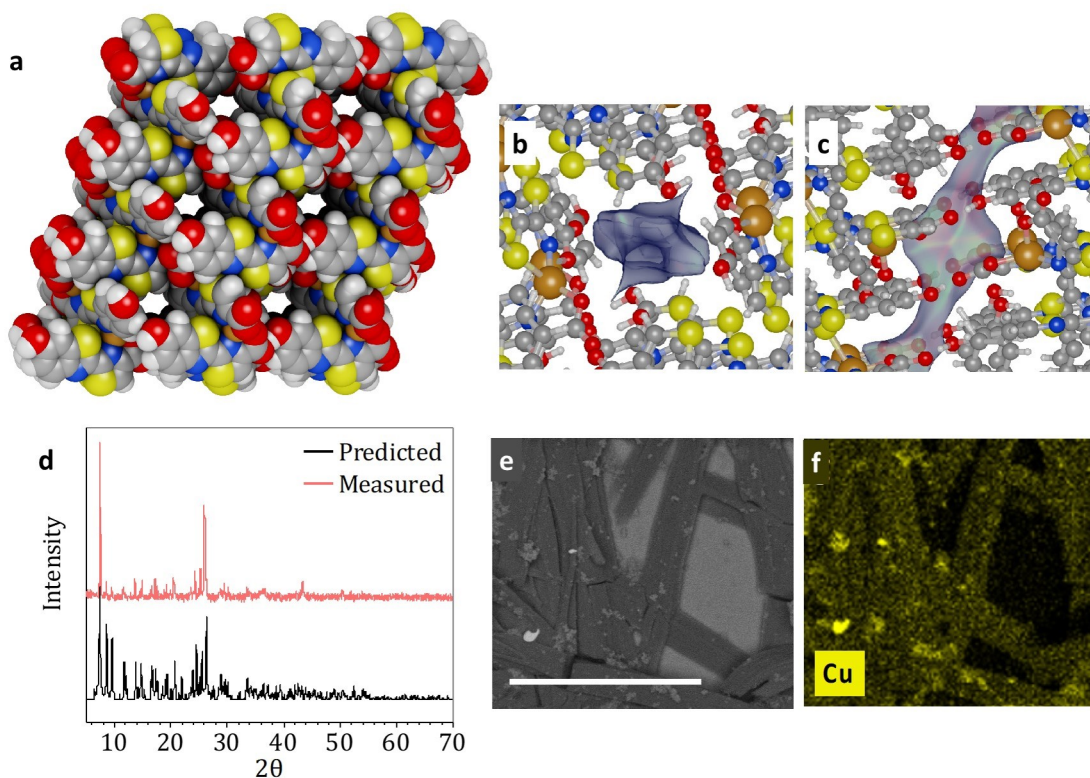


Figure 4.5 – Crystal structure of Cu_2L_3 . **a.** Spacefill model of Cu_2L_3 shows 1D channels in the c-axis direction. **b,c.** Views of internal surfaces of the channels in the crystal highlight the accessibility of ligand terminal groups to the channels. Atom colour scheme: C = gray, H = white, O = red, N = blue, S = yellow. **d.** Predicted and measured PXRD patterns of as-made Cu_2L_3 , **e,f** SEM image, and corresponding Cu EDX spectrum of as-synthesised Cu_2L_3 . Scale bar corresponds to 10 μm .

4.3.3 Optical Properties of Cu_2L_3

The UV-visible absorption spectrum of Cu_2L_3 follows a similar profile to that of the free ligand L (Figure 4.6a), with a narrow absorption band at 340 nm corresponding to $\pi\text{-}\pi^*$ transitions localised in each of the three ligands, L1, L2, and L3. The longer-wavelength shoulder is attributed to weak *Metal-to-Ligand Charge Transfer* (MLCT) transitions directed primarily to the central ligand, L2, whose thiazole S (S3) and benzothiazole N (N3) are both coordinated to Cu1. When excited at 350 nm, as-synthesised crystals of Cu_2L_3 show a broad photoluminescence spectrum consisting of three distinct contributions; a blue peak centred at 430 nm, a green-yellow 550 nm peak, and a red shoulder at 630 nm (Figure 4.6b). The emissive deexcitations that give rise to the 430 nm and 550 nm main peaks are ascribed to intraligand contributions. The ligand precursor, D-LH₂, as well

as its derivative molecules, are strong photoacids with well-investigated photochemical properties. Typically, neutral LH₂-like molecules emit in the blue region. Deprotonation of the 6'-OH group, which results in the anionic phenolate form of the molecule, is known to lower the emission energy, resulting to a characteristic 100 nm redshift. The 430 nm and 550 nm peaks in Cu₂L₃ are therefore attributed to the complexed ligands in their neutral and anionic (6'-O⁻) forms, respectively. Dispersions of Cu₂L₃ in a range of non-aqueous solvents, including ethanol, exhibit only the 430 nm phenol signature peak in their emission spectra, (Figure 4.6b), indicating full protonation of the benzothiazole terminals. In pure water and aqueous buffers of pH 9 and 4, only the 550 nm phenolate emission is present, indicating complete deprotonation of the benzothiazole terminals. Notably, the effect of pH on the protonation state of the phenol terminals is negligible compared to that of H₂O, which we assign to the low pK_a of these terminals in the excited state, as confirmed by dominance of the 6'-O⁻ characteristic peak at pH 4.

To confirm the assignment of optical absorption and emission peaks, *Density Functional Theory* (DFT) was used to calculate the molecular orbitals associated with photoexcited transitions in Cu₂L₃ (Figure 4.6c). These calculations confirm that the optical properties of Cu₂L₃ are ligand-based, and correspond to the sum of individual transitions localised on each ligand comprising the asymmetric unit. Since the Cu₂L₃ complex is charge-neutral, appearance of the 550 nm 6'-O⁻ signature peak in the spectrum is attributed to the strong photoacidity of the void-facing 6'-OH terminals, whereby photoexcitation lowers their pK_a [138] from 8 to -0.5. This means that proximate guest water molecules present in the synthetic binding pockets of the complex promote partial deprotonation of the photoexcited 6'-OH* via fast *Excited-State Proton Transfer* (ESPT) with the environment.

A common strategy in bioluminescence engineering is to modify LH₂-like molecules in order to obtain different emission colours. Our results therefore suggest that introducing modifications to the ligand precursors used can extend the range of emission colours obtainable from Cu₂L₃-like materials. To illustrate this point, we used DFT calculations to identify two LH₂-based modified ligands that could form isostructural complexes of Cu₂L₃ and predicted the positions of their 6'-OH and 6'-O⁻ emission peaks. The hypothetical modified ligands, shown in Figure 4.7 include Se-L, in which the thiazole S3 is substituted by Se, and N-L, in which the benzene ring of the benzothiazole fragment is substituted by naphthalene. The predicted emission peaks are redshifted with respect to Cu₂L₃, and they confirm the possibility of achieving further tuneability using such

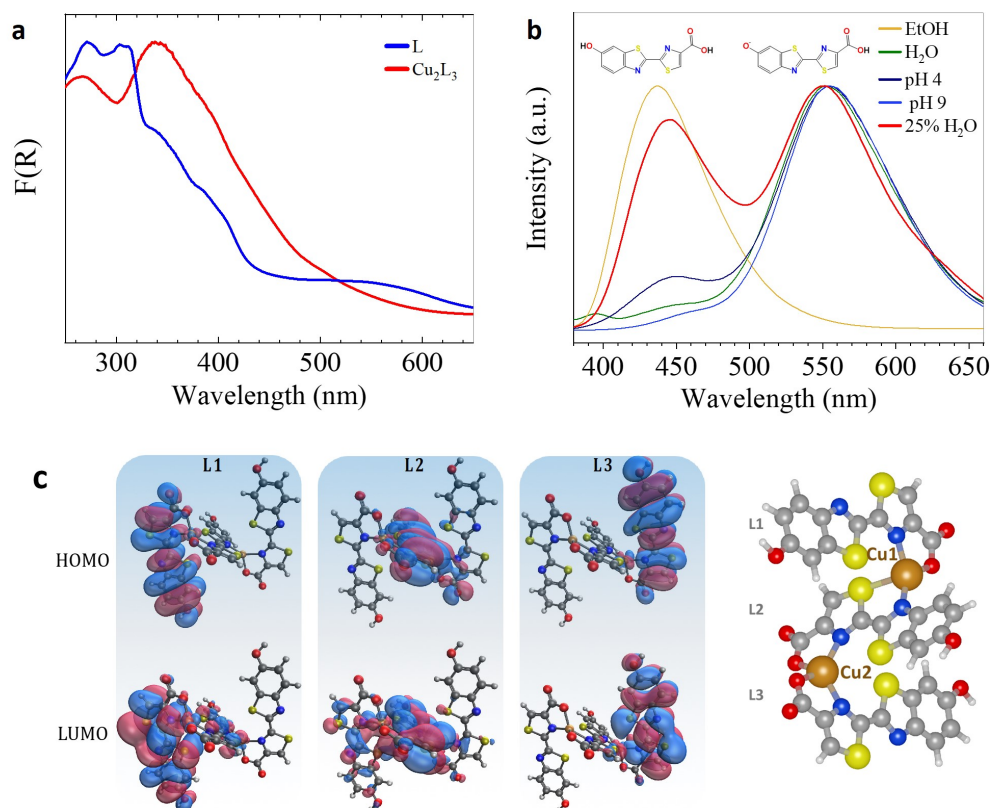


Figure 4.6 – Optical properties of Cu_2L_3 . **a.** Kubelka-Munk ($F(R)$) diffuse reflectance spectrum of the free ligand L and Cu_2L_3 , **b.** Photoluminescence spectrum of as-synthesised Cu_2L_3 excited at 350 nm (red line), and the crystals suspended in different solvents, **c.** Molecular orbitals associated with the three main excitations contributing to the absorption band of Cu_2L_3 .

materials.

For a given structure, we can achieve a further fine tuning of the colour by changing the composition of the solvent in the void space. For example, immersion of the insoluble crystals in pure ethanol or pure water indicate the emission colour due to fully protonated or fully deprotonated OH groups respectively. This suggests that loading the pores with mixtures of water and ethanol in varying ratios will give rise to the simultaneous appearance of both 6'-OH and 6'-O⁻ peaks in varying intensities. Indeed, by decreasing the ethanol concentration, we observe that the emission coordinates of the crystals follow the white region of the CIE map from cool to warm (Figure 4.8a. and b.), closely crossing the coordinates for ideal white light. The change in emission colour upon introduction of water in increasing concentrations can be seen in the photograph in Figure 4.8c. The

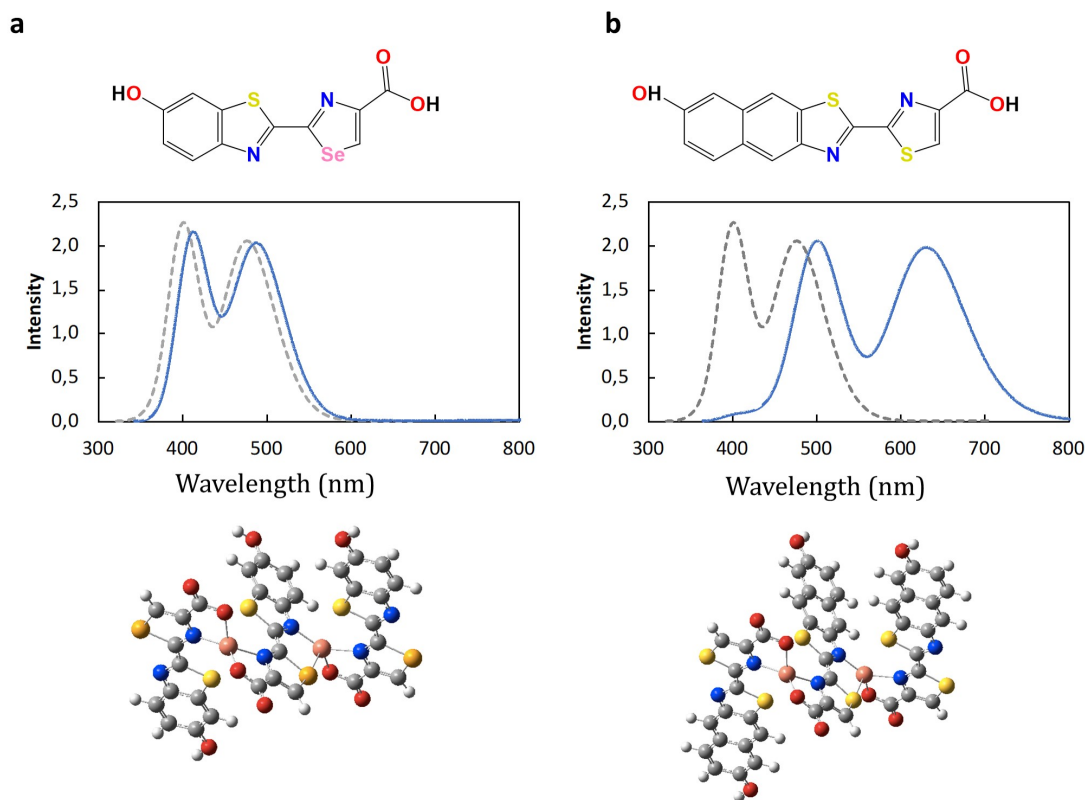


Figure 4.7 – Structure and emission of predicted Cu_2L_3 -like complexes. **a.** Computed geometry and emission spectra (blue lines) of Cu_2L_3 complex with Se-substituted L ligands and **b.** naphthalene L. The computed emission spectra of Cu_2L_3 is also given for comparison (grey dotted lines). Both protonated and deprotonated forms of 6'-OH are considered. A width of 0.3 eV was used in the spectra representation.

emission spectrum of Cu_2L_3 crystals in 25% water is significantly broad (FWHM = 182.1 nm), and consists of the 450 and 550 nm peaks in a 0.75:1.00 intensity ratio, along with the 630 nm shoulder (Figure 4.8a, red line). This corresponds to nearly pure-white CIE coordinates of (0.29, 0.33) (Figure 4.8b, red circle). The PLQY is 57%; amongst the highest reported for a single-species white light emitter, and to the best of our knowledge, the highest quantum yield of an emitter closest to the equal energy point of the CIE map. We attribute the high PLQY to rigidity and low rotational and vibrational losses in the complex, due to the ligand C2-C2', OH, and COOH bonds being locked in position by the Cu centres. Stability of the material in air and water is demonstrated via PXRD measurements of the complex after three months in air, and after soaking in a H_2O -EtOH 0.25:0.75 mixture overnight (Figure 4.8d). The realisation of an electroluminescent device lies beyond the scope of this thesis, however, the results obtained show promise for the use of Cu_2L_3 in tunable broad-spectrum lighting. While it is possible that charge

injection may lead to the oxidation of Cu^{1+} to Cu^{2+} , this has not been explored, and the material itself in the conditions we have exposed it to can be used as a bright, spectrally- and chemically-stable phosphor. As our material relies neither on toxic chemicals nor rare metals, it holds promise for widespread use in relatively cheap light emitting devices.

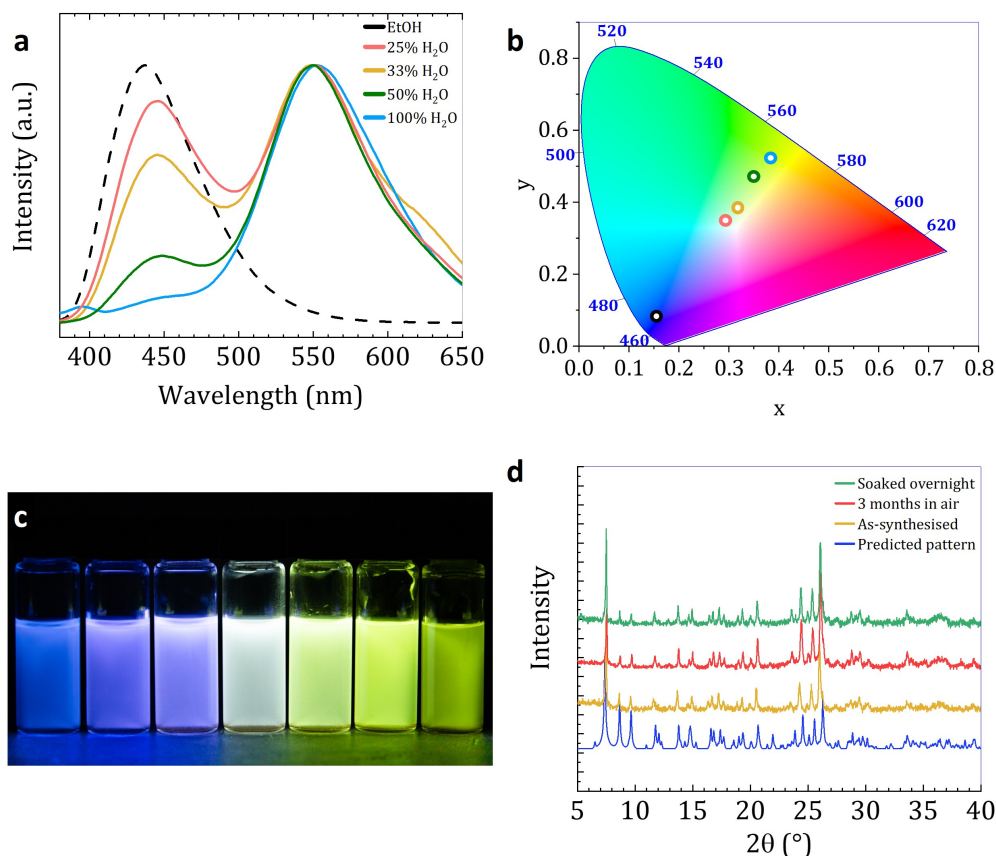


Figure 4.8 – Tuneable luminescence spectrum of Cu_2L_3 . **a.** Dependence of photoluminescence spectrum (normalised to the 550 nm peak) on the concentration of H_2O in the pores of Cu_2L_3 , and **b.** Corresponding emission colours. Black and blue circles/dashed lines correspond to signature $6'-\text{OH}$ and $6'-\text{O}^-$ spectra seen in pure ethanol and pure water, respectively. CIE coordinates of Cu_2L_3 synthesised in 25% H_2O (red circle) are (0.29, 0.33). Photoluminescence spectrum of Cu_2L_3 excited at 350 nm (blue line). A Gaussian deconvolution of the spectrum gives peaks positioned at 430 nm (cyan line), 550 nm (green line) and 630 nm (red line). The black dashed line corresponds to the overall fitting of the emission spectrum, **c.** Photograph of Cu_2L_3 crystals suspended in solvent mixtures with varying amounts of water, from the left, 0, 5, 15, 25, 50, 75, and 100%. **d.** Stability of Cu_2L_3 in air and in aqueous solutions is demonstrated via PXRD patterns of the material as-synthesised, after three months in open air, and after soaking overnight in an aqueous ethanol solution.

To gain insights into the behaviour of water molecules in the synthetic binding pocket of

Cu_2L_3 Monte Carlo (MC) simulations were carried out for different solvent concentrations. Figure 4.9a, shows the adsorption sites of oxygen molecules from guest molecules such as ethanol and water within the pores of Cu_2L_3 . One of the preferential binding sites for water lies next to the 6'-OH groups, and is labelled site 1. Upon addition of ethanol into the pores, the ethanol molecules show a stronger binding at this particular site, and displace the water molecules, which makes it increasingly difficult for the 6'-OH to deprotonate. This effect is seen in Figure 4.9b, which shows that a consequence of increasing the concentration of ethanol in the Cu_2L_3 environment, the probability of finding a water molecule next to the 6'-O site decreases. It is worth noting that according to the calculations, while the probability of finding a water molecule at site 1 decreases upon addition of ethanol, the probability of finding a water molecule at site 2 simultaneously increases. This supports the hypothesis that water molecules are pushed away from the site 1 in the presence of ethanol, giving fewer 6'-OH sites access to deprotonation, and shifting the relative intensities of the two characteristic peaks.

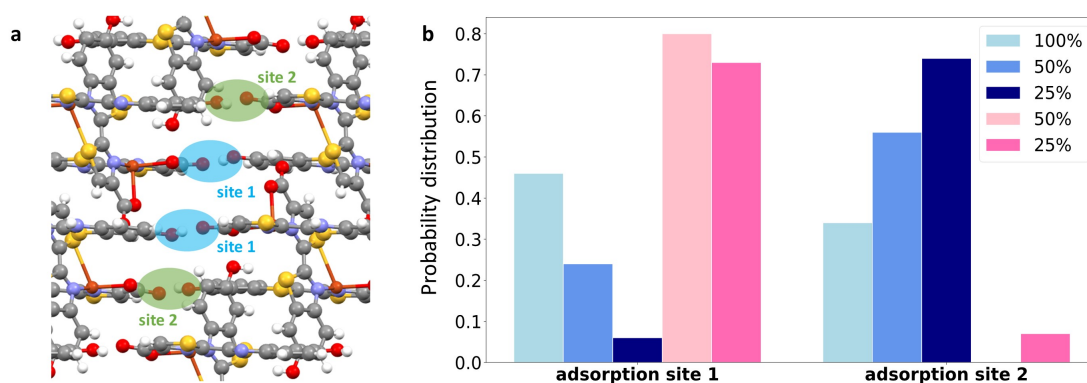


Figure 4.9 – Solvent adsorption sites and probability density plots computed in the 3x3x2 supercell of DFT optimized Cu_2L_3 at 298.15 K and 0.02 bar. a adsorption sites 1 and two are marked in blue and green, respectively. **b** Probability distribution of the oxygen atoms from water and ethanol molecules at the adsorption sites 1 and 2. Percentages in the legend represent water compositions. Blue and pink colors represent water and ethanol, respectively.

4.3.4 Cu_2L_3 as a Molecular Model for luciferin@luciferase Complexes

Luciferase/luciferin pairs are extensively investigated for use in bioimaging and analysis applications [130]. Near- and far infra-red emitting systems in particular are of interest for in vivo bioimaging of haemoglobin-rich or high-density tissue such as bones. These applications drive the search for an understanding of bioluminescence colour tuning

mechanisms. Such an understanding will help guide the design of luciferase/luciferin variants that support high quantum yield bioluminescence well into the red.

Investigations of luciferase variants have unveiled a range of factors that may contribute to determining the bioluminescence emission colour. The most commonly proposed factors include tautomerization of keto (red-emitting) and enol (green-emitting) forms of the thiazole fragment in luciferin [139], non-specific solvent interaction effects [140], interactions between residues of the luciferase enzyme [141], and the confirmation of the active site [134, 142]. While the community has yet to converge on a hypothesis that explains precisely how the emitted colour is determined, recent studies have provided substantial mechanistic clues. For example, it was found that both green and red bioluminescence can be observed when the keto-like 5,5'-dimethyl-oxyluciferin (dimethoxyluciferin), which cannot undergo tautomerism, is used as a substrate [143]. Subsequent experimental and theoretical studies have served to dispute the impact of tautomerization within the luciferase binding site [137]. Residue interactions, conformation of the active site, and solvent interactions with the 6'-OH group can then be considered to play significant roles in determining whether the emission is green or red.

In-depth studies into the effects of site-directed mutations on a range of luciferase variants have shed light on the complex interplay between different factors present in bioluminescent systems. For example, even substitutions of randomly-distributed residues, distant from the luciferase binding site, have resulted in changes of the bioluminescence emission colour [144], possibly due to effect of inter-residue interactions on the conformation and/or chemical environment of the binding site [140]. Studies have shown that changes in the binding site conformation, whereby it takes on a more 'open' configuration, result in redshifting of the luminescence [134]. This redshift has been attributed to the open-form microenvironment allowing excited oxyluciferin to rotate about its C2-C2' bond, thus lowering the energy of its radiative deexcitation. Several examples reported in the literature demonstrate that enlarging of the binding site or its surrounding cavity also result in redshifted emissions [135]. Besides geometric relaxation, an alternative hypothesis to explain this tendency points to the effect of solvent interactions. Recent comprehensive structural studies of pH-sensitive and pH-insensitive luciferases suggest that increased accessibility of solvent molecules to the luciferase binding site result in red emissions. Interestingly, these studies also suggest that the 6'-OH group of oxyluciferin lies close to the luciferase binding site region that is responsible for colour determination [145]. Within this region of the binding site, potential non-specific solvent effects that can result

in redshifted emissions include changes in pH, the concentration of metal ions, or the concentration water molecules.

By proposing Cu_2L_3 and similar porous crystals as molecular models for bioluminescence colour tuning, we are able to disentangle and separately investigate the different contributing factors currently under debate, and thus potentially contribute to the design of application-specific luciferases. In Cu_2L_3 , the thiazole rings are fixed in a planar aromatic ('enol-like') structure, and the COOH terminals, which take part in coordination, are unavailable to interact with the pore environment. Rigidity of the packed structure prevents rotation about the C2-C2' bond, eliminating effects of geometry relaxation on the radiative deexcitation energy. Access of the 6'-OH groups of all three ligands in the asymmetric unit of Cu_2L_3 allows us to monitor the impact of the pore environment on the emission wavelength, without any other structural or chemical modifications.

Key structural similarities between the ligands in Cu_2L_3 , crystallised oxyluciferin, and AMP-complexed oxyluciferin in the *Luciola cruciata* binding site support the use of Cu_2L_3 as a molecular model. Binding of the thiazole N3 to Cu in all three ligands of Cu_2L_3 is comparable to N3-O binding to a 6'-OH in crystallised oxyluciferin, and to a proximate water molecule in AMP-complexed luciferin of the *L. cruciata* species. N3-Cu bond lengths in Cu_2L_3 range from 1.927 Å to 1.983 Å, while in both, crystallised oxyluciferin and LH2@*L. cruciata* the N-O bonds range from 2.782 Å to 2.878 Å. Similarities between Cu_2L_3 the luciferin molecule in the protein environment were quantified by performing similarity analyses between the structure of Cu_2L_3 and the Oxy-LH₂ molecule embedded in the protein scaffold (PDB 2D1T27). As seen in Figure 4.10, the geometry of Cu_2L_3 (red) agrees perfectly (RMS < 0.067 Å) with the crystal structure of Oxy-LH₂ reported by Naumov et al (blue). In the protein scaffold, the thiazole half of the benzothiazole ring can $\pi - \pi$ interact with the phenyl ring from Phe249, which is at a distance of 4.16 Å. In our compound, we find a stacking distance of approximately 3.7 Å, and similar to Naumov et al. we observe that the dimers are offset to each other. We also find a similar packing fraction of 0.12 as in the crystal of enol-Oxy-LH₂ (0.11).

Simulations were used to visualize the interface of Cu_2L_3 with the environment, and draw comparisons with the natural luciferin@luciferase system. In particular the water adsorption surfaces of and luciferin in the protein pocket were calculated at 298 K. These adsorption surfaces, shown in blue in Figure 4.11, clearly show that, similar to the structure embedded in the protein, the phenolic OH can form all hydrogen bonding active functional groups most strongly interact with water. Similar water coordination

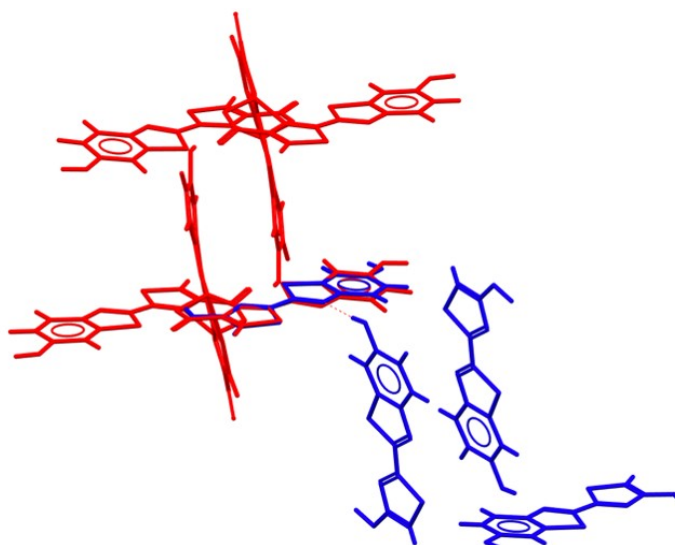


Figure 4.10 – Comparison of Cu_2L_3 to crystallised oxyluciferin. Crystal structure of crystallised oxyluciferin illustrates the comparable intraligand interactions in Cu_2L_3 , oxyluciferin and *L. cruciata* luciferin@luciferase structures.

environments were found in GCMC simulations. According to the simulations, the maximum of the distribution of distances of the oxygen of the water molecule to oxygen the phenolic OH group is 3.3 Å, which is close to the distances of 2.73 Å and 3.3 Å that are found in the protein.

By locking the solvent-emitter interactions into a simplified synthetic binding pocket with a comparable chemical environment to that of both crystallised oxyluciferin and the luciferase protein pocket, we are able to more closely observe the drastic effect of water molecules on emission spectra. Simply changing the protonation state of the 6'-OH by introducing water into the surrounding pocket is sufficient to change colour. Conformational changes, in addition to the nature of the residue, may impact the water content, and hence the protonation state of the 6'-OH group in luciferin. This rationalises why such diverse hypotheses have been put forward; all directly or indirectly influence the water molecules in the binding pocket, and hence colour-determining chemical interactions taking place in vivo.

4.4 Conclusions

In this Chapter, we summarised the challenges in WOLED technology, and proposed a novel strategy that may contribute to filling some of the existing gaps. Inspired by

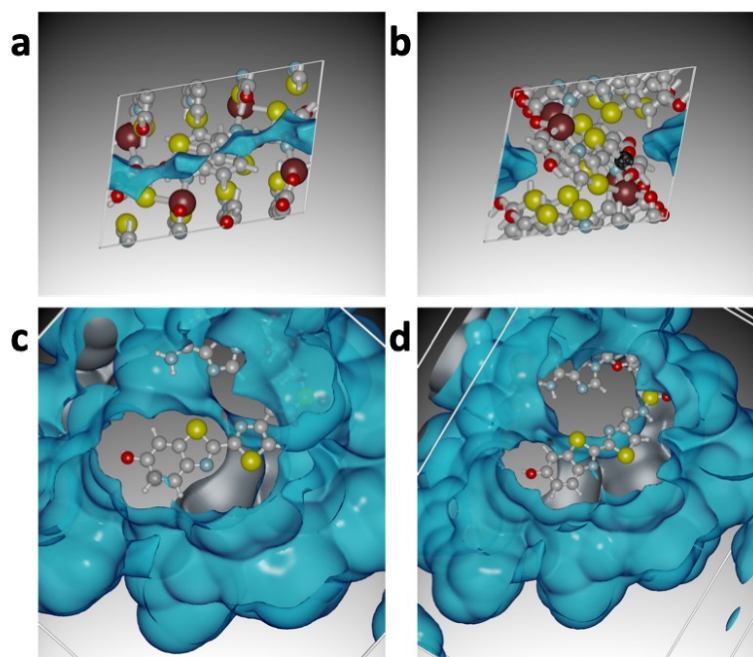


Figure 4.11 – Comparison of water adsorption in Cu_2L_3 and luciferase pocket. **a,b.** Water adsorption surface in Cu_2L_3 **c,d.** water adsorption surface of the ATP bound molecule in the SLU pocket of the protein. For visual clarity, we omit the amino acids that form the protein pocket in subfigures c and d but they are considered for the calculation of the adsorption surface.

the variety of emission colours that can be observed in bioluminescent organisms, we synthesised a porous, crystalline material using a bioluminescent molecule. Exploiting the properties of this molecule, we obtain a single-species white-light emitter whose emission is not only broad but also tuneable. The tuneability arises due to ESIPT processes occurring when water molecules are present in the pores of the material. By changing the amount of water used in the synthesis, we can easily control the colour of light that is emitted. Our material is stable and can be synthesised using inexpensive reagents, under low-temperature conditions. In addition, by forming a rigid complex using copper ions, we were able to achieve a PLQY of 57%, which is currently the highest value of quantum yield reported for a white-light emitter.

Since the reason why different bioluminescent organisms emit different colours is still under debate by biologists, we were intrigued to explore whether the tuneability observed in the pores of our structure offer any insights. We found that treating our material as a molecular model for the in-vivo protein system, we are able to isolate the significant impact of water molecules within the protein pocket.

5

Conclusions and Future Perspectives

This thesis was focused on the design and discovery of new luminescent, porous, crystalline materials for targeted applications. As we have worked towards design of materials for specific applications, we have paid careful attention to consider the potential of our work for practical implementation. However, there is an even more important theme that underlies the work presented in this thesis; rather than focusing on how to find a solution for one specific problem at a time, we aimed to find and propose strategies for material design that may be generalised and applied to a range of problems.

Working with modular porous crystals like *Metal-Organic Frameworks* (MOFs) and *Organic Molecules of Intrinsic Microporosity* (OMIMs), we were able to explore an extensive landscape of ways to incorporate desirable properties into our materials, such as stability, high *Photoluminescence Quantum Yield* (PLQY), and chemical functionality. In Chapter 1, we provided a general introduction that highlights the various aspects of MOFs and OMIMs that make them the powerful sub-class of materials they are. Chapter 2 details the photoluminescence properties of such materials, and the associated phenomena that occur in their structures. In particular, we highlighted how the combined properties of modularity, crystallinity, and porosity can give rise to unique optical phenomena. The principles outlined in the first two chapters of this thesis were considered in the tailored design of new materials.

Despite their promising properties, such materials are challenging to implement into real-world applications. For example, while the number of unique MOF structures that have been reported is in the range of several tens of thousands, they have yet to evolve into commercially and industrially viable materials. Addressing some of the most common challenges, such as limited stability, low synthetic yields, or poor processability, will help bridge the gap between the laboratory and the real world to bring these materials

closer to practical use. The outcome of this work has been two new materials developed for two different applications, each of which perform highly in comparison with their recently-reported contenders, while possessing unique properties that allow them to function in interesting ways. For both materials, we have considered practical aspects such as stability, the use of relatively inexpensive reagents, or the means by which they may be used in practice. The first, presented in Chapter 3, is a MOF for quantitatively sensing fluoride ions in the trace levels (<2 *parts per million* (ppm)) at which they can be toxic in drinking water. Unlike other F^- sensing materials, our MOF, named ‘Sion-105’, binds with its target analyte via electrostatic interactions, and yet manages to selectively target F^- , even in the presence of other small anionic interferences. The reason for this is the shape of the MOF ligand, which contains the active site for F^- binding. With its bulky sidegroups, once locked in as part of the rigid MOF net, the ligand rotates into a propeller-like structure that allows only F^- to access the active site. In addition, the sensitivity of Sion-105 to F^- is among the highest reported in literature for the same application. In Chapter 4, we present a second material with unique properties; an OMIM that we created for white light emission. The broad-spectrum light emission arises from the organic component of this OMIM, which consists of a bioluminescent molecule called luciferin. The metal nodes, made of Cu^{1+} and Cu^{2+} ions, do not contribute to the emission colour of the complex, however by locking the luciferin molecules into a rigid structure, they enhance the intensity of light emitted. As a result, we were able to obtain a material with the highest thus-far reported value of PLQY for a single-species white light emitter. Not only is our OMIM a highly efficient white light emitter, it also possesses unique pore environment that allow its emission colour to be easily tuned by changing the amount of water used in its synthesis.

5.1 Future Perspectives

It has been a key aspect over the course of this thesis to try and find creative new approaches to materials design that may easily be generalised beyond a single application. As such, we foresee interesting opportunities to expand both projects.

The Sion-105 project addresses the detection of fluoride, a chemical contaminant that is common in ground water, safe to consume in very small quantities, but highly toxic if trace levels are consumed over prolonged periods. Since fluoride-contaminated water is safe to use for washing and bathing, and fluoride ions are relatively easy and cheap to

extract from water, the key challenge lies in being able to test a water source and identify whether it is safe to drink from, or needs to be filtered. Another chemical contaminant that is also safe to use but not consume, and is commonly found in ground water, is arsenic. The toxicity of both these contaminants is most strikingly manifested itself in the remote desert villages of countries like India and Pakistan, where people have limited or no access to test facilities. The Sion-105 portable device presented in this thesis offers a possible solution. As an immediate future goal, we envision the development of a new MOF with lanthanide-based luminescence, similar to Sion-105, whose linker is designed for the targeted detection of arsenic. By employing green-emitting Terbium, we may be able to achieve similar quantitative detection using green light. We would then be able to tweak the Sion-105 portable device, introducing a new photodiode and filter, to obtain a single handheld instrument to simultaneously quantify the presence of both contaminants in a single water sample.

The Cu_2L_3 project offers an alternative, bioluminescence-inspired approach to obtaining tuneable, high-PLQY, white-light emission. In addition to the favourable optical properties, the porous structure served as an interesting molecular model to investigate what chemical processes might be occurring within bioluminescent cells to cause the different emission colours of different organisms. We are interested in further extending both aspects of this study. First, we envision the synthesis of new, modified luciferins to synthesise new OMIM structures for light emission applications. In particular, we would like to investigate how much of the *International Commission on Illumination* (CIE) colour space we can access by synthesising new luciferin-based porous crystals. We have filed to patent this strategy. Given that each crystal will have different pore geometries and unique internal chemical environments, we can continue to investigate how small changes in the structure of luciferin's in-vivo protein pocket might be influencing the bioluminescence colour.

Overall, we continue to explore new prospects in the world of MOFs, OMIMs, and other molecular materials, with curiosity and an open mind. This work presents an infinitesimal window into the many possibilities.

Bibliography

- [1] Angelo Kirchon, Liang Feng, Hannah F Drake, Elizabeth A Joseph, and Hong-Cai Zhou. From fundamentals to applications: a toolbox for robust and multifunctional mof materials. *Chemical Society Reviews*, 47(23):8611–8638, 2018.
- [2] James R Holst, Abbie Trewin, and Andrew I Cooper. Porous organic molecules. *Nature chemistry*, 2(11):915–920, 2010.
- [3] AI Cooper and ACS Cent. Sci. 2017, 3, 544:[pmc free article][pubmed][google scholar] b) hasell t., cooper ai. *Nat. Rev. Mater*, 1:16053, 2016.
- [4] Seham Ebrahim, Tomoki Fujita, Bryan A Millis, Elliott Kozin, Xuefei Ma, Sachiyo Kawamoto, Michelle A Baird, Michael Davidson, Shigenobu Yonemura, Yasuo Hisa, et al. Nmii forms a contractile transcellular sarcomeric network to regulate apical cell junctions and tissue geometry. *Current Biology*, 23(8):731–736, 2013.
- [5] Metasebya Solomon, Kevin Guo, Gail P Sudlow, Mikhail Y Berezin, W Barry Edwards, Samuel Achilefu, and Walter J Akers. Detection of enzyme activity in orthotopic murine breast cancer by fluorescence lifetime imaging using a fluorescence resonance energy transfer-based molecular probe. *Journal of biomedical optics*, 16(6):066019, 2011.
- [6] DC Agrawal, Harvey S Leff, and VJ Menon. Efficiency and efficacy of incandescent lamps. *American Journal of Physics*, 64(5):649–654, 1996.
- [7] Lisa Guan, Trevor Berrill, and Richard J Brown. Measurement of actual efficacy of compact fluorescent lamps (cfls). *Energy and Buildings*, 86:601–607, 2015.
- [8] Hiroshi Amano, Masahiro Kito, Kazumasa Hiramatsu, and Isamu Akasaki. P-type conduction in mg-doped gan treated with low-energy electron beam irradiation (leebi). *Japanese Journal of Applied Physics*, 28(12A):L2112, 1989.

- [9] Isamu Akasaki, Hiroshi Amano, Masahiro Kito, and Kazumasa Hiramatsu. Photoluminescence of mg-doped p-type gan and electroluminescence of gan pn junction led. *Journal of luminescence*, 48:666–670, 1991.
- [10] Shuji Nakamura, Takashi Mukai, and Masayuki Senoh. Candela-class high-brightness ingan/algan double-heterostructure blue-light-emitting diodes. *Applied Physics Letters*, 64(13):1687–1689, 1994.
- [11] Nabeela Khan and N Abas. Comparative study of energy saving light sources. *Renewable and sustainable energy reviews*, 15(1):296–309, 2011.
- [12] Paul Waide. Phase out of incandescent lamps. *OECD Publications*, 5, 2010.
- [13] Rajagopal Vadivambal and Digvir S Jayas. *Bio-imaging: principles, techniques, and applications*. CRC Press, 2015.
- [14] Otto S Wolfbeis. An overview of nanoparticles commonly used in fluorescent bioimaging. *Chemical Society Reviews*, 44(14):4743–4768, 2015.
- [15] Jia-Xing Jiang, Abbie Trewin, Dave J Adams, and Andrew I Cooper. Band gap engineering in fluorescent conjugated microporous polymers. *Chemical Science*, 2(9):1777–1781, 2011.
- [16] Abhijit Patra and Ullrich Scherf. Fluorescent microporous organic polymers: Potential testbed for optical applications. *Chemistry–A European Journal*, 18(33):10074–10080, 2012.
- [17] Yuanjing Cui, Banglin Chen, and Guodong Qian. Lanthanide metal-organic frameworks for luminescent sensing and light-emitting applications. *Coordination Chemistry Reviews*, 273:76–86, 2014.
- [18] MD Allendorf, CA Bauer, RK Bhakta, and RJT Houk. Luminescent metal-organic frameworks. *Chemical Society Reviews*, 38(5):1330–1352, 2009.
- [19] Zhichao Hu, Benjamin J Deibert, and Jing Li. Luminescent metal-organic frameworks for chemical sensing and explosive detection. *Chemical Society Reviews*, 43(16):5815–5840, 2014.
- [20] Huai-Song Wang. Metal-organic frameworks for biosensing and bioimaging applications. *Coordination Chemistry Reviews*, 349:139–155, 2017.

-
- [21] Teng Zhang and Wenbin Lin. Metal–organic frameworks for artificial photosynthesis and photocatalysis. *Chemical Society Reviews*, 43(16):5982–5993, 2014.
- [22] Stavroula Kampouri and Kyriakos C Stylianou. Dual-functional photocatalysis for simultaneous hydrogen production and oxidation of organic substances. *ACS Catalysis*, 9(5):4247–4270, 2019.
- [23] Tu N Nguyen, Fatmah Mish Ebrahim, and Kyriakos C Stylianou. Photoluminescent, upconversion luminescent and nonlinear optical metal-organic frameworks: From fundamental photophysics to potential applications. *Coordination Chemistry Reviews*, 377:259–306, 2018.
- [24] H Mo Powell. 15. the structure of molecular compounds. part iv. clathrate compounds. *Journal of the Chemical Society (Resumed)*, pages 61–73, 1948.
- [25] Yukio Kinoshita, Ikuo Matsubara, and Yoshihiko Saito. The crystal structure of bis (succinonitrilo) copper (i) nitrate. *Bulletin of the Chemical Society of Japan*, 32(7):741–747, 1959.
- [26] STEPHEN J Maginn. Crystal engineering: the design of organic solids by gr desiraju, 1991.
- [27] Michael J Zaworotko. Crystal engineering of diamondoid networks. *Chemical Society Reviews*, 23(4):283–288, 1994.
- [28] Omar M Yaghi, Guangming Li, and Hailian Li. Selective binding and removal of guests in a microporous metal–organic framework. *Nature*, 378(6558):703–706, 1995.
- [29] Omar M Yaghi, Michael O’Keeffe, Nathan W Ockwig, Hee K Chae, Mohamed Eddaoudi, and Jaheon Kim. Reticular synthesis and the design of new materials. *Nature*, 423(6941):705–714, 2003.
- [30] Hailian Li, Mohamed Eddaoudi, Thomas L Groy, and OM Yaghi. Establishing microporosity in open metal- organic frameworks: gas sorption isotherms for zn (bdc)(bdc= 1, 4-benzenedicarboxylate). *Journal of the American Chemical Society*, 120(33):8571–8572, 1998.
- [31] Mohamed Eddaoudi, Jaheon Kim, Nathaniel Rosi, David Vodak, Joseph Wachter, Michael O’Keeffe, and Omar M Yaghi. Systematic design of pore size and functionality in isorecticular mofs and their application in methane storage. *Science*, 295(5554):469–472, 2002.

- [32] Gérard Férey, Christian Serre, Caroline Mellot-Draznieks, Franck Millange, Suzy Surblé, Julien Dutour, and Irène Margiolaki. A hybrid solid with giant pores prepared by a combination of targeted chemistry, simulation, and powder diffraction. *Angewandte Chemie International Edition*, 43(46):6296–6301, 2004.
- [33] Laura Mitchell, Berenice Gonzalez-Santiago, John PS Mowat, Mary E Gunn, Patrick Williamson, Nadia Acerbi, Matthew L Clarke, and Paul A Wright. Remarkable lewis acid catalytic performance of the scandium trimesate metal organic framework mil-100 (sc) for c–c and c [double bond, length as m-dash] n bond-forming reactions. *Catalysis Science & Technology*, 3(3):606–617, 2013.
- [34] Javier Castells-Gil, Natalia M Padial, Neyvis Almora-Barrios, Iván Da Silva, Diego Mateo, Josep Albero, Hermenegildo García, and Carlos Martí-Gastaldo. De novo synthesis of mesoporous photoactive titanium (iv)–organic frameworks with mil-100 topology. *Chemical science*, 10(15):4313–4321, 2019.
- [35] Hiroyasu Furukawa, Kyle E Cordova, Michael O’Keeffe, and Omar M Yaghi. The chemistry and applications of metal-organic frameworks. *Science*, 341(6149):1230444, 2013.
- [36] Jacklyn N Hall and Praveen Bollini. Structure, characterization, and catalytic properties of open-metal sites in metal organic frameworks. *Reaction Chemistry & Engineering*, 4(2):207–222, 2019.
- [37] Hong Ki Kim, Won Seok Yun, Min-Bum Kim, Jeung Yoon Kim, Youn-Sang Bae, JaeDong Lee, and Nak Cheon Jeong. A chemical route to activation of open metal sites in the copper-based metal–organic framework materials hkust-1 and cu-mof-2. *Journal of the American Chemical Society*, 137(31):10009–10015, 2015.
- [38] Sheng Ye, Xin Jiang, Lin-Wei Ruan, Bei Liu, Yi-Min Wang, Jun-Fa Zhu, and Ling-Guang Qiu. Post-combustion co₂ capture with the hkust-1 and mil-101 (cr) metal–organic frameworks: Adsorption, separation and regeneration investigations. *Microporous and Mesoporous Materials*, 179:191–197, 2013.
- [39] Barbara Supronowicz, Andreas Mavrandonakis, and Thomas Heine. Interaction of small gases with the unsaturated metal centers of the hkust-1 metal organic framework. *The Journal of Physical Chemistry C*, 117(28):14570–14578, 2013.
- [40] Youn-Sang Bae, Chang Yeon Lee, Ki Chul Kim, Omar K Farha, Peter Nickias, Joseph T Hupp, SonBinh T Nguyen, and Randall Q Snurr. High propene/propane

- selectivity in isostructural metal–organic frameworks with high densities of open metal sites. *Angewandte Chemie International Edition*, 51(8):1857–1860, 2012.
- [41] Liyong Yuan, Ming Tian, Jianhui Lan, Xingzhong Cao, Xiaolin Wang, Zhifang Chai, John K Gibson, and Weiqun Shi. Defect engineering in metal–organic frameworks: a new strategy to develop applicable actinide sorbents. *Chemical communications*, 54(4):370–373, 2018.
- [42] Hui Wu, Yong Shen Chua, Vaiva Krungleviciute, Madhusudan Tyagi, Ping Chen, Taner Yildirim, and Wei Zhou. Unusual and highly tunable missing-linker defects in zirconium metal–organic framework uio-66 and their important effects on gas adsorption. *Journal of the American Chemical Society*, 135(28):10525–10532, 2013.
- [43] Lingmei Liu, Zhijie Chen, Jianjian Wang, Daliang Zhang, Yihan Zhu, Sanliang Ling, Kuo-Wei Huang, Youssef Belmabkhout, Karim Adil, Yuxin Zhang, et al. Imaging defects and their evolution in a metal–organic framework at sub-unit-cell resolution. *Nature chemistry*, 11(7):622–628, 2019.
- [44] Michael Mastalerz and Iris M Oppel. Rational construction of an extrinsic porous molecular crystal with an extraordinary high specific surface area. *Angewandte Chemie International Edition*, 51(21):5252–5255, 2012.
- [45] Rupert GD Taylor, C Grazia Bezzu, Mariolino Carta, Kadhum J Msayib, Jonathan Walker, Rhys Short, Benson M Kariuki, and Neil B McKeown. The synthesis of organic molecules of intrinsic microporosity designed to frustrate efficient molecular packing. *Chemistry—A European Journal*, 22(7):2466–2472, 2016.
- [46] Ephraim Prantl, Bernd Kohl, Dimitrij Ryvlin, Philipp Biegger, Hubert Wadepohl, Frank Rominger, Uwe HF Bunz, Michael Mastalerz, and Siegfried R Waldvogel. Microporous triptycene-based affinity materials on quartz crystal microbalances for tracing of illicit compounds. *ChemPlusChem*, 84(9):1239–1244, 2019.
- [47] Hemendra Kumar Sen-Gupta. Xliv.—condensation of ketones with phenols. part i. condensation with α -naphthol. *Journal of the Chemical Society, Transactions*, 105:399–409, 1914.
- [48] Wilson Baker, AJ Floyd, JFW McOmie, G Pope, AS Weaving, and JH Wild. 394. condensation products of phenols and ketones. part x. the structure of dianin’s compounds, a unique inclusion-forming substance. *Journal of the Chemical Society (Resumed)*, pages 2010–2017, 1956.

- [49] Richard M Barrer and Vivien H Shanson. Dianin's compound as a zeolitic sorbent. *Journal of the Chemical Society, Chemical Communications*, 9:333–334, 1976.
- [50] Neil B. McKeown. Nanoporous molecular crystals. *J. Mater. Chem.*, 20:10588–10597, 2010.
- [51] Shan Jiang, John Bacsá, Xiaofeng Wu, James TA Jones, Robert Dawson, Abbie Trewin, Dave J Adams, and Andrew I Cooper. Selective gas sorption in a [2+3]‘propeller’cage crystal. *Chemical Communications*, 47(31):8919–8921, 2011.
- [52] Rupert GD Taylor, Mariolino Carta, C Grazia Bezzu, Jonathan Walker, Kadhum J Msayib, Benson M Kariuki, and Neil B McKeown. Triptycene-based organic molecules of intrinsic microporosity. *Organic letters*, 16(7):1848–1851, 2014.
- [53] Kadhum J Msayib, David Book, Peter M Budd, Nhamo Chaukura, Kenneth DM Harris, Madeleine Helliwell, Steven Tedds, Allan Walton, John E Warren, Mingcan Xu, et al. Nitrogen and hydrogen adsorption by an organic microporous crystal. *Angewandte Chemie International Edition*, 48(18):3273–3277, 2009.
- [54] Aleksander Jablonski. Efficiency of anti-stokes fluorescence in dyes. *Nature*, 131(3319):839–840, 1933.
- [55] Jean-Luc Bredas. Mind the gap! *Materials Horizons*, 1(1):17–19, 2014.
- [56] Gift Mehlana and Susan A Bourne. Unravelling chromism in metal–organic frameworks. *CrystEngComm*, 19(30):4238–4259, 2017.
- [57] Norman S Allen. *Photochemistry and photophysics of polymeric materials*. John Wiley & Sons, 2010.
- [58] Michael E Foster, Jason D Azoulay, Bryan M Wong, and Mark D Allendorf. Novel metal–organic framework linkers for light harvesting applications. *Chemical Science*, 5(5):2081–2090, 2014.
- [59] Pekka Hänninen and Harri Härmä. *Lanthanide luminescence: photophysical, analytical and biological aspects*, volume 7. Springer Science & Business Media, 2011.
- [60] JG Santaclara, F Kapteijn, J Gascon, and MA Van Der Veen. Understanding metal–organic frameworks for photocatalytic solar fuel production. *CrystEngComm*, 19(29):4118–4125, 2017.

-
- [61] Silvia Bordiga, Carlo Lamberti, Gabriele Ricchiardi, Laura Regli, F Bonino, A Damin, K-P Lillerud, M Bjorgen, and Adriano Zecchina. Electronic and vibrational properties of a mof-5 metal–organic framework: Zno quantum dot behaviour. *Chemical communications*, 20:2300–2301, 2004.
- [62] Lina Li, Shuquan Zhang, Liangjin Xu, Liang Han, Zhong-Ning Chen, and Junhua Luo. An intensely luminescent metal–organic framework based on a highly light-harvesting dicyclo-metallated iridium (iii) unit showing effective detection of explosives. *Inorganic chemistry*, 52(21):12323–12325, 2013.
- [63] SP McGlynn, FJ Smith, and G Cilento. Some aspects of the triplet. *Photochemistry and Photobiology*, 3(4):269–294, 1964.
- [64] Lu Zhai, Wen-Wei Zhang, Jing-Lin Zuo, and Xiao-Ming Ren. Simultaneous observation of ligand-based fluorescence and phosphorescence within a magnesium-based cp/mof at room temperature. *Dalton Transactions*, 45(30):11935–11938, 2016.
- [65] Joseph R Lakowicz. *Principles of fluorescence spectroscopy*. Springer Science & Business Media, 2013.
- [66] Monica C So, Gary P Wiederrecht, Joseph E Mondloch, Joseph T Hupp, and Omar K Farha. Metal–organic framework materials for light-harvesting and energy transfer. *Chemical Communications*, 51(17):3501–3510, 2015.
- [67] Tanya N Singh-Rachford and Felix N Castellano. Photon upconversion based on sensitized triplet–triplet annihilation. *Coordination Chemistry Reviews*, 254(21-22):2560–2573, 2010.
- [68] Markus Pollnau, Daniel R Gamelin, SR Lüthi, HU Güdel, and Markus P Hehlen. Power dependence of upconversion luminescence in lanthanide and transition-metal ion systems. *Physical Review B*, 61(5):3337, 2000.
- [69] David C Mayer, Aurora Manzi, Raghavender Medishetty, Benedikt Winkler, Christian Schneider, Gregor Kieslich, Alexander Pothig, Jochen Feldmann, and Roland A Fischer. Controlling multiphoton absorption efficiency by chromophore packing in metal–organic frameworks. *Journal of the American Chemical Society*, 141(29):11594–11602, 2019.

- [70] Chen Wang, Li Tian, Wei Zhu, Shiqiang Wang, Peng Wang, Yun Liang, Wanlin Zhang, Hongwei Zhao, and Guangtao Li. Dye@ bio-mof-1 composite as a dual-emitting platform for enhanced detection of a wide range of explosive molecules. *ACS applied materials & interfaces*, 9(23):20076–20085, 2017.
- [71] NI Nijegorodov and WS Downey. The influence of planarity and rigidity on the absorption and fluorescence parameters and intersystem crossing rate constant in aromatic molecules. *The Journal of Physical Chemistry*, 98(22):5639–5643, 1994.
- [72] Yuanjing Cui, Yanfeng Yue, Guodong Qian, and Banglin Chen. Luminescent functional metal–organic frameworks. *Chemical reviews*, 112(2):1126–1162, 2012.
- [73] Beatrice Alpha, Roberto Ballardini, Vincenzo Balzani, Jean-Marie Lehn, Siglinda Perathoner, and Nanda Sabbatini. Antenna effect in luminescent lanthanide cryptates: a photophysical study. *Photochemistry and photobiology*, 52(2):299–306, 1990.
- [74] James H Nobbs. Kubelka—munk theory and the prediction of reflectance. *Review of Progress in Coloration and Related Topics*, 15(1):66–75, 1985.
- [75] Fang Tian, Karolyn M Hansen, Thomas L Ferrell, Thomas Thundat, and Douglas C Hansen. Dynamic microcantilever sensors for discerning biomolecular interactions. *Analytical Chemistry*, 77(6):1601–1606, 2005.
- [76] Hans Peter Lang and Christoph Gerber. Microcantilever sensors. In *STM and AFM studies on (bio) molecular systems: unravelling the nanoworld*, pages 1–27. Springer, 2008.
- [77] Yildiz Uludağ, Sergey A Piletsky, Anthony PF Turner, and Matthew A Cooper. Piezoelectric sensors based on molecular imprinted polymers for detection of low molecular mass analytes. *The FEBS journal*, 274(21):5471–5480, 2007.
- [78] Changyong Yim, Moonchan Lee, Wuseok Kim, Sanghee Lee, Gook-Hee Kim, Kyong Tae Kim, and Sangmin Jeon. Adsorption and desorption characteristics of alcohol vapors on a nanoporous zif-8 film investigated using silicon microcantilevers. *Chemical Communications*, 51(28):6168–6171, 2015.
- [79] Changyong Yim, Moonchan Lee, Minhyuk Yun, Gook-Hee Kim, Kyong Tae Kim, and Sangmin Jeon. Co 2-selective nanoporous metal-organic framework microcantilevers. *Scientific reports*, 5(1):1–8, 2015.

-
- [80] Ivo Stassen, Nicholas Burtch, Alec Talin, Paolo Falcaro, Mark Allendorf, and Rob Ameloot. An updated roadmap for the integration of metal–organic frameworks with electronic devices and chemical sensors. *Chemical Society Reviews*, 46(11):3185–3241, 2017.
- [81] Jiri Janata. Potentiometric microsensors. *Chemical Reviews*, 90(5):691–703, 1990.
- [82] P Davydovskaya, V Pentyala, O Yurchenko, L Hussein, R Pohle, and GA Urban. Work function based sensing of alkanes and alcohols with benzene tricarboxylate linked metal organic frameworks. *Sensors and Actuators B: Chemical*, 193:911–917, 2014.
- [83] Camille Petit, Barbara Mendoza, and Teresa J Bandosz. Reactive adsorption of ammonia on cu-based mof/graphene composites. *Langmuir*, 26(19):15302–15309, 2010.
- [84] Colette McDonagh, Conor S Burke, and Brian D MacCraith. Optical chemical sensors. *Chemical reviews*, 108(2):400–422, 2008.
- [85] William P Lustig, Soumya Mukherjee, Nathan D Rudd, Aamod V Desai, Jing Li, and Sujit K Ghosh. Metal–organic frameworks: functional luminescent and photonic materials for sensing applications. *Chemical Society Reviews*, 46(11):3242–3285, 2017.
- [86] Denise Zacher, Osama Shekhah, Christof Wöll, and Roland A Fischer. Thin films of metal–organic frameworks. *Chemical Society Reviews*, 38(5):1418–1429, 2009.
- [87] Mostafa MH Khalil, Ahmed Shahat, Ahmed Radwan, and MF El-Shahat. Colorimetric determination of cu (ii) ions in biological samples using metal-organic framework as scaffold. *Sensors and Actuators B: Chemical*, 233:272–280, 2016.
- [88] Andrzej Gładysiak, Tu N Nguyen, Jorge AR Navarro, Matthew J Rosseinsky, and Kyriakos C Stylianou. A recyclable metal–organic framework as a dual detector and adsorbent for ammonia. *Chemistry–A European Journal*, 23(55):13602–13606, 2017.
- [89] Yingmu Zhang, Shuai Yuan, Gregory Day, Xuan Wang, Xinyu Yang, and Hong-Cai Zhou. Luminescent sensors based on metal-organic frameworks. *Coordination Chemistry Reviews*, 354:28–45, 2018.

- [90] Xian Fang, Boyang Zong, and Shun Mao. Metal–organic framework-based sensors for environmental contaminant sensing. *Nano-micro letters*, 10(4):64, 2018.
- [91] Wanbin Li, Yufan Zhang, Congyang Zhang, Qin Meng, Zehai Xu, Pengcheng Su, Qingbiao Li, Chong Shen, Zheng Fan, Lei Qin, et al. Transformation of metal-organic frameworks for molecular sieving membranes. *Nature communications*, 7(1):1–9, 2016.
- [92] John DB Featherstone. Prevention and reversal of dental caries: role of low level fluoride. *Community dentistry and oral epidemiology*, 27(1):31–40, 1999.
- [93] PK DenBesten and H Thariani. Biological mechanisms of fluorosis and level and timing of systemic exposure to fluoride with respect to fluorosis. *Journal of dental research*, 71(5):1238–1243, 1992.
- [94] Marie-Laure Cittanova, Brigitte Lelongt, Marie-Christine Verpont, Monique Geniteau-Legendre, Fayez Wahbe, Dominique Prie, Pierre Coriat, and Pierre M Ronco. Fluoride ion toxicity in human kidney collecting duct cells. *Anesthesiology: The Journal of the American Society of Anesthesiologists*, 84(2):428–435, 1996.
- [95] Piler Mahaboob Basha, Puja Rai, and Shabana Begum. Fluoride toxicity and status of serum thyroid hormones, brain histopathology, and learning memory in rats: a multigenerational assessment. *Biological trace element research*, 144(1-3):1083–1094, 2011.
- [96] Zohreh Kheradpisheh, Masoud Mirzaei, Amir Hossein Mahvi, Mehdi Mokhtari, Reyhane Azizi, Hossein Fallahzadeh, and Mohammad Hassan Ehrampoush. Impact of drinking water fluoride on human thyroid hormones: a case-control study. *Scientific reports*, 8(1):2674, 2018.
- [97] Yi-Guo Long, Ya-Nan Wang, Jia Chen, Su-Fen Jiang, Agneta Nordberg, and Zhi-Zhong Guan. Chronic fluoride toxicity decreases the number of nicotinic acetylcholine receptors in rat brain. *Neurotoxicology and teratology*, 24(6):751–757, 2002.
- [98] Olivier Barbier, Laura Arreola-Mendoza, and Luz María Del Razo. Molecular mechanisms of fluoride toxicity. *Chemico-biological interactions*, 188(2):319–333, 2010.
- [99] Surendra Roy and Gurcharan Dass. Fluoride contamination in drinking water—a review. *Resour. Environ*, 3(3):53–58, 2013.

-
- [100] Binglin Sui, Bosung Kim, Yuanwei Zhang, Andrew Frazer, and Kevin D Belfield. Highly selective fluorescence turn-on sensor for fluoride detection. *ACS applied materials & interfaces*, 5(8):2920–2923, 2013.
- [101] Zhong-Rui Yang, Man-Man Wang, Xue-Sheng Wang, and Xue-Bo Yin. Boric-acid-functional lanthanide metal–organic frameworks for selective ratiometric fluorescence detection of fluoride ions. *Analytical chemistry*, 89(3):1930–1936, 2017.
- [102] Ying Zhou, Jun Feng Zhang, and Juyoung Yoon. Fluorescence and colorimetric chemosensors for fluoride-ion detection. *Chemical reviews*, 114(10):5511–5571, 2014.
- [103] Florian M Hinterholzinger, Bastian Rühle, Stefan Wuttke, Konstantin Karaghiosoff, and Thomas Bein. Highly sensitive and selective fluoride detection in water through fluorophore release from a metal-organic framework. *Scientific reports*, 3:2562, 2013.
- [104] Rui Hu, Jiao Feng, Dehui Hu, Shuangqing Wang, Shayu Li, Yi Li, and Guoqiang Yang. A rapid aqueous fluoride ion sensor with dual output modes. *Angewandte Chemie International Edition*, 49(29):4915–4918, 2010.
- [105] Eun Jin Cho, Byung Ju Ryu, Young Ju Lee, and Kye Chun Nam. Visible colorimetric fluoride ion sensors. *Organic letters*, 7(13):2607–2609, 2005.
- [106] Casey R Wade, Alexander EJ Broomsgrove, Simon Aldridge, and Francois P Gabbai. Fluoride ion complexation and sensing using organoboron compounds. *Chemical reviews*, 110(7):3958–3984, 2010.
- [107] Joel Keizer. Nonlinear fluorescence quenching and the origin of positive curvature in stern-volmer plots. *Journal of the American Chemical Society*, 105(6):1494–1498, 1983.
- [108] Bernard Valeur. Molecular fluorescence. *digital Encyclopedia of Applied Physics*, pages 477–531, 2003.
- [109] Hualing Zeng and Gilles Durocher. Analysis of fluorescence quenching in some antioxidants from non-linear stern—volmer plots. *Journal of luminescence*, 63(1-2):75–84, 1995.
- [110] Banglin Chen, Liangbo Wang, Fatima Zapata, Guodong Qian, and Emil B Lobkovsky. A luminescent microporous metal- organic framework for the recognition

- and sensing of anions. *Journal of the American Chemical Society*, 130(21):6718–6719, 2008.
- [111] Ling Chen, Jia-Wen Ye, Hai-Ping Wang, Mei Pan, Shao-Yun Yin, Zhang-Wen Wei, Lu-Yin Zhang, Kai Wu, Ya-Nan Fan, and Cheng-Yong Su. Ultrafast water sensing and thermal imaging by a metal-organic framework with switchable luminescence. *Nature communications*, 8:15985, 2017.
- [112] C Subramani, S Surya, J Gowtham, Rahul Chari, S Srinivasan, JP Siddharth, and Hemant Shrimali. Energy efficiency and pay-back calculation on street lighting systems. In *AIP Conference Proceedings*, volume 2112, page 020082. AIP Publishing LLC, 2019.
- [113] Ir Dr Sam CM Hui. Lighting energy management. 2017.
- [114] David F Motta Cabrera and Hamidreza Zareipour. Data association mining for identifying lighting energy waste patterns in educational institutes. *Energy and Buildings*, 62:210–216, 2013.
- [115] Bianca Blum, Julian Hübner, Adrian Milde, and Karl Justus Bernhard Neumärker. On the evidence of rebound effects in the lighting sector: Implications for promoting led lighting. Technical report, The Constitutional Economics Network Working Papers, 2018.
- [116] Christian Branas, Francisco J Azcondo, and J Marcos Alonso. Solid-state lighting: A system review. *IEEE Industrial Electronics Magazine*, 7(4):6–14, 2013.
- [117] Andrei Nardelli, Eduardo Deuschle, Leticia Dalpaz de Azevedo, João Lorenzo Novaes Pessoa, and Enedir Ghisi. Assessment of light emitting diodes technology for general lighting: A critical review. *Renewable and Sustainable Energy Reviews*, 75:368–379, 2017.
- [118] Nobuhiro Ide, Takuya Komoda, and Junji Kido. Organic light-emitting diode (oled) and its application to lighting devices. In *Organic Light Emitting Materials and Devices X*, volume 6333, page 63330M. International Society for Optics and Photonics, 2006.
- [119] Vinod Kumar Khanna. *Fundamentals of solid-state lighting: LEDs, OLEDs, and their applications in illumination and displays*. CRC press, 2014.

-
- [120] Vitor C Bender, Tiago B Marchesan, and J Marcos Alonso. Solid-state lighting: A concise review of the state of the art on led and oled modeling. *IEEE Industrial Electronics Magazine*, 9(2):6–16, 2015.
- [121] Ching W Tang and Steven A VanSlyke. Organic electroluminescent diodes. *Applied physics letters*, 51(12):913–915, 1987.
- [122] Jeremy H Burroughes, Donal DC Bradley, AR Brown, RN Marks, K Mackay, Richard H Friend, PL Burns, and AB Holmes. Light-emitting diodes based on conjugated polymers. *nature*, 347(6293):539–541, 1990.
- [123] Junji Kido, Masato Kimura, and Katsutoshi Nagai. Multilayer white light-emitting organic electroluminescent device. *Science*, 267(5202):1332–1334, 1995.
- [124] Gianluca M Farinola and Roberta Ragni. Electroluminescent materials for white organic light emitting diodes. *Chemical Society Reviews*, 40(7):3467–3482, 2011.
- [125] Brian W D’Andrade and Stephen R Forrest. White organic light-emitting devices for solid-state lighting. *Advanced Materials*, 16(18):1585–1595, 2004.
- [126] Xu-Hui Zhu, Junbiao Peng, Yong Cao, and Jean Roncali. Solution-processable single-material molecular emitters for organic light-emitting devices. *Chemical Society Reviews*, 40(7):3509–3524, 2011.
- [127] Lili Bao and Michael D Heagy. A review of single white-light emitters: The quest for picture perfect dyes in the next generation of single layer woled displays. *Current Organic Chemistry*, 18(6):740–772, 2014.
- [128] Pance Naumov, Yutaka Ozawa, Kei Ohkubo, and Shunichi Fukuzumi. Structure and spectroscopy of oxyluciferin, the light emitter of the firefly bioluminescence. *Journal of the American Chemical Society*, 131(32):11590–11605, 2009.
- [129] Takahiro Kuchimaru, Satoshi Iwano, Masahiro Kiyama, Shun Mitsumata, Tetsuya Kadonosono, Haruki Niwa, Shojiro Maki, and Shinae Kizaka-Kondoh. A luciferin analogue generating near-infrared bioluminescence achieves highly sensitive deep-tissue imaging. *Nature communications*, 7(1):1–8, 2016.
- [130] Satoshi Iwano, Rika Obata, Chihiro Miura, Masahiro Kiyama, Kazutoshi Hama, Mitsuhiro Nakamura, Yoshiharu Amano, Satoshi Kojima, Takashi Hirano, Shojiro Maki, et al. Development of simple firefly luciferin analogs emitting blue, green, red, and near-infrared biological window light. *Tetrahedron*, 69(19):3847–3856, 2013.

- [131] David C McCutcheon, Miranda A Paley, Rachel C Steinhardt, and Jennifer A Prescher. Expedient synthesis of electronically modified luciferins for bioluminescence imaging. *Journal of the American Chemical Society*, 134(18):7604–7607, 2012.
- [132] Jagannath Kuchlyan, Debasis Banik, Arpita Roy, Niloy Kundu, and Nilmoni Sarkar. Excited-state proton transfer dynamics of firefly’s chromophore d-luciferin in dmso–water binary mixture. *The Journal of Physical Chemistry B*, 118(48):13946–13953, 2014.
- [133] Yoriko Ando, Kazuki Niwa, Nobuyuki Yamada, Toshiteru Enomoto, Tsutomu Irie, Hidehiro Kubota, Yoshihiro Ohmiya, and Hidefumi Akiyama. Firefly bioluminescence quantum yield and colour change by ph-sensitive green emission. *Nature Photonics*, 2(1):44–47, 2008.
- [134] Toru Nakatsu, Susumu Ichiyama, Jun Hiratake, Adrian Saldanha, Nobuyuki Kobashi, Kanzo Sakata, and Hiroaki Kato. Structural basis for the spectral difference in luciferase bioluminescence. *Nature*, 440(7082):372–376, 2006.
- [135] Mitra Kheirabadi, Zohreh Sharafian, Hossein Naderi-Manesh, Udo Heineman, Ulrich Gohlke, and Saman Hosseinkhani. Crystal structure of native and a mutant of lampyris turkestanicus luciferase implicate in bioluminescence color shift. *Biochimica et Biophysica Acta (BBA)-Proteins and Proteomics*, 1834(12):2729–2735, 2013.
- [136] Ron Simkovitch, Naama Karton-Lifshin, Shay Shomer, Doron Shabat, and Dan Huppert. Ultrafast excited-state proton transfer to the solvent occurs on a hundred-femtosecond time-scale. *The Journal of Physical Chemistry A*, 117(16):3405–3413, 2013.
- [137] Pance Naumov and Manoj Kochunnonny. Spectral- structural effects of the keto- enol- enolate and phenol- phenolate equilibria of oxyluciferin. *Journal of the American Chemical Society*, 132(33):11566–11579, 2010.
- [138] Yuval Erez and Dan Huppert. Excited-state intermolecular proton transfer of the firefly’s chromophore d-luciferin. *The Journal of Physical Chemistry A*, 114(31):8075–8082, 2010.
- [139] Emil H White, Mark G Steinmetz, Jeffrey D Miano, Peter D Wildes, and Robert Morland. Chemi-and bioluminescence of firefly luciferin. *Journal of the American Chemical Society*, 102(9):3199–3208, 1980.

- [140] Vadim R Viviani, Gabriele VM Gabriel, Vanessa R Bevilaqua, AF Simões, T Hirano, and PS Lopes-de Oliveira. The proton and metal binding sites responsible for the ph-dependent green-red bioluminescence color tuning in firefly luciferases. *Scientific reports*, 8(1):1–14, 2018.
- [141] Cristina Garcia-Iriepe and Isabelle Navizet. Effect of protein conformation and amp protonation state on fireflies’ bioluminescent emission. *Molecules*, 24(8):1565, 2019.
- [142] John Lee. Perspectives on bioluminescence mechanisms. *Photochemistry and photobiology*, 93(2):389–404, 2017.
- [143] Bruce R Branchini, Martha H Murtiashaw, Rachelle A Magyar, Nathan C Portier, Maria C Ruggiero, and Justin G Stroh. Yellow-green and red firefly bioluminescence from 5, 5-dimethyloxyluciferin. *Journal of the American Chemical Society*, 124(10):2112–2113, 2002.
- [144] E Santaniello and G Meroni. Color-tuning of firefly luciferase bioluminescence by modification of enzyme and substrate structure: new opportunities for optical imaging. *Minerva Biotechnologica*, 21(2):77, 2009.
- [145] Marlene DeLuca. Hydrophobic nature of the active site of firefly luciferase. *Biochemistry*, 8(1):160–166, 1969.

FATMAH MISH EBRAHIM

Email: ebrahim.fatmah@gmail.com

ORCID 0000-0002-0785-1575

EDUCATION

Ecole Polytechnique Federale de Lausanne (EPFL) PhD, Chemistry and Chemical Engineering	May 2017 – June 2020 (expected)
PHELMA, Politecnico di Torino, EPFL MSc. Micro-and Nano-technologies for Integrated Systems	Sept 2011 – Feb 2013
University College London BSc. Physics	Sept 2006 – June 2009

RESEARCH EXPERIENCE

Laboratory of Molecular Simulation, EPFL Doctoral assistant	May 2017 – May 2020
--	----------------------------

My research involves the design, synthesis, and investigation of novel porous, luminescent, crystalline materials for targeted applications. The luminescence of these materials stems from the incorporation of lanthanide ions and organic luminophores into their structures, and their structural and optical properties are characterised using a range of techniques including powder X-ray diffraction, gas adsorption isotherms, infrared, fluorescence, and UV-vis spectroscopy, and electron microscopy. Two novel materials were developed for sensing and OLED lighting, and prototype electronic devices were built to demonstrate the potential real-world applicability of these materials.

GALATEA Lab, EPFL Research assistant	Sept 2015 – Feb 2017
---	-----------------------------

Worked on femtosecond-laser micromachining of 3D structures within the bulk of fused silica. Applications of this process range from the realization of complex micromechanical devices to cleanroom-compatible microfluidics chips.

IBM Almaden, San Jose CA Visiting research fellow	March 2013 – August 2014
--	---------------------------------

Worked on design and characterisation of self-assembled, biodegradable and regenerable polymeric systems called coacervates, for drug delivery applications. Coacervate systems with easily tuneable size, loading capacity, stability, and structural integrity were formed and investigated using fluorescence spectroscopy, fluorescence anisotropy, atomic force microscopy, scanning electron microscopy, rheology, ellipsometry, and a set of optical tweezers.

Max Planck Institute for Biophysical Chemistry Research intern	May – August 2012
---	--------------------------

Worked on the design and fabrication of a droplet-based microfluidic chip with reflective channels and micro-lenses for the high signal-noise ratio, rapid screening of fluorescent assays in droplet micro-reactors.

London Centre for Nanotechnology Research intern	Sept 2008 – June 2009
---	------------------------------

BSc thesis on exploring the optical and structural properties of mono-, bi-, and few-layer graphene using optical microscopy, atomic force microscopy, and Raman spectroscopy

PROFESSIONAL EXPERIENCE

Bon Education STEM Education project consultant	Dec 2014 – Dec 2015
--	----------------------------

Involved in hiring and training of educators to implement education technology tools into government schools across the UAE. Also contributed to curriculum development, coordination, and implementation of hands-on, project-based educational workshops for young adults to incentivise the pursuit of higher education in STEM subjects.

Government of Ras Al Khaimah (RAK) Investment and Development Office Program manager	Sept 2009 – June 2011
---	------------------------------

Led budgeting, logistics and coordination of projects undertaken by the RAK Centre for Advanced Materials (RAK CAM), an entity focused on enhancing scientific research in the region, and the Al Qasimi Foundation, a public policy think-tank with a focus on society, education, and public health. Duties included outreach, conference production, and the management of projects for the development of education and public health in the state. Aided policy research for increased disability access, diabetes awareness, and improvement of girls education. Developed the RAK Teachers' Network and helped establish the Gulf chapter of the World Council of Comparative Education Societies.

LIST OF PUBLICATIONS

- **F. M. Ebrahim**, M. Fumanal, A. Gładysiak, S. Shyshkanov, D. Ongari, Ö. Kadioglu, K. M. Jablonka, S. Saris, C. P. Ireland, A. Mace, P. J. Dyson, K. C. Stylianou and B. Smit, “Tuneable luminescence from a biomolecule-inspired single-species emitter of white light”, *in submission*
- **F. M. Ebrahim**, T. N. Nguyen, S. Shyshkanov, A. Gładysiak, P. Favre, A. Zacharia, G. Itskos, P. J. Dyson and K. C. Stylianou, “Selective, Fast-Response, and Regenerable Metal–Organic Framework for Sampling Excess Fluoride Levels in Drinking Water” *J. Am. Chem. Soc.* 141, 7, 3052-3058 (2019)
- S. Kampouri, **F. M. Ebrahim**, M. Fumanal, P. A. Schouwink, C. P. Ireland, K. C. Stylianou and B. Smit, “Development of a MOF/MOF Heterojunction for Enhanced Photocatalytic Performance”, *in submission*
- M. A. Syzgantseva, C. P. Ireland, **F. M. Ebrahim**, B. Smit and O. A. Syzgantseva, “Metal Substitution as the Method of Modifying Electronic Structure of Metal–Organic Frameworks”, *J. Am. Chem. Soc.* 141, 15, 6271-6278 (2019)
- S. Shyshkanov, T. N. Nguyen, **F. M. Ebrahim**, K. C. Stylianou and P. J. Dyson, “In Situ Formation of Frustrated Lewis Pairs in a Water-Tolerant Metal–Organic Framework for the Transformation of CO₂”, *Angew. Chem. Int. Ed.* 58, 16 (2019)
- F. P. Kinik, T. N. Nguyen, E. Oveisi, B. Valizadeh, **F. M. Ebrahim**, A. Gładysiak, M. Mensi and K. C. Stylianou, “Discovery of a self-healing catalyst for the hydrolytic dehydrogenation of ammonia borane”, *J. Mater. Chem. A.* 41, 5371-5375 (2019)
- T. N. Nguyen, **F. M. Ebrahim**, K. C. Stylianou, “Photoluminescent, upconversion luminescent and nonlinear optical metal-organic frameworks: From fundamental photophysics to potential applications”, *Coord. Chem. Rev.* 377, 259-306 (2018)
- T. N. Nguyen, G. Capano, A. Gładysiak, **F. M. Ebrahim**, S. V. Eliseeva, A. Chidambaram, B. Valizadeh, S. Petoud, B. Smit and K. C. Stylianou “Lanthanide-based near-infrared emitting metal–organic frameworks with tunable excitation wavelengths and high quantum yields”, *Chem. Comm.* 54, 6816-6819 (2018)
- S. Kampouri, T. N. Nguyen, C. P. Ireland, B. Valizadeh, **F. M. Ebrahim**, G. Capano, D. Ongari, A. Mace, N. Guijarro, K. Sivula, A. Sienkiewicz, L. Forró, B. Smit and K. C. Stylianou, “Photocatalytic hydrogen generation from a visible-light responsive metal–organic framework system: the impact of nickel phosphide nanoparticles”, *J. Mater. Chem. A.* 6, 2476-2481 (2018)

CONFERENCE CONTRIBUTIONS

- **American Chemical Society (ACS) Spring 2019 National Meeting and Expo Orlando, FL**, oral presentation titled “A selective, fast-response, regenerable metal-organic framework for sampling excess fluoride levels in drinking water”
- **8th North America-Greece-Cyprus Workshop on Paramagnetic Materials (NAGC) 2018, Sparta**, oral presentation titled “Selective and sensitive metal-organic framework sensors with fast optical response for fluoride anions”
- **International Workshop on Advanced Materials 2018, Ras Al Khaimah**, oral presentation titled “Metal-organic framework sensors for sampling of trace contaminants in ground water”
- **SPIE Photonics West 2017, San Francisco, CA**, oral presentation titled “Fabrication of high aspect-ratio 3D metallic microstructures for electro-optic devices”